

Henri Tervo

NON-METALLIC INCLUSIONS IN STEELS AND THEIR EFFECT ON THE TOUGHNESS AND DUCTILITY

*ULTRA-HIGH-STRENGTH STEELS AND HIGH
STRENGTH OFFSHORE STEELS*

UNIVERSITY OF OULU GRADUATE SCHOOL;
UNIVERSITY OF OULU,
FACULTY OF TECHNOLOGY



ACTA UNIVERSITATIS OULUENSIS
C Technica 864

HENRI TERVO

**NON-METALLIC INCLUSIONS IN
STEELS AND THEIR EFFECT ON
THE TOUGHNESS AND DUCTILITY**

Ultra-high-strength steels and high strength offshore
steels

Academic dissertation to be presented with the assent of
the Doctoral Programme Committee of Technology and
Natural Sciences of the University of Oulu for public
defence in Martti Ahtisaari auditorium (L2), Linnanmaa, on
13 January 2023, at 12 noon

UNIVERSITY OF OULU, OULU 2023

Copyright © 2023
Acta Univ. Oul. C 864, 2023

Supervised by
Professor Jukka Kömi
Professor Mahesh Somani
Doctor Antti Kaijalainen

Reviewed by
Professor Claire Davis
Docent Andrey Karasev

Opponents
Professor Roman Kuziak
Professor Claire Davis

ISBN 978-952-62-3548-6 (Paperback)
ISBN 978-952-62-3549-3 (PDF)

ISSN 0355-3213 (Printed)
ISSN 1796-2226 (Online)

Cover Design
Raimo Ahonen

PUNAMUSTA
TAMPERE 2023

Tervo, Henri, Non-metallic inclusions in steels and their effect on the toughness and ductility. Ultra-high-strength steels and high strength offshore steels

University of Oulu Graduate School; University of Oulu, Faculty of Technology

Acta Univ. Oul. C 864, 2023

University of Oulu, P.O. Box 8000, FI-90014 University of Oulu, Finland

Abstract

Non-metallic inclusions and their effects on the toughness and ductility of ultra-high-strength steels (UHSS) and high strength offshore steels have been investigated in this study. In the case of UHSS, the scope covered the martensitic base material, while in the case of offshore steels, the coarse-grained heat-affected zone (CGHAZ), consisting primarily of various types of bainite, caused by the thermal cycles during the welding were mainly studied. The focus was on the degrading effect of inclusions on the toughness and ductility, but the beneficial effects of certain inclusion types through inducing the acicular ferrite (AF) formation in the CGHAZ of offshore steels were also considered.

In UHSS, it was found that small differences in impurity levels (IL), i.e. sum of S, N and O contents, had a significant impact on the inclusions. The number density of coarse inclusions increased with increasing IL from 0.7 mm^{-2} to 1.2 mm^{-2} . In the steel with a lower IL, the coarse inclusions were mainly calcium aluminates with a calcium sulphide cell around them, while in the steel with a higher IL, a majority of the coarse inclusions consisted of titanium nitrides (TiN) and elongated manganese sulphides (MnS). The MnSs were found to deteriorate the transverse ductility relative to the rolling direction, while it was suggested that TiNs impaired the impact toughness at $-40 \text{ }^\circ\text{C}$.

In the offshore steels, CGHAZs were simulated using various cooling rates in order to produce different microstructures and to be able to compare the combined effect of inclusions and microstructures on toughness properties.

Low heat-input welding and a lack of coarse TiNs were found to be important for excellent toughness in the CGHAZ of 500 MPa offshore steels. For high heat-input welding, it might be necessary to lower the carbon content of the steel in order to achieve good toughness in the CGHAZ.

Increasing prior austenite grain size, decreasing cooling rate, and the presence of small $\text{MnOTiO}_x(+\text{MnS})$ inclusions were found to promote the formation of AF in the CGHAZ of 420 MPa offshore steels. However, AF did not improve the impact toughness. This was concluded to be a result of coarse microstructural features and a large number of coarse inclusions that diminished the beneficial effect of AF. Additionally, the fraction of AF might not have been enough to improve the toughness of the CGHAZ.

Keywords: ductility, inclusions, steel, toughness, weldability

Tervo, Henri, Epämetalliset sulkeumat teräksissä ja niiden vaikutus sitkeysominaisuuksiin. Ultralujat teräkset sekä lujat offshore-teräkset

Oulun yliopiston tutkijakoulu; Oulun yliopisto, Teknillinen tiedekunta

Acta Univ. Oul. C 864, 2023

Oulun yliopisto, PL 8000, 90014 Oulun yliopisto

Tiivistelmä

Tässä väitöskirjassa on tutkittu epämetallisia sulkeumia ja niiden vaikutusta ultralujien terästen sekä lujien offshore-terästen sitkeysominaisuuksiin. Ultralujien terästen osalta tarkasteltavana oli perusaineen sitkeys, kun taas offshore-terästen osalta keskityttiin hitsauksesta johtuvan karkearaakeisen lämpömuutosvyöhykkeen (CGHAZ) sitkeyteen. Pääpaino oli sulkeumien haitallisessa vaikutuksessa sitkeyden kannalta, mutta lisäksi käsiteltiin myös asikulaarisen ferriitin (AF) muodostumista ja sen mahdollisesti sitkeyttä parantavaa vaikutusta offshore-terästen CGHAZ:ssa tietyn tyyppisten sulkeumien avulla.

Ultralujissa teräksissä pienen eron epäpuhtauspitoisuuksissa havaittiin vaikuttavan merkittävästi sulkeumarakenteeseen. Isojen sulkeumien määrä nousi epäpuhtauspitoisuuden noustessa. Pienemmällä epäpuhtauspitoisuudella isot sulkeumat olivat enimmäkseen pyöreitä kalsiumalumiinaatteja, kun taas suuremmalla epäpuhtauspitoisuudella isot sulkeumat olivat titaaninitridejä (TiN) sekä valssauksessa venyneitä mangaanisulfideja (MnS). MnS:n todettiin heikentävän teräksen sitkeyttä valssausuuntaan nähden poikittaisessa suunnassa, kun taas TiN:n havaittiin heikentävän iskusitkeyttä -40 °C :ssa.

Offshore-terästen CGHAZ:t simuloitiin käyttäen useita jäähtymisnopeuksia. Näin saatiin tuotettua erilaisia mikrorakenteita, jolloin voitiin vertailla mikrorakenteen ja sulkeumien yhteisvaikutusta sitkeysominaisuuksiin.

500 MPa offshore-teräksissä matalan lämmöntonin hitsausmenetelmillä voidaan saavuttaa erinomainen CGHAZ:n isku- ja murtumissitkeys, kun teräksessä ei ole isoja titaaninitridejä. Käytettäessä korkean lämmöntonin hitsausmenetelmiä riittävän hyvän sitkeyden saavuttamiseen vaadittaneen teräksen hiilipitoisuuden laskemista.

Riittävän karkean perinnäisen austeniitin raekoon sekä pienien MnO-TiO_x(+MnS) sulkeumien havaittiin edesauttavan AF:n muodostumista 420 MPa offshore-terästen CGHAZ:ssa. Lisäksi AF:n osuus mikrorakenteessa kasvoi jäähtymisnopeuden laskiessa. Toisin kuin oletettiin, AF ei parantanutkaan CGHAZ:n iskusitkeyttä. Tämän todettiin johtuvan mikrorakenteellisten tekijöiden karkeudesta sekä sitkeydelle haitallisten sulkeumien suuresta määrästä, jotka heikensivät sitkeyttä enemmän kuin AF paransi sitä. Lisäksi saavutettu AF:n osuus mikrorakenteessa ei välttämättä ollut tarpeeksi korkea, jotta sillä olisi CGHAZ:n sitkeyttä parantavaa vaikutusta.

Asiasanat: hitsattavuus, iskusitkeys, murtumissitkeys, sulkeumat, teräs

*”Nyt aika on teräksen, miekan ja hurmoksen
Metallitotuuden nimeen
Vaikka huomista mietimme tänään me elämme vain”
(Teräsbetoni, 2006)*

Acknowledgements

The research work for this dissertation started already in 2014 at the erstwhile Materials Engineering research group at the University of Oulu, as a part of the Finnish Metals and Engineering Competence Cluster (FIMECC Ltd.), later Digital, Internet, Materials & Engineering Co-Creation (DIMECC Ltd.) research program System Integrated Metals Processing (SIMP, 2014–2017) funded by Business Finland. In the following years, the research work has been linked to other Business Finland funded projects such as Flexible and adaptive operations in metal production (FLEX, 2017–2019) and Intelligent Steel Applications (ISA, 2019–2022). Additional funding has been received from the Riitta and Jorma Takanen foundation (2017), the Tauno Tönnig foundation (2019) and the Jenny and Antti Wihuri foundation (2019 and 2020). The University of Oulu Graduate School (UniOGS) also funded a conference journey related to this research work in 2018. The six months research visit to the University of Miskolc, Hungary in 2017 was funded by the European Union's Erasmus scholarship. Furthermore, the research work has been closely linked to the R&D projects of SSAB Europe Oyj, and the studied materials were provided by them. The author is grateful to all the funding agencies and foundations for generous funding that helped to accomplish the research work smoothly and made this dissertation possible.

During my research work I have had a pleasure to co-operate with numerous experts both from the academic and industrial fields. I am grateful to the supervisors of this dissertation: Prof. Jukka Kömi, Prof. Mahesh Somani, Dr. Antti Kaijalainen, and Prof. Emeritus David Porter who was supervising my work in the beginning before his retirement. Their comments, help and support have been invaluable for me throughout these years.

Thank you for the support and guidance also to my doctoral trainee follow-up group: Docent Eetu-Pekka Heikkinen, Dr. Olli Nousiainen, and Docent Jouko Leinonen who took part in the first follow-up group meeting before his retirement.

The expertise and the general atmosphere in the Materials and Mechanical Engineering research group has been a driving force for conducting my research work there. I want to express my gratitude to everybody in the group during these years. Particularly, acknowledging the co-authors of my original publications included in this work; Dr. Sakari Pallaspuuro, Dr. Vahid Javaheri, Dr. Satish Kolli and Dr. Mohammed Ali, my office roommates; Dr. Jaakko Hannula, Juho Mourujärvi, M.Sc. and Ilkka Miettunen, M.Sc., long time UHSS team members; Sami Koskenniska, M.Sc., Dr. Ari Saastamoinen, Niko Vähäkuopus, M.Sc., Pekka

Kantanen, M.Sc., Pekka Plosila, M.Sc., Renata Latypova, M.Sc. and Dr. Oskari Haiko. Practical work would not have been possible without the help and support of the laboratory staff; late Seppo Järvenpää, M.Sc., Sampo Uusikallio, M.Sc., Juha Uusitalo, M.Sc., Mr. Ilpo Alasaarela and Tun Tun Nyo, M.Sc.

I want to thank also Dr. Tuomas Alatarvas from the Process Metallurgy research group for all the inclusion discussions and for co-authoring my latest publications.

Microscopy was very important in this research work. Therefore, the staff of Centre for Material Analysis at the University of Oulu is acknowledged for all the help with their equipment.

Collaboration with the staff of SSAB Europe Oyj has also been a remarkable part of the research. Particularly, I want to acknowledge Dr. Severi Anttila, Dr. Saara Mehtonen and Dr. Pasi Suikkanen for the support, coordination, and general interest toward my work. Furthermore, I want to thank Teppo Pikkarainen, M.Sc. and Mikko Mehtonen, M.Sc. for co-authoring my publications.

During my doctoral studies I had a great opportunity to spend six months in the University of Miskolc, Hungary. I want to thank Prof. János Lukács and everybody in the Institute of Materials Science and Technology for welcoming me warmly. Additional acknowledgements to prof. Marcell Gáspár and Dr. Ádám Dobosy for the interesting discussions, help, advices, invitations and generally introducing me to the way of life in Hungary.

The pre-examiners of this dissertation, Prof. Claire Davis from the University of Warwick, UK, and Docent Andrey Karasev from KTH – Technical University of Stockholm, Sweden, are acknowledged for their valuable comments to improve the dissertation.

Finally, thank you to my family, relatives, and all acquaintances for all kinds of support throughout the years.

8.10.2022

Henri Tervo

List of abbreviations, definitions, and symbols

Abbreviations and definitions

bcc	body-centred cubic
bet	body-centred tetragonal
CGHAZ	coarse-grained heat-affected zone
CMOD	crack mouth opening displacement
CTOD	crack tip opening displacement
CVN	Charpy V-notch impact toughness
DBTT	ductile-brittle transition temperature
EBS	electron backscatter diffraction
ECD	equivalent circular diameter (μm)
e.g.	exempli gratia; for example
etc.	et cetera
FCAW	flux-cored arc welding
fcc	face-centred cubic
FESEM	field-emission scanning electron microscope
FGHAZ	fine-grained heat-affected zone
HV ₁₀	Vickers hardness using a 100N load
ICCGHAZ	intercritically reheated coarse-grained heat-affected zone
ICHAZ	intercritical heat-affected zone
i.e.	id est; that is
IL	impurity level
IQ	image quality
LSCM	laser scanning confocal microscope
LT	longitudinal direction
ND	normal direction
OES	optical emission spectroscopy
PAGS	prior austenite grain size (μm)
RA	reduction of area (%)
RD	rolling direction
SAW	submerged arc welding
SCHAZ	subcritical heat-affected zone
SENB	single-edge notched bend
TEM	transmission electron microscope

TMCP	thermomechanically controlled processing
TD	transverse direction
USE	upper shelf energy (J) or (J/cm ²)
UTS	ultimate tensile strength
XRD	X-ray diffraction
YS	yield strength
wt.%	weight fraction in percent

Symbols

A	percentage elongation after fracture (%)
$D_{80\%}$	grain size at 80% cumulative size distribution (μm)
$D_{90\%}$	grain size at 90% cumulative size distribution (μm)
E_a	absorbed energy in the crack arrest (J)
E_i	absorbed energy in the crack initiation (J)
E_p	absorbed energy in the crack propagation (J)
F_m	maximum load (kN)
M_s	martensite start temperature ($^{\circ}\text{C}$)
M_f	martensite finish temperature ($^{\circ}\text{C}$)
p	p-value (statistics)
P_{cm}	critical metal parameter for weld cracking
R_m	tensile strength (MPa)
R_p	0.2% offset yield strength (MPa)
$t_{8/5}$	cooling time from 800 $^{\circ}\text{C}$ to 500 $^{\circ}\text{C}$ (s)
T	temperature ($^{\circ}\text{C}$)
T_{35}	impact toughness transition temperature at 35 J/cm ² ($^{\circ}\text{C}$)
T_p	peak temperature of HAZ simulation ($^{\circ}\text{C}$)

List of original publications

This thesis is based on the following publications, which are referred to throughout the text by their Roman numerals I–IV:

- I Tervo, H., Kajjalainen, A., Pikkarainen, T., Mehtonen, S., & Porter, D. (2017). Effect of impurity level and inclusions on the ductility and toughness of an ultra-high-strength steel. *Materials Science & Engineering A*, 697, 184–193. <https://doi.org/10.1016/j.msea.2017.05.013>
- II Tervo, H., Kajjalainen, A., Pallaspuro, S., Anttila, S., Mehtonen, S., Porter, D., & Kömi, J. (2020). Low-temperature toughness properties of 500 MPa offshore steels and their simulated coarse-grained heat-affected zones. *Materials Science & Engineering A*, 773, 138719. <https://doi.org/10.1016/j.msea.2019.138719>
- III Tervo, H., Kajjalainen, A., Javaheri, V., Kolli, S., Alatarvas, T., Anttila, S., & Kömi, J. (2020). Characterization of coarse-grained heat-affected zones in Al and Ti-deoxidized offshore steels. *Metals*, 10(8), 1096. <https://doi.org/10.3390/met10081096>
- IV Tervo, H., Kajjalainen, A., Javaheri, V., Ali, M., Alatarvas, T., Mehtonen, M., Anttila, S., & Kömi, J. (2021). Comparison of impact toughness in simulated coarse-grained heat-affected zone of Al-deoxidized and Ti-deoxidized offshore steels. *Metals*, 11(11), 1783. <https://doi.org/10.3390/met11111783>

In all publications, Henri Tervo was the main corresponding author. Most of the writing, conceptualization, microscopy, and hardness testing as well as analysis of the results were done by the main author.

Supervisors of the research work were Prof. Emeritus David Porter (Publications I and II), Dr. Antti Kajjalainen (Publications I–IV) and Prof. Jukka Kömi (Publications II–IV). As a native English speaker, Prof. Emeritus Porter also checked the language in Publications I and II. All supervisors are acknowledged for their valuable comments, help and support throughout the research work.

Tensile tests and Charpy V-notch impact toughness tests for Publication I were performed at SSAB Raahe under the supervision of Teppo Pikkarainen M.Sc. The Charpy V-notch impact toughness tests and CTOD fracture toughness tests for Publication II were performed at SSAB Raahe under the supervision of Dr. Saara Mehtonen. The tensile tests for Publication II were carried out by the main author with the aid of Tun Tun Nyo M.Sc. Jussi Paavola M.Sc. assisted the main author with the laboratory-scale hot-rolling for Publication II. Gleeble simulation tests for the study of heat-affected zones for publications II–IV were conducted by Juha Uusitalo M.Sc, who also took the macroscale photographs of the fracture surfaces in Publications I and IV. Tensile testing specimens for Publication II, as well as

Charpy V-notch impact toughness testing specimens for Publications II and IV, were machined by Mr. Ilpo Alasaarela.

The fracture toughness results in Publication II were analysed and visualized by Dr. Sakari Pallaspuro. Fractography studies were performed by the main author with the assistance of Dr. Sakari Pallaspuro (Publication II) and Mikko Mehtonen M.Sc (Publication IV). Statistical analyses in Publications II–IV were performed by Dr. Severi Anttila. Prior austenite grain size reconstruction using MTEX software and Image Quality analysis to quantify phase fractions for Publications III and IV were performed by Dr. Vahid Javaheri. TEM studies for Publication III were operated by Sami Saukko M.Sc. for the samples prepared by Esa Heinonen, M.Sc. using the Focused Ion Beam. The DICTRA modelling for Publication III was performed by Dr. Satish Kolli. XRD and TEM studies for Publication IV were performed by Dr. Mohammed Ali.

Inclusions were measured at SSAB Raahe under the supervision of Teppo Pikkarainen M.Sc (Publication I), Dr. Saara Mehtonen (Publication II) and Dr. Severi Anttila (Publications III and IV). Inclusions were classified and visualized in Publications III and IV by Dr. Tuomas Alatarvas using a method developed by him. Instrumented Charpy V-notch impact toughness tests for Publication IV were performed at the Kemi-Tornio University of Applied Sciences and the results were analysed and visualized by Mikko Mehtonen M.Sc. Sample preparation for the microstructural characterization and hardness measurements in all publications was performed by Tun Tun Nyo M.Sc. Reviewing and correcting of papers before submission were carried out by Prof. Emeritus David Porter (Publications I and II), Dr. Antti Kaijalainen (Publications I–IV), Dr. Saara Mehtonen (Publications I and II), Dr. Severi Anttila (Publications II–IV), Dr. Vahid Javaheri (Publications III and IV), Dr. Sakari Pallaspuro (Publication II), Dr. Mohammed Ali (Publication IV) and Dr. Tuomas Alatarvas (Publications III and IV).

Finally, the compositions of the studied steels were designed at SSAB Raahe, and delivered by SSAB Raahe (Publications I and II) and Outokumpu Oyj (Publications III and IV).

Content

Abstract	
Tiivistelmä	
Acknowledgements	9
List of abbreviations, definitions, and symbols	11
List of original publications	13
Content	15
1 Introduction	17
1.1 Background	17
1.2 Aims and objectives of the study	19
2 Theoretical background	21
2.1 Inclusions in steels	21
2.1.1 Oxides.....	22
2.1.2 Sulphides	24
2.1.3 Nitrides	25
2.2 Microstructures	25
2.2.1 Ferrite	26
2.2.2 Bainite	26
2.2.3 Martensite.....	28
2.3 Inclusions and mechanical properties	29
2.3.1 Negative effect of inclusions on toughness and ductility	29
2.3.2 Positive effect of inclusions on toughness through inducing acicular ferrite formation.....	32
3 Materials and methods	35
3.1 Materials	35
3.1.1 Ultra-high-strength steels	35
3.1.2 High-strength offshore steels.....	35
3.2 Microstructural characterization	38
3.2.1 General microstructural characterization.....	38
3.2.2 Inclusion measurements	39
3.3 Mechanical testing	39
3.3.1 Tensile testing.....	40
3.3.2 Charpy V-notch impact toughness testing	40
3.3.3 Hardness testing	41
3.3.4 Fracture toughness testing	41

4 Results	43
4.1 Effect of impurity level and inclusions on the ductility and toughness of an ultra-high-strength steel.....	43
4.1.1 Microstructures and mechanical properties	43
4.1.2 Inclusions.....	46
4.2 Low-temperature toughness properties of 500 MPa offshore steels and their simulated coarse-grained heat-affected zones	48
4.2.1 Microstructures and mechanical properties	48
4.2.2 Inclusions.....	57
4.3 Characterization of coarse-grained heat-affected zones in Al- and Ti-deoxidized offshore steels	60
4.3.1 Microstructures and mechanical properties	61
4.3.2 Inclusions.....	78
5 Discussion	83
5.1 Effect of impurity level and inclusions on ductility of ultra-high-strength steels	83
5.1.1 Effect of microstructure on toughness and ductility	83
5.1.2 Effect of inclusions and impurity content on toughness and ductility	84
5.2 Effect of inclusions on toughness and ductility of the CGHAZ of 500 MPa offshore steels	87
5.3 Factors affecting the impact toughness of the CGHAZ of 420 MPa offshore steels	91
5.3.1 Role of titanium oxides in inducing acicular ferrite formation	92
5.3.2 Other factors affecting acicular ferrite formation	94
5.3.3 Role of coarse inclusions impairing the impact toughness of the coarse-grained heat-affected zone	95
5.3.4 Other factors affecting the impact toughness of the coarse-grained heat-affected zone	97
6 Future considerations	103
7 Summary and conclusions	105
8 Novel features	109
References	111
Original publications	117

1 Introduction

It has been known for a long time that the steel consists not only of metal, but also non-metallic particles such as nanoscale precipitates and microscale inclusions such as carbides, oxides, sulphides and nitrides. For instance, McCance's paper about non-metallic inclusions in steel was published as early as 1918 [1].

Inclusions became a hot topic in steel research in the 1960s when it was found that lamellar tearing problems in the welded structures were caused by inclusions, leading to a better understanding of the influence of inclusions on the properties of steel [2]. To share the ideas and research results regarding inclusions in steels among the international research community, the first International Conference on Clean Steel was arranged in 1970 in Hungary. Since then, the Hungarian Mining Society arranged nine more Clean Steel conferences by 2018, indicating the ongoing importance of research on the inclusions and cleanliness of steel [3].

Traditionally, cleanliness of steel has been extremely important in applications such as aerospace [4] and automotive high strength steels [5]. For instance, in bearing steel grades, oxygen contents as low as 5–10 ppm were achieved already in the 1990s in order to avoid fatigue strength problems caused by oxide inclusions [5].

Despite a lot of work regarding the effect of inclusions on steels being conducted already over decades, it is important to continue the work with modern steels. This is all the more essential due to the ever-increasing strength level of steels that makes them more prone to the detrimental effect of inclusions, since the maximum inclusion size that can be tolerated without reductions in ductility and toughness is known to decrease with increasing strength [6]. The strict quality requirements for steel products in modern society further encourage continued research to guarantee the demanded properties. Additionally, the inclusion content in modern ultra-high-strength and advanced high-strength steels differs significantly from that in conventional steels due to the improved cleanliness control in the steel production. Hence, it is important to update the knowledge of inclusions to the 2020s.

1.1 Background

Ultra-high-strength steels (UHSS) produced cost-efficiently by hot rolling and subsequent direct quenching are suitable for applications where cost-savings can be achieved with weight reductions. Due to their martensitic microstructure, these

steels have excellent mechanical properties when it comes to strength and hardness. However, due to the same high strength, these steels are more prone to toughness and ductility problems further debilitated by non-metallic inclusions. Therefore, the impurity levels in UHSSs must be significantly lower than present in lower strength conventional steels.

The published research about inclusions in UHSSs and their effect on the mechanical properties is still scarce. Moreover, the low impurity levels of these modern steels produce different kinds of inclusion contents (including the number density, distribution, type, shape and size of inclusions) than in conventional steels. Therefore, it is important to study how this reduced impurity level affects the properties of UHSS and if they can be further improved by modifying the inclusion content.

Besides UHSS, the materials studied for this doctoral research also included high strength offshore steels. The thermomechanically controlled hot rolling process (TMCP), typically utilized in the manufacturing of these steels, provides a fine-grained microstructure that leads to a good combination of strength and toughness in the base plate of these steels. Additionally, good weldability is provided by low contents of carbon and other alloying elements.

Typical applications for high strength offshore steels are oil drilling platforms, where the safety of the structures is extremely important, and structures need to withstand harsh service conditions. For instance, 500 MPa offshore steels have been used in the Valhall oil drilling platform in Norway [7]. However, these steels are also suitable for other structural applications, where a combination of excellent strength, toughness and weldability is needed.

The challenge regarding these steels is the toughness in the weakest spots of the structures, which are often located in the heat-affected zones (HAZ), where the original fine-grained microstructure is altered due to the thermal cycles caused by the welding process. Particularly vulnerable are the coarse-grained heat-affected zone (CGHAZ), the intercritical heat-affected zone (ICHAZ) and the intercritically reheated coarse-grained heat-affected zone (ICCGHAZ). However, standards such as EN 10225-1 [8] and NORSOK M-120 [9] also strictly require good toughness in these zones.

Inclusions have a significant role when it comes to toughness problems in the HAZ of these steels, since they may initiate cleavage fractures, which, due to the coarsened grain size in HAZs, propagate freely over relatively long distances and eventually lead to failure of the structure. On the other hand, certain kinds of

inclusions can also be utilized to promote the formation of acicular ferrite in the HAZ, which is expected to improve the toughness.

Therefore, these steels fit excellently into the scope of this doctoral research and make a good entity for the effect of inclusions in some modern steels, which are relevant to the research and development topics at the time of writing.

1.2 Aims and objectives of the study

Two different main objectives were derived due to the different types of steels studied.

Regarding the UHSS, the aim is to find out how different types of inclusions affect the base material ductility and toughness of these steels. Additionally, the published research about the inclusion content of modern ultra-high-strength steels is very sparsely available. Hence, one of the aims is to investigate the typical inclusion content of these steels.

In the case of high-strength offshore steels, the aim is similar but instead of the base material, the focus is on the coarse-grained heat affected zone (CGHAZ) that forms as a result of heat cycles caused by welding. These steels are required to have good weldability even in the weakest parts of the structures, which often happen to be the CGHAZ, and need to have sufficient toughness in order to pass the strict requirements of the standards [9]. Hence, the aim is to investigate if the inclusions affect the impact and fracture toughness of the CGHAZ in these steels. Additionally, the aim is to study the possibility to improve the toughness of the CGHAZ through the acicular ferrite formation induced by certain inclusion types.

2 Theoretical background

2.1 Inclusions in steels

Inclusions are non-metallic particles, which are always present in steels. They form as chemical compounds of impurities, such as oxygen, sulphur, and nitrogen, with a metallic component that is present in steel either as an alloying element or as an impurity, such as aluminium, silicon, manganese, titanium, magnesium and calcium. Generally, oxides are the first inclusions to form during the steelmaking process. Sulphides may form in liquid temperatures, but also near the solidifying temperature of the steel. Nitrides generally form during solidification. In practice, inclusions often nucleate on the surface of existing inclusions, forming complex mixes of various inclusion types. Each of the inclusion types has its own characteristics when it comes to the shape, hardness, bonding to the steel matrix, deformability and behaviour during hot rolling, and finally, the effect on manufacturing process of steel and different properties of the finished steel product. Example of different types of inclusions and their behaviour during hot working is presented in Fig. 1.

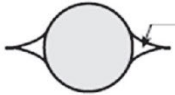
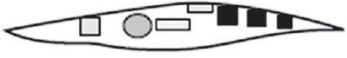
Before hot working	After hot working	
		"hard" inclusion
		
		
		Complex inclusion
		Plastic inclusion

Fig. 1. Examples of different types of inclusions and their behaviour during hot working (Reprinted under CC BY-NC-ND 4.0 license¹ from [10] © 2019 Brazilian Metallurgical, Materials and Mining Association. Published by Elsevier Editora Ltda.).

2.1.1 Oxides

In commercial Al-killed steels, the most common oxides include alumina (Al_2O_3) and different types of spinels (e.g., $\text{Al}_2\text{O}_3\text{-MgO}$). However, these inclusions are often modified by Ca-treatment into calcium aluminates ($x\text{CaO-yAl}_2\text{O}_3$) [11], [12]. Titanium oxides and titanium-manganese oxides (e.g., TiO , Ti_2O_3 , $(\text{Ti,Mn})_2\text{O}_3$) are present in Ti-deoxidized steels [13]–[15].

¹ <https://creativecommons.org/licenses/by-nc-nd/4.0/>

Alumina (Al_2O_3)

Al_2O_3 forms as a deoxidation product in the early part of the steelmaking process. Aluminium is added to molten steel to remove oxygen from the steel [12]. Al reacts with dissolved O forming Al_2O_3 , which is lighter than liquid steel and rises to the top of the ladle and eventually attaches to the slag that is added to the surface of the molten steel [12].

However, some of the Al_2O_3 will remain in the steel. Al_2O_3 appears in liquid steel as solid particles due to their high melting point [16]. Al_2O_3 tends to agglomerate on the surface of the submerged entry nozzle during the continuous casting, causing clogging and eventually distractions to the process [12]. In the solidified steel, Al_2O_3 has an irregular shape and a tendency to form clusters [12]. During hot rolling, Al_2O_3 breaks into stringers, which cause anisotropy of toughness and ductility in the finished steel product [12]. Subsequently, both castability and properties of the finished steel product can be improved when Al_2O_3 is modified by Ca-treatment to form less harmful calcium aluminates [12], [16].

Calcium aluminate ($xCaO-yAl_2O_3$)

Ca-treatment modifies Al_2O_3 into $xCaO-yAl_2O_3$, where x and y depend on how well the Ca-treatment succeeds and define the properties of the inclusion [17]. With a suitable combination of x and y , the inclusion takes a spherical shape and remains as liquid at liquid steel temperatures [17]. This prevents the inclusions causing clogging during the continuous casting process [17]. These types of inclusions also withstand the load during hot rolling relatively well, rendering them less prone to breaking into stringers, which would cause anisotropy of toughness and ductility in the steel [17].

Titanium oxides and titanium-manganese oxides (e.g. TiO , Ti_2O_3 , $(Ti,Mn)_2O_3$)

Titanium oxides are present in steels deoxidized with Ti instead of Al [15]. Ti-deoxidation is deliberately carried out in order to produce these inclusions due to their ability to promote acicular ferrite formation e.g., in heat-affected zones of steels [15]. However, due to the high cost of Ti-deoxidation, it is more common to use cheaper elements such as Al, Mn or Si for deoxidation and modify the oxides

with the addition of Ti during secondary refining [14]. MnTiO₂ inclusions have been reported when deoxidizing the steel with low Ti-content [15].

2.1.2 Sulphides

In conventional steels, the most common sulphides are manganese sulphides (MnS). Mn is basically always added to steel as an alloying element because sulphur would otherwise form sulphides with Fe, causing difficulties during hot forming due to hot shortness [12], [18]. In Ca-treated steels, MnS are modified to form CaS or (Mn,Ca)S [16].

Manganese sulphide (MnS)

During the solidification of steel, the formation of MnS takes place in the interdendritic regions, which are sulphur-rich and remain in liquid state for the longest duration of time [16]. MnS tends to elongate during hot rolling, because it is softer than the surrounding steel matrix in the hot rolling temperatures. These elongated inclusions impair the transverse ductility regarding the rolling direction, causing in-plane anisotropy [11]. MnS also increases the susceptibility of the steel to hydrogen-induced cracking by providing sites for hydrogen accumulation due to its low bonding strength to the steel matrix [16].

Calcium sulphide (CaS)

In Ca-treated steels, MnS is modified to form CaS or (Mn,Ca)S, depending on the efficiency of Ca-treatment. CaS forms earlier in liquid steel than MnS and is therefore evenly distributed. They are also significantly harder than MnS, making them less prone to elongating during hot rolling [11], [16]. Often, CaS precipitates on the surface of pre-existing $x\text{CaO}\cdot y\text{Al}_2\text{O}_3$, forming a shell around these spherical inclusions [16].

2.1.3 Nitrides

Titanium nitride (TiN)

Titanium is generally alloyed in steel either to form nanoscale TiN precipitates, which are known to inhibit the austenite grain growth, e.g., during welding [19], [20], or to bind N, thus preventing the formation of boron nitrides in B-alloyed steels [21]. However, when the product of %Ti \times %N (in wt.%) exceeds the solubility product of TiN at the solidus temperature, there is a risk that TiN may form as microscale inclusions before the solidification of the steel [21]. Due to the microsegregation phenomenon, the local %Ti \times %N product in the interdendritic regions increases and coarse TiN inclusions may form even if the %Ti \times %N product of the bulk composition is below the solubility product of TiN [22].

TiN inclusions often have a rectangular shape with sharp edges and corners, and they are known to initiate cleavage fracture due to their brittleness and strong bonding to the steel matrix [23]. This means that the inclusion fractures easily due to the stresses from the matrix and the fracture propagates further into the steel matrix through the inclusion-matrix interface [24].

2.2 Microstructures

At hot rolling temperatures, steel is in austenite phase form that has a face-centred cubic crystal structure (fcc). During cooling, austenite transforms to microstructures with either a body-centred cubic (bcc) or a body-centred tetragonal (bct) structure such as ferrite, pearlite, bainite or martensite depending on the cooling rate, in this order comprising the slowest to the fastest cooling. Generally, the hardness of the steel increases and the toughness decreases in the same order. Each of these phases or allotropes also have sub-types.

During welding, the originally achieved microstructures change due to the high temperatures and varying cooling rates, depending on the welding method and parameters. The significant temperature range concerning the transformed microstructure is between 800 °C and 500 °C during the cooling and the time spent in this range is usually denoted as cooling time, $t_{8/5}$. In this temperature range, $t_{8/5}$ will influence the transformation characteristics of austenite into other phases depending on the cooling rate similarly as in the case of base metal during cooling after hot rolling.

The microstructures relevant for the steels studied in this dissertation are briefly presented in the following sub-chapters.

2.2.1 Ferrite

Ferrite can be divided into allotriomorphic and idiomorphic sub-types depending on the location of their nucleation, either at the austenite grain boundaries or inside the austenite grains on non-metallic inclusions [25]. The growth of ferrite is controlled by diffusion and/or migration of interfaces and the transformation can occur only at high temperatures [25].

Allotriomorphic ferrite

Allotriomorphic ferrite, e.g., polygonal ferrite, transforms from austenite at the slowest cooling rates. It nucleates at the austenite grain boundaries and assumes the shape of the original austenite grain [25]. In steels with very low carbon content, the formation of quasi-polygonal ferrite with a highly irregular shape is also possible [26].

Acicular ferrite

Acicular ferrite (AF) is a type of intragranular ferrite, i.e., it nucleates within the grain e.g., on non-metallic inclusions instead of grain boundaries. Its transformation takes place in a range between bainite and polygonal ferrite in the continuous cooling transformation (CCT) diagram [27], and in the temperature range of 650–440 °C depending on the cooling rate and chemical composition of the steel [15].

AF is known to improve the toughness of weld metal and heat-affected zones by increasing the number of high angle boundaries [28]. More precisely, its chaotically oriented acicular, i.e., needle-like grains of around 1–3 µm in width and 5–15 µm in length, form a fine-grained and interlocking complex structure that prevents the propagation of cleavage cracks efficiently [14].

2.2.2 Bainite

Bainite transforms from austenite when the cooling rate is faster than that for ferrite and pearlite formation but slower than that for martensite formation. Historically,

bainitic microstructures have been classified into various subgroups according to their morphologies. However, since the early days of bainite research, the main groups have been upper bainite and lower bainite, based on their transformation temperatures [26]. Upper bainite and lower bainite consist of ferrite and carbide components, where the ferrite plates are approximately 10 μm long and 0.2 μm thick [25]. A schematic presentation of the difference between upper and lower bainite is shown in Fig. 2.

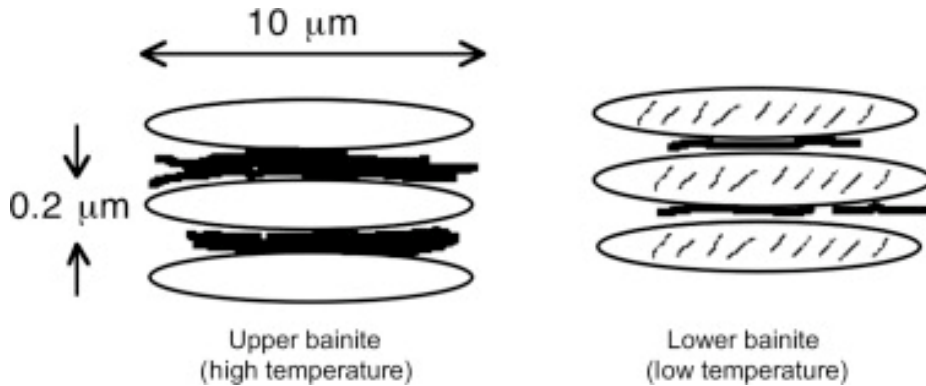


Fig. 2. Schematic presentation of upper and lower bainite (Reprinted, with permission, from [25] © 2014 Elsevier B.V.).

Upper bainite

Upper bainite typically forms in the temperature range between 450 $^{\circ}\text{C}$ and 500 $^{\circ}\text{C}$, and consists of parallel ferrite laths or plates and discontinuous cementite particles between the ferrite [26]. The amount of cementite between the ferrite depends on the carbon content of the steel and the ferrite itself is free from carbides [25]. The coarse cementite particles are detrimental to the toughness of the steel [25]. Degenerated upper bainite is a subgroup of upper bainite that has residual martensite-austenite (MA) microconstituents instead of cementite between the ferrite laths [26].

Lower bainite

Lower bainite forms close to the martensite start temperature (M_s), and in addition to cementite in carbon-rich interlath regions, fine cementite precipitates are located

inside ferrite laths as intralath particles at angles between 55° and 60° [26]. Lower bainite also has a subgroup of degenerated lower bainite where MA constituents, instead of cementite, are located inside ferrite laths [26].

Granular bainite

Granular bainite is composed of an irregular type of ferrite with secondary phases between the ferrite grains [26]. Typical for granular bainitic microstructure is the lack of carbides [26]. Instead, according to the same source, the secondary phase microconstituents in this kind of microstructure may contain e.g., degenerated pearlite, debris of cementite, bainite, martensite-austenite (MA) or martensite.

Granular bainite has been reported to have better toughness compared to upper bainite in ultralow-carbon steels [29]. However, as reported in the same source, the toughness of granular bainite decreases due to the formation of coarse MA constituents in steels with higher carbon content.

2.2.3 Martensite

Martensite forms at the highest cooling rates and may occur even in steels with very low carbon content [26]. Martensitic transformation is diffusionless and can also be called a shear or displacive transformation [30]. Being athermal transformation, the amount of martensite product phase depends only on the temperature. Martensite start temperature (M_s) is the temperature where martensite begins to form during cooling, and the formation of martensite continues until the temperature reaches a martensite finish temperature (M_f) [31]. Both M_s and M_f depend on the alloying content [31]. In low-carbon steels, martensite usually forms as laths, with a typical lath being about $0.3 \times 4 \times 200 \mu\text{m}$, but the actual size depends on the austenite grain size [30]. These laths are organized into blocks, and the clusters of blocks form packets inside the austenite grain [30]. The size of the packet controls the cleavage crack propagation and therefore has an influence on the toughness of the steel [30]. Auto-tempering of martensite may occur due to high M_s , leading to the presence of randomly distributed cementite precipitates inside martensite laths [26].

2.3 Inclusions and mechanical properties

Inclusions have been reported to affect various properties in steels [11], [32]–[34]. In the current research, the focus is on the toughness and ductility. Hence, the following sub-chapters will present the theoretical background of inclusions, which affect these properties.

2.3.1 Negative effect of inclusions on toughness and ductility

Ductile fracture

Inclusions have a drastic role in ductile fracture by initiating nucleation of microvoids around themselves [12], [35], [36]. As explained in the same sources, with increasing tension, these microvoids grow and coalesce, eventually leading to final fracture. The number of inclusions correlates directly with the number of microvoids. There are two mechanisms that dictate how these microvoids nucleate around inclusions: either the inclusion debonds from the matrix during the plastic deformation due to the stress field around the inclusion, or the stress concentration caused by the plastic deformation breaks the inclusion. The occurring mechanism depends at least on the shape of the inclusion, e.g., plate-like inclusions break easier than spherical ones. Manganese sulphide is favourable for microvoid nucleation since it shrinks more than the steel matrix during solidification. Generally, both oxides and sulphides only bond weakly to the matrix and they tend to debond easily at the beginning of the plastic deformation. The shape of the microvoid depends on the shape of the inclusion. Spherical inclusions incur less stress concentration than sharp-edged ones. This may affect the growth rate of the microvoids since it is dependent not only on the shape of the microvoid but also on the state of stress and elongation in the matrix. When the volume fraction of microvoids and the elongation of the matrix exceed a critical value, the final fracture occurs, leaving characteristic dimples at the fracture surface [12], [35], [36].

When the strength of the steel increases, the elongation needed to cause the fracture decreases, as the nucleation of microvoids initiate earlier in the elongation process [37]. It has been observed that microvoids nucleate first around manganese sulphides, then on smaller oxides, and lastly even at smaller carbides [38]. An example of a ductile fracture surface is shown in Fig. 3.

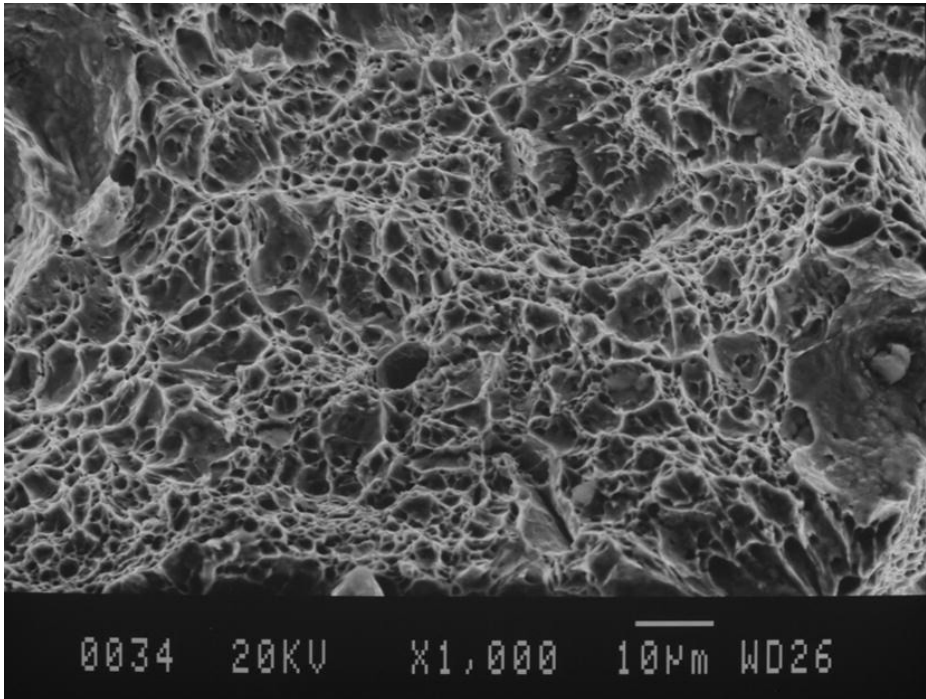


Fig. 3. Ductile fracture surface with dimples in HSLA-100 steel at $-196\text{ }^{\circ}\text{C}$ after a strain rate of 1600 s^{-1} (Reprinted, with permission, from [39] © 2016 Elsevier Ltd.).

In conventional steels, the effect of inclusions on ductility has been studied for decades and e.g., the detrimental effect of elongated inclusions, such as manganese sulphides, on the ductility in transverse direction compared to the rolling direction is well known [12].

Xiao *et. al* [40] studied the effect of MnS on ductility of case hardening steel DIN 18CrNiMo7-6 with relatively high sulphur contents (from 0.007 % to 0.037%) with and without Ca-treatment. The strength levels of the steels were comparable with those of ultra-high-strength steels ($R_m \approx 1400\text{ MPa}$, $R_{p0.2} \approx 1100\text{ MPa}$). It was noted that the transverse ductility decreased in all cases compared to the longitudinal ductility.

Ghosh *et. al* [41] also studied the effect of sulphur content on anisotropy of ductility, but in steels with more moderate strength (yield strength $\approx 300\text{--}600\text{ MPa}$). The studied sulphur contents were 0.01% and 0.03%, and the results showed that in case of higher sulphur content the transverse upper shelf energy in Charpy V-notch impact toughness testing was only 14.6 J, compared to 46.3 J in longitudinal

direction. However, in case of lower sulphur content such anisotropy was not observed.

Wilson studied in the early 1980s the effect of inclusions and Ca-treatment on various mechanical properties in a wide range of steel grades [42], [43]. For instance, the presence of elongated manganese sulphides in the centreline led to the decrease in reduction of area from 72.2% to 36.1% measured in longitudinal and transverse directions, respectively. However, such anisotropy was not observed when Ca-treatment was applied. The studied materials were conventionally produced (YS \approx 360–370 MPa, UTS \approx 530–540 MPa S-content 0.019%) and Ca-treated (YS \approx 330–360 MPa, UTS \approx 500–520 MPa, S-content 0.007%) A387-22 steel plates [43].

Brittle fracture

Of the two fracture modes, ductile and brittle, the latter is generally more severe and should be prevented as much as possible [36]. As explained in the same source, this is due to its unpredictable nature, since it propagates at high speed, often without plastic deformation, and possibly with little absorbed energy. The microscopic mechanism behind the macroscopic brittle fracture can be a transgranular cleavage fracture, intergranular fracture or geometrically constrained ductile fracture. The factors affecting the type of fracture, i.e., ductile or brittle, comprise crystal structure, microstructure, loading rate and temperature. An increase in grain size increases the ductile-brittle transition temperature (DBTT) in steels with a body-centred cubic (bcc) lattice. An increase in strain rate also raises the DBTT except in high-strength steels [36].

A cleavage fracture has characteristic microscale faceted flat regions which are connected by so-called river lines [36]. According to the same source, these river lines show the propagation of the fracture, often beginning from the crack initiation site and leading to obstacles such as grain boundaries or packet boundaries in the case of bainitic and martensitic steels. However, these river lines only show the local crack propagation, not necessarily the macroscopic route of the fracture. In practice, microscopic fracture surfaces may show characteristics of both cleavage and ductile fractures forming, so-called quasi-cleavage fracture [36].

Regarding the effect of inclusions on cleavage fractures, there are contradicting studies. In recent decades, a cleavage fracture has generally been considered the result of other factors in the microstructure, such as grain size [12], and suggested to begin e.g., from dislocation interactions, twinning deformation, or second-phase

particles such as grain boundary carbides [44]. On the other hand, many studies suggest hard inclusions, such as TiN and Al₂O₃, play a role in the initiation of the cleavage fracture [21], [23], [45].

In coarse-grained heat-affected zone, the combined effect of coarsened grain size and hard and brittle inclusions such as TiN is known to increase the risk of cleavage fracture [23]. Additionally, it has been shown that the spatial distribution of coarse TiN inclusions affects the toughness properties via statistical sampling [46]. An example of a cleavage fracture surface is shown in Fig. 4.

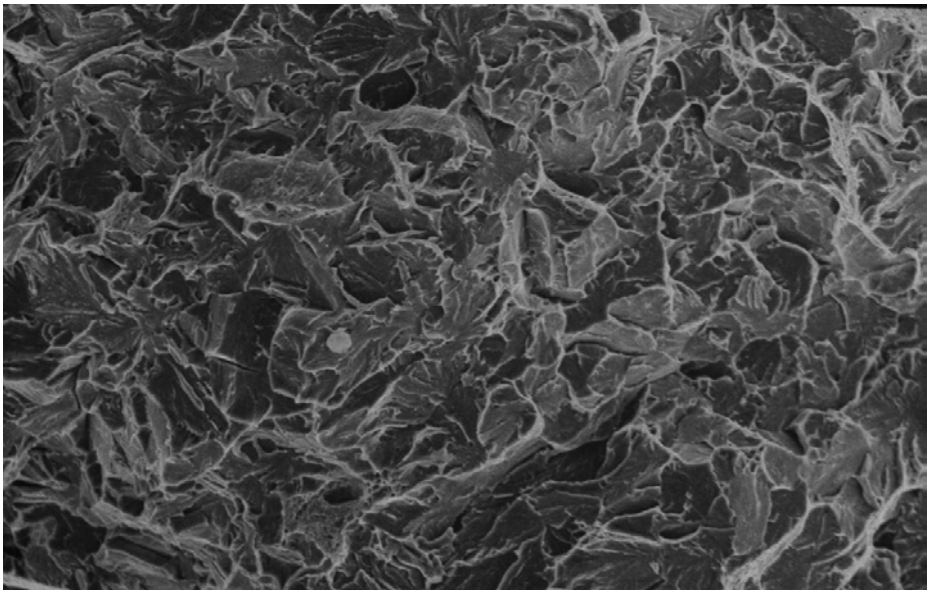


Fig. 4. Cleavage fracture surface in HSLA-100 steel at $-196\text{ }^{\circ}\text{C}$ after a strain rate of 10800 s^{-1} (Reprinted, with permission, from [39] © 2016 Elsevier Ltd.).

2.3.2 Positive effect of inclusions on toughness through inducing acicular ferrite formation

Besides the detrimental effect of inclusions on the toughness and ductility of steels, certain types of inclusions might even be beneficial to these properties. This is due to their ability to promote the formation of acicular ferrite (AF), which is expected to improve the toughness, especially in weld metals and also in heat-affected zones. A lot of research has been done on several inclusion types and their ability to

nucleate AF and some of the most promising ones have been: Ti_2O_3 , TiO_2 , $(\text{Ti},\text{Mn})_2\text{O}_3$, $\text{MnO}-\text{Al}_2\text{O}_3$, and complex inclusions of the mentioned oxides together with MnS and/or TiN [14], [15], [47]–[50].

There are many theories about the ensuing mechanism and how inclusions induce the nucleation of AF, such as destruction of the crystal structure, creation of dislocation arrays, reduction of lattice mismatch and chemical changes in the local matrix [14]. However, it is suggested that these mechanisms often occur simultaneously [15].

Regarding inclusions consisting of MnO and/or MnS components, a popular theory is a local depletion of Mn in the steel matrix around the inclusion [50]–[52]. Mn either diffuses into the inclusion or precipitates as MnS on the surface of the oxide [50]–[52]. This way, the content of Mn in the matrix decreases, which leads to an increase in the ferrite transformation temperature in the immediate vicinity of the inclusion, which in turn triggers the nucleation of ferrite on the inclusion instead of grain boundaries [50]–[52].

However, in order to have a beneficial effect on toughness, inclusions should remain moderate in size, since coarse inclusions typically worsen toughness properties. Regarding AF formation, the optimal inclusion size has been reported to vary between $0.25\ \mu\text{m}$ and $3\ \mu\text{m}$ [14], [15], [49]. Taking into account the degrading effect of coarse inclusions on toughness properties, an inclusion size of $1\ \mu\text{m}$ has been suggested as optimal [14].

It should be noted that the formation of AF is not only dependent on inclusions, but other factors simultaneously affecting its formation are prior austenite grain size, steel composition and cooling rate [14], [15].

3 Materials and methods

This work uses different types of steels which are presented in this chapter. Additionally, the methods used to characterize the microstructural features as well as the mechanical properties of the studied steels are described here.

3.1 Materials

The materials in this work are roughly divided into two main categories: ultra-high-strength steels studied in Publication I, and high-strength offshore steels studied in Publications II–IV. All studied steels were rather experimental compared to commercial steels and their chemical compositions are presented in Table 1.

In the case of ultra-high-strength steels, the research was conducted focusing on the base material properties, while in the case of offshore steels, the primary interest concerned characterization of the simulated heat-affected-zones.

3.1.1 Ultra-high-strength steels

The studied ultra-high-strength steels were principally of the same chemical composition but with different levels of impurities (S, O, N), see Table 1. There were also slight differences in the levels of Ca and Al contents.

The steels were hot rolled from slabs of 200 mm thickness to plates of 12 mm thickness. The final rolling temperature was 930 °C and the subsequent cooling rate during direct quenching after the final rolling pass was about 50–70 °C/s down to room temperature.

The yield and ultimate tensile strengths of the steels were approximately 1000 MPa and 1300 MPa, respectively.

3.1.2 High-strength offshore steels

The high-strength offshore steels comprising of two 500 MPa steels with different alloying compositions were studied in Publication II, while three different compositions of 420 MPa steels were studied in Publications III and IV.

The 500 MPa steels studied in Publication II were laboratory hot rolled pieces cut approximately from the centreline of industrial scale continuously cast slabs. The dimensions of the pieces were 180 × 80 × 55 mm³, and they were hot rolled to the thickness of 9 mm. The finish rolling temperature was targeted to 820 °C,

followed by water cooling to 400 °C with a cooling rate of 30 °C/s and subsequent air cooling to room temperature with a cooling rate of ≤ 0.3 °C/s.

The 420 MPa steels studied in Publications III and IV were laboratory casts using a vacuum induction furnace. The 85 kg ingots were soaked at 1200 °C and hot rolled into 20 mm plates.

In these steels, the research interest concerned the heat-affected zones (HAZ) that occurred due to the thermal cycles of the welding processes. The HAZ is typically divided into different subzones e.g., intercritical HAZ (ICHAZ), subcritical HAZ (SCHAZ), fine-grained HAZ (FGHAZ), coarse-grained HAZ (CGHAZ) and intercritically reheated coarse-grained HAZ (ICCGHAZ). In this study, the research focused on the characterization of CGHAZ, which is often considered the weakest location in welded structures.

Instead of studying real welds, the formation of CGHAZs was simulated using a Gleeble 3800 thermomechanical simulator. Physical simulation enables the reliable characterization and testing of different HAZ subzones, and it is possible to simulate various types of welding methods by varying the heat input and cooling rate. In the case of welding simulation, it is common to use cooling time from 800 °C to 500 °C ($t_{8/5}$) instead of cooling rate. Between these temperatures, the microstructure of steel transforms from austenite into other phases depending on the cooling path. The chosen $t_{8/5}$ times were 6 seconds and 30 seconds in Publication II, ≈ 5 seconds, 17 seconds and 24 seconds in Publication III, and ≈ 5 seconds, 24 seconds and 64 seconds in Publication IV. The peak temperature was 1350 °C in all cases and the holding time at the peak temperature was 0.1 second. In Publication II, the heating rate was 100 °C/s and the free span was 20 mm, while in Publications III and IV, the heating rate was 300 °C/s and the free span was 9 mm. While the applied cooling model was Rykalin 2D in Publication II, Rykalin 3D model was applied in Publications III and IV.

Table 1. Chemical composition of the studied steels (wt.%); balance Fe.

Material	Publication	Element content (wt.%)														
		C	Si	Mn	Al	Nb	V	Ti	P	S	N	O	Ca	Cr	Mo	B
UHSS A	I	0.15	0.3	1.0	0.031	-	-	0.015	0.01	0.0018	0.0055	0.0018	0.0015	0.4	0.1	0.0015
UHSS B	I	0.15	0.3	1.0	0.053	-	-	0.015	0.01	0.0007	0.0035	0.0013	0.0022	0.4	0.1	0.0015
Steel A1	II	0.02	0.38	1.5	0.03	0.03	0.008	0.012	-	0.0024	0.0056	0.0017	0.0023	*	*	-
Steel A2	II	0.02	0.38	1.5	0.03	0.03	0.008	0.012	-	0.0014	0.0045	0.0008	0.0023	*	*	-
Steel B1	II	0.07	0.3	1.3	0.03	0.03	0.01	0.013	-	0.0016	0.0054	0.0017	0.0025	**	**	-
Steel B2	II	0.07	0.3	1.3	0.03	0.03	0.01	0.013	-	0.0012	0.0043	0.0012	0.0025	**	**	-
Al _{ref}	III, IV	0.05	0.01	1.6	0.037	0.01	0.01	0.016	0.005	0.003	0.006	0.0023	-	***	***	-
T _{high}	III, IV	0.05	0.03	1.7	0.002	0.01	0.07	0.027	0.005	0.003	0.006	0.0080	-	***	***	-
T _{low}	III, IV	0.05	0.23	1.7	0.003	0.01	0.07	0.016	0.007	0.003	0.008	0.0047	-	***	***	-

*Cr + Mo = 0.44 wt.%; **Cr + Mo = 0.07 wt.%; *** Cr, Mo, Cu, Ni in equal proportions.

3.2 Microstructural characterization

The microstructures of the studied steels were characterized using the equipment of Materials and Mechanical Engineering as well as those of the Centre for Material Analysis at the University of Oulu. Additionally, inclusion measurements were carried out at SSAB Europe in Raahе, Finland.

3.2.1 General microstructural characterization

General microstructural characterization of the studied steels in Publications I, II and IV was performed on Nital-etched cross-sectional samples using a Zeiss Sigma field emission scanning electron microscope (FESEM) operated at 5 kV acceleration voltage and using a working distance of approximately 5 mm. Additionally, a Keyence VK-X200 laser scanning confocal microscope (LSCM) was used for microstructural characterization of Nital-etched samples in Publication II.

The prior austenite grain size (PAGS) of the steels studied in Publication I was examined using the LSCM after etching with saturated picric acid in soap solution.

Fracture surfaces of the tested samples were also examined using the Zeiss Sigma FESEM (Publications I, II and IV) as well as the LSCM (Publication I).

In order to define the average effective grain size and grain boundary misorientation distribution, EDAX electron backscatter diffraction (EBSD) imaging was utilized on the FESEM with an acceleration voltage of 15 kV. The area and step size for the EBSD measurements varied in different Publications due to different microstructures that required adjustment of the settings to obtain the most reasonable measurements. Grain boundaries which had misorientation greater than 15° were considered as effective grain boundaries and the equivalent circular diameter (ECD) was used to define the effective grain size. Three pixels were filtered from the original acquisitions in order to mitigate the frequency of minuscule grains typically encountered with EBSD. In Publications III and IV, the quantitative microstructural features were defined using an image quality (IQ) analysis technique on the EBSD images.

The data acquired by EBSD was also utilized to define the PAGS in Publications III and IV with the help of MATLAB software and supplemented with the MTEX toolbox.

The fraction of retained austenite in Publication IV was determined using a Rigaku SmartLab X-ray diffractometer (XRD) with Co K α radiation. The acceleration voltage was 40 kV, the current was 135 mA, the scan speed was 7.1945° per minute and the step size and range were 0.05° and 45° > 2 θ > 130°, respectively. The comparative retained austenite fraction was acquired via the EBSD, too.

3.2.2 Inclusion measurements

The inclusion contents of the studied steels were measured at SSAB Europe, Raahе, Finland, using a FESEM (Jeol JSM-7000F) equipped with an energy dispersive spectrometer (EDS). The acceleration voltage was 15 kV and the current was 3.5 nA. The data was acquired and analysed using the Oxford INCA software. The working distance was 10 mm and each inclusion was measured for 1 second of time. In Publications I and II, the inclusions were analysed on cross-sections containing the rolling direction (RD) and normal direction (ND), while in Publications III and IV, inclusions were studied on simulated CGHAZs and on cross-sections containing the transverse direction (TD) and ND. The acquired data included information about the number, location, size, shape and chemical composition of the inclusions. The size of the inclusions was determined using their maximum length and the minimum inclusion size included in the results was 1 μ m.

Two different inclusion classification methods were utilized. In Publications I and II, inclusions were classified using the system developed at SSAB Europe, Raahе, Finland, where certain most commonly detected elements exceeding the limit of 5 wt.% in the inclusion were included in the determination of the chemical compounds of the inclusions.

The classification method used in Publications III and IV was developed at University of Oulu [53], which utilized the ratios between the considered elements instead of absolute values and classified inclusions according to the molar fractions of components, such as Al₂O₃, MnO, MnS, TiN and TiO₂.

3.3 Mechanical testing

The main mechanical properties considered in this research were yield strength, ultimate tensile strength, ductility, impact toughness and hardness, but fracture toughness was additionally considered in Publication II. Strength and hardness were mainly measured in order to verify the strength grades of the studied steels and to observe the effect of transformed microstructures in the simulated heat-

affected zones. In addition, any increase in strength and hardness is generally known to decrease the toughness, so these are some of the variables used in studying the effects of different factors on toughness. The research methods and equipment are presented in the following sections.

3.3.1 Tensile testing

Tensile testing was carried out for the samples studied in Publications I and II.

In Publication I, tensile testing was performed at SSAB Europe, Raahe, Finland according to the standard EN ISO 6892-1 [54]. The round specimens had dimensions $D = 10$ mm and $L_0 = 80$ mm and they were cut both in longitudinal and transverse directions of rolling. Five specimens of each variant were tested in both directions. Yield strength (YS), ultimate tensile strength (UTS) and reduction of area (RA) were determined from the results.

For Publication II, tensile testing was performed at the University of Oulu using 12 mm wide and 8 mm thick flat specimens. The gauge length was 75 mm, and the specimens were cut parallel to the rolling direction. Testing was not possible transverse to the rolling direction due to the inadequate width of the laboratory hot rolled plates. A minimum of three specimens were tested per variant. YS, UTS and elongation to fracture were determined. Tensile testing was only performed on the base material.

3.3.2 Charpy V-notch impact toughness testing

Charpy V-notch (CVN) impact toughness testing was carried out at SSAB Europe, Raahe, Finland for Publications I and II, and standardized instrumented CVN tests at Lapland University of Applied Science, Kemi, Finland for Publication IV.

In Publication I, $10 \times 10 \times 55$ mm³ specimens were tested at various temperatures ranging from -60 °C to 100 °C in accordance with EN ISO 148-1 standard [55]. The specimens were machined both in longitudinal and transverse directions and three specimens were tested at each temperature in both directions. The absorbed impact energy at -40 °C and the upper shelf energy (USE) were determined from the results.

The CVN tests for Publication II were performed using sub-sized $5 \times 10 \times 55$ mm³ specimens transverse to the rolling direction (TD). Tests were carried out in accordance with EN ISO 148-1 standard [55], and the testing temperature ranged from -160 °C to 40 °C. Exponential-fitted ductile-brittle transition temperature

range with impact toughness transition temperatures (T_{35}) and upper shelf energies, taking into account the correction for the sub-size specimens, were determined from the results. Two specimens were tested at each temperature for the base materials, while the simulated CGHAZ were tested with either two or three specimens at each temperature.

For Publication IV, standardized instrumented CVN impact toughness tests were carried out according to ISO 14556 standard [56]. The testing temperature range was from $-80\text{ }^{\circ}\text{C}$ to $-40\text{ }^{\circ}\text{C}$, and sub-sized $5 \times 10 \times 55\text{ mm}^3$ specimens transverse to the rolling direction were used for testing. Tests were also performed on simulated CGHAZ specimens. The difference from the normal CVN test is that by using an instrumented test, it is possible to determine the absorbed energy needed for the nucleation of the fracture crack as well as the energy needed for its propagation to complete the fracture.

3.3.3 Hardness testing

Hardness was measured at the University of Oulu using a Duramin-A300 (Struers) instrumented hardness tester using a 10 kg (100 N) load (HV_{10}). In Publications I and II, the hardness of the base materials was measured from the thickness of cross-sections parallel to the rolling direction (RD) and normal direction (ND). In Publications II, III and IV, the hardness of the simulated CGHAZ samples were measured from the centre line of the TD-ND surface and along the simulated CGHAZ.

3.3.4 Fracture toughness testing

In Publication II, fracture toughness was also studied. Testing was done at SSAB Europe, Raahе, Finland in accordance with EN ISO 12737 standard [57]. 5 mm-thick single-edge notched bend (SENB) specimens were used with an a/W ratio of 0.5 (where a is the crack length and W is the width) and with the pre-fatigued crack positioned at the centre of the simulated CGHAZ. Testing was performed at $-10\text{ }^{\circ}\text{C}$ and $-40\text{ }^{\circ}\text{C}$. Two or three specimens were tested per temperature.

4 Results

The results presented here are the summaries of the results of the corresponding results reported in Publications I–IV. The results of Publications III and IV are presented in the same chapter, since the original papers were written from the same study. Publication I dealt with the effects of inclusions on the ductility and toughness of an ultra-high-strength steel. Publication II focused on the detrimental effect of coarse titanium nitrides on the impact and fracture toughness properties of the coarse-grained heat-affected zone (CGHAZ) of 500 MPa offshore steels. Publication III presented the results concerning the effect of inclusions on inducing the acicular ferrite formation in the CGHAZ of high strength offshore steels. Finally, Publication IV dealt with the impact toughness of the CGHAZ of the steels studied in Publication III, including the effects of inclusions and other factors. For chemical compositions of the steels, see Table 1 presented in Section 3.1.2.

4.1 Effect of impurity level and inclusions on the ductility and toughness of an ultra-high-strength steel

Publication I compared the ductility and toughness of two ultra-high-strength steels (originally Steel A and B in Publication I, but modified to UHSS A and B in this dissertation for clarity) with a minimum specified tensile strength of 1300 MPa. Their impurity levels were different, but the steels were otherwise similar. Impurity level was defined as a sum of the O, N and S contents, which were 91 and 55 mass ppm in UHSS A and B, respectively. This also led to different inclusion contents in the two steels.

4.1.1 Microstructures and mechanical properties

The transformation microstructure was martensitic in both the studied steels, processed via direct quenching route. There were only marginal differences in respect of prior austenite grain size (PAGS) and effective grain size between the two steels. The estimated PAGSs were 29 μm and 27 μm , and the effective grain sizes 1.27 μm and 1.43 μm of UHSSs A and B, respectively. The sizes of the coarsest grains i.e., the grain size at 90% in the cumulative size distribution ($D_{90\%}$) were 12.20 μm and 11.67 μm , respectively, for UHSSs A and B. Additionally, the grain boundary misorientation distributions were very similar in both the steels. Fig. 5 presents the typical microstructure and prior austenite grain structure of the

studied steels. Fig. 6 presents the EBSD-images of UHSS A (a) and UHSS B (b) as well as the grain boundary misorientation distributions of both the steels (c) acquired from the EBSD data. The grain boundary misorientation distributions are typical for martensitic steels [58].

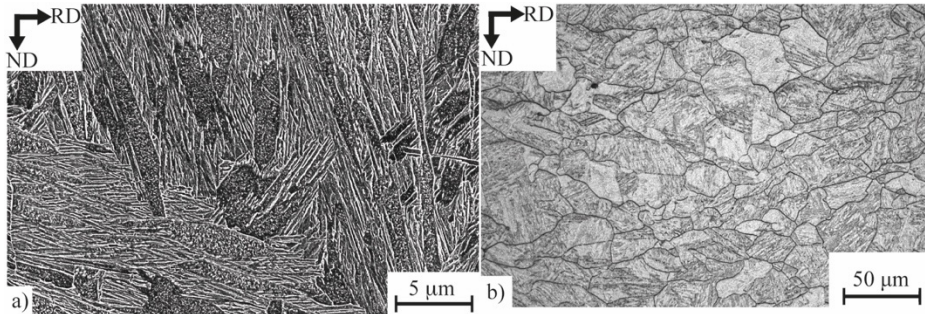


Fig. 5. Typical microstructure (a) and prior austenite grain structure (b) in studied steels (Reprinted, with permission, from Publication I © 2017 Elsevier B.V.).

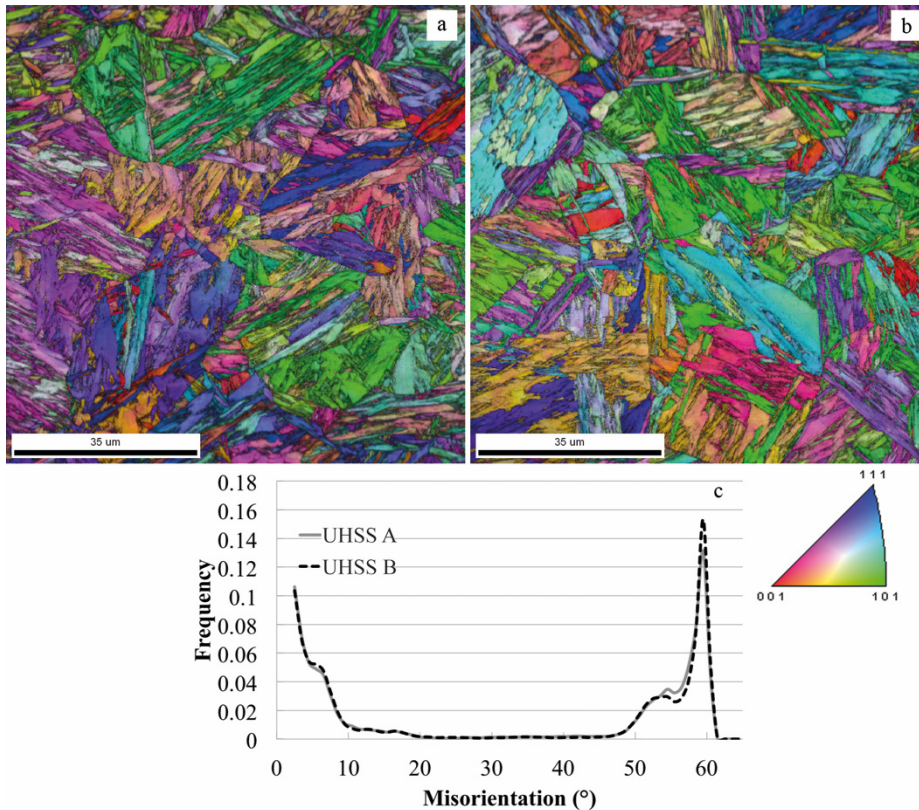


Fig. 6. EBSD-images of UHSS A (a) and UHSS B (b) as well as the grain boundary misorientation distributions of both the steels (Adapted, with permission, from Publication I © 2017 Elsevier B.V.).

The mechanical properties of the studied steels are summarized in Table 2. Tensile (R_m) and yield ($R_{p0.2}$) strengths of UHSS A were slightly higher compared to those of UHSS B. However, the total elongation, reduction of area (RA) as well as the upper shelf energy (USE) estimated through the CVN impact toughness testing, were comparatively higher in the case of UHSS B. Additionally, the ductility of UHSS A points to a strong tendency for anisotropy, as both RA and USE were clearly higher in the longitudinal direction (LT) than the transverse direction (TD). The CVN impact toughness of UHSS B at -40 °C was also higher compared to that of UHSS A, although there was only a statistical difference in TD as tested by the Student-T method. Mean hardness values were also measured for the two steels,

which turned out to be 420 ± 8 HV₁₀ and 407 ± 8 HV₁₀ for UHSS A and UHSS B, respectively.

Table 2. Mechanical properties of the studied steels (Adapted, with permission, from Publication I © 2017 Elsevier B.V.).

UHSS	Testing direction	R_m [MPa]	$R_{p0.2}$ [MPa]	RA [%]	A [%]	USE [J]	USE [°C]	CVN at -40 °C [J]
A	LT	1324±4	1032±2	63.8±1.8	13.8±0.5	134±7	60	29±15
	TD	1348±3	1050±10	54.1±2.8	11.6±0.6	*101±2	...	24±9
B	LT	1281±7	1000±8	65.3±0.5	14.0±0.5	164±4	40	40±34
	TD	1290±2	1005±4	63.9±1.8	12.8±0.2	161±2	20	39±7

*Value estimated from $(\text{absorbed energy at } 100\text{ °C}) / (0.05 + 0.95 \cdot (\% \text{ ductile fracture at } 100\text{ °C} / 100\%))^{0.72}$ because USE was not reached at 100 °C. Ductile percentage was 70 for A-TD [59].

4.1.2 Inclusions

Inclusion contents of the two steels were found to be rather different, as could be predicted from different impurity levels (the sum of S, O and N) at 91 ppm in UHSS A and 55 ppm in UHSS B. The total number density of inclusions was still only marginally different, being 80.5 mm^{-2} and 73.8 mm^{-2} in UHSS A and UHSS B, respectively. A majority of inclusions in both steels were relatively small, which accounted for the biggest fraction of the total number densities. However, only the role of coarse inclusions was highlighted, when it concerned the detrimental effect of inclusions on mechanical properties [60]. Hence, in this study, only inclusions with longest length $> 8\text{ }\mu\text{m}$ were taken into account when correlating the number density of inclusions to the mechanical properties. The length of $8\text{ }\mu\text{m}$ was chosen as a critical size based on the experimental results previously presented in the author's Master's Thesis [61], where different size of inclusions were correlated statistically with the ductility and toughness properties in similar steels. Fig. 7a shows the number density of such inclusions in the studied steels as well as the fractions of different compositional types of inclusions. It is evident that the number density of coarse inclusions was significantly higher in UHSS A (1.2 mm^{-2}) compared to that of UHSS B (0.7 mm^{-2}). Additionally, the chemical compositions of those inclusions were different in the two steels, as the majority of coarse inclusions in UHSS A were TiN and elongated MnS, while Ca-based inclusions, mainly spherical $x\text{CaO}-y\text{Al}_2\text{O}_3$ with or without CaS, were present in UHSS B. For comparison, the fraction of different types of all inclusions, including also the ones smaller than $8\text{ }\mu\text{m}$, are presented in Fig. 7b. Regarding all inclusions, there were

not big differences between UHSS A and UHSS B. A significant fraction of all inclusions in both steels were unclassified. However, nearly all of them were smaller than 8 μm . Typical coarse inclusions of these steels are presented in Fig. 8. However, TiN in Fig. 8b, even if commonly detected in UHSS A in this study, does not represent a typical cubic or rectangular shape of TiN.

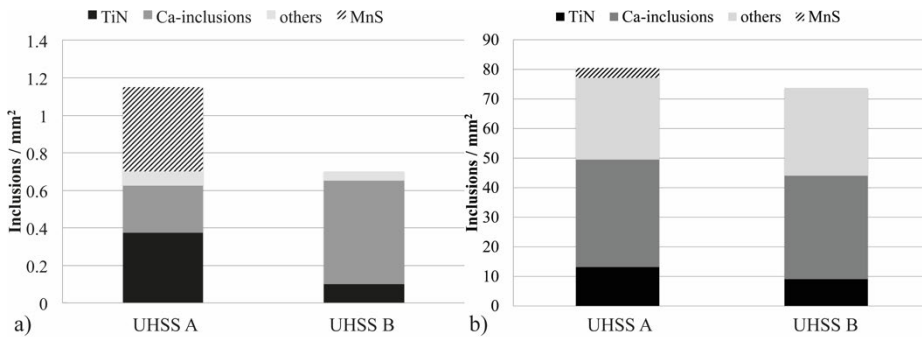


Fig. 7. The number density of coarse inclusions (>8 μm) (a) and all inclusions (b), and the fraction of different types of inclusions by chemical composition of both coarse and all inclusions in the studied steels. Ca-inclusions consist mainly of CaS, $x\text{CaO}\text{-}y\text{Al}_2\text{O}_3$, Ca-modified spinel and their combinations. Others are mainly Al_2O_3 and $\text{MgO}\text{-}\text{Al}_2\text{O}_3$. The inclusions were scanned from an area approximately 40 mm² (Adapted, with permission, from Publication I © 2017 Elsevier B.V.).

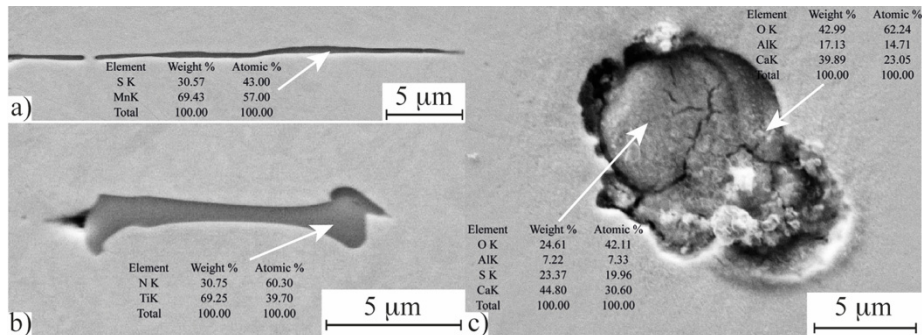


Fig. 8. FESEM-images of some typical inclusions detected in the steels: elongated manganese sulphide (a) and titanium nitride (b) in UHSS A; spherical calcium aluminate with calcium sulphide in UHSS B (c) (Reprinted, with permission, from Publication I © 2017 Elsevier B.V.).

4.2 Low-temperature toughness properties of 500 MPa offshore steels and their simulated coarse-grained heat-affected zones

The focus in Publication II was to investigate the detrimental effect of inclusions, mainly coarse TiN or (Ti,Nb)N, on the impact toughness and fracture toughness of the CGHAZ in 500 MPa offshore steels. Welded joints, and particularly heat-affected zones caused by the welding thermal cycles, are considered the most vulnerable parts of offshore structures. As such, it is essential to study and aim to improve the properties of these parts in order to meet the strict requirements for these steels [9].

Two different steel compositions were studied (A and B) and for both the steels, there were two variants with differing impurity and inclusion contents coded as: Steels A1, A2, B1 and B2 (Table 1). Additionally, two different cooling times ($t_{8/5}$) were applied when simulating the CGHAZ in order to produce microstructures similar to submerged arc welding (SAW) and flux-cored arc welding (FCAW), which are the specified welding methods for these steel types according to the standards, such as EN-10225 [8].

4.2.1 Microstructures and mechanical properties

The base material microstructures of steels A1, A2, B1 and B2 and their corresponding grain boundary misorientation distributions are presented in Fig. 9. In steels A1 and A2, the microstructures consisted of mainly quasi-polygonal ferrite, while in steels B1 and B2, the slightly higher C-content (0.07% C in Steel B and 0.02% C in Steel A) and alloying ($P_{cm} = 0.174$ in Steel B and 0.156 in Steel A) led to the formation of some bainite in the microstructure. The value of P_{cm} is used in low carbon steels instead of carbon equivalent to evaluate the weld cracking tendency and it is calculated according to the equation

$$P_{cm} = \%C + \frac{\%Si}{30} + \frac{\%Mn + \%Cu + \%Cr}{20} + \frac{\%Ni}{60} + \frac{\%Mo}{15} + \frac{\%V}{10} + \%B \times 5. \quad (1)$$

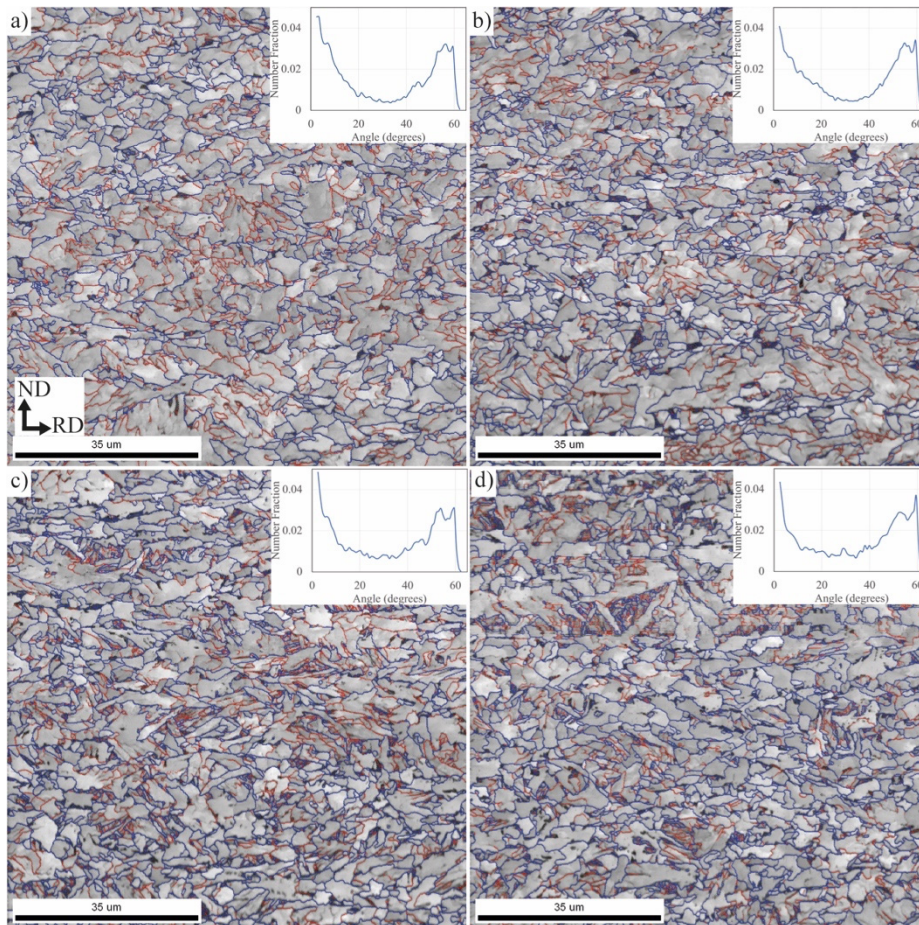


Fig. 9. Base material microstructure of Steels A1 (a), A2 (b), B1 (c) and B2 (d) as shown by EBSD. Images are taken from $\frac{1}{4}$ thickness. Blue lines indicate high-angle boundaries ($>15^\circ$), while red lines indicate low-angle boundaries ($2\text{--}15^\circ$) (Reprinted, with permission, from Publication II © 2019 Elsevier B.V.).

Due to the slight differences in the microstructures, the effective grain sizes were marginally smaller in steels B1 ($1.9\ \mu\text{m}$) and B2 ($1.8\ \mu\text{m}$) compared to those of steels A1 ($2.4\ \mu\text{m}$) and A2 ($2.1\ \mu\text{m}$), as can be discerned from Fig. 10. A similar trend was also observed in the 80th percentile ECD in the cumulative grain size distribution.

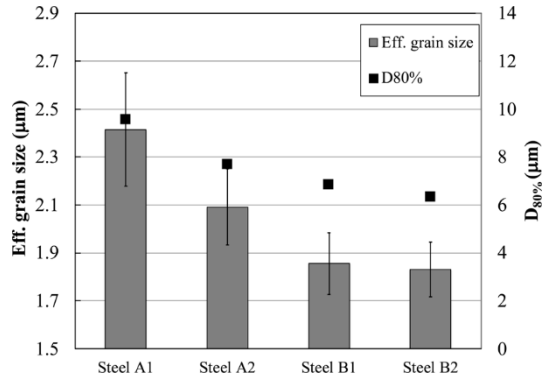


Fig. 10. The effective grain size and the 80th percentile ECD in the cumulative grain size distribution of all the measured grains in the studied steels. According to the one-way ANOVA, statistically significant differences occur between A1 and B1, A1 and B2, and A2 and B2 (Reprinted, with permission, from Publication II © 2019 Elsevier B.V.).

Fig. 11 shows the simulated CGHAZ microstructures of the studied steels using the minimum and maximum cooling times $t_{8/5} = 6$ seconds and 30 seconds. The images were obtained by employing LSCM, FESEM and EBSD. Only steels A2 and B2 were chosen to represent the microstructural characterization of steels A and B, respectively, because it was assumed that the impurity and inclusion contents would not affect the microstructures.

Using the cooling time of $t_{8/5} = 6$ seconds, the microstructure of Steel A consisted mainly of upper bainite and a small fraction of granular bainite, whereas in Steel B, the microstructure comprised of a mixture of lower bainite and martensite with a small amount of upper bainite, as can be seen in the LSCM images displayed in Fig. 11a and g, respectively. The difference in the microstructures is essentially due to the higher carbon and alloying contents of Steel B, thereby increasing its hardenability compared to that of Steel A.

Using the cooling time of $t_{8/5} = 30$ seconds, the microstructure of Steel A changed mainly to granular bainite with a small fraction of upper bainite. The microstructure of Steel B also consisted of a combination of granular and upper bainite (Fig. 11d and j, respectively).

FESEM images (Fig. 11b, e, h, k) as well as EBSD images (Fig. 11c, f, i, l) reveal more details of these microstructures. Grain boundary misorientation distributions (Fig. 12) also show the obvious differences between the CGHAZ microstructure of Steel B with $t_{8/5} = 6$ seconds and other variants of Steel A as well as Steel B. A greater fraction of grain boundaries are high angle boundaries ($\approx 50\%$ –

60°) compared to other boundaries. These charts help to confirm the microstructures identified from the microstructural images, as the grain boundary distribution of Steel B with $t_{8/5} = 6$ seconds is typical of lower bainite [62], while the distribution of the other variants is similar and pertains to upper bainite [62], [63]. The peak of about 45° is not present in the chart of Steel B with $t_{8/5} = 6$ seconds, unlike in the case of other variants. This peak indicates the presence of austenite [64].

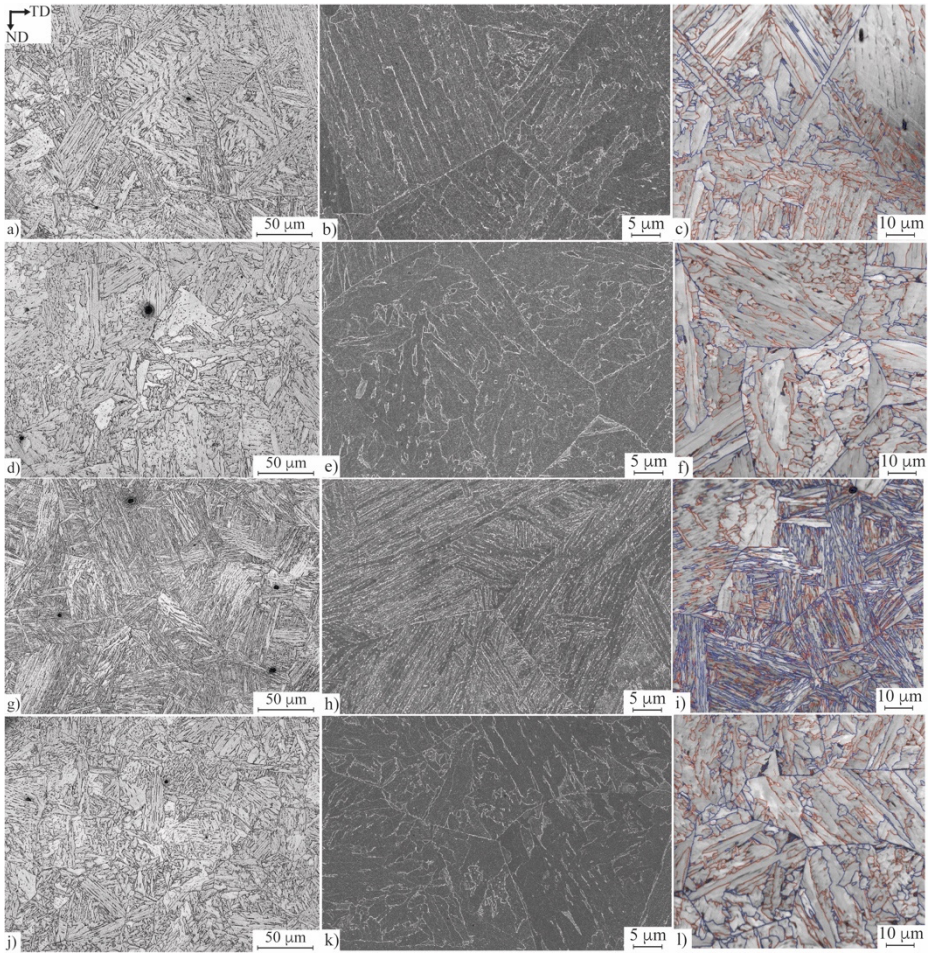


Fig. 11. LSCM, FESEM and EBSD images of simulated CGHAZ of Steel A with $t_{8/5} = 6s$ (a, b, c) and $t_{8/5} = 30s$ (d, e, f) as well as Steel B with $t_{8/5} = 6s$ (g, h, i) and $t_{8/5} = 30s$ (j, k, l). In images c, f, i and l, blue lines indicate high-angle boundaries ($>15^\circ$), while red lines indicate low-angle boundaries ($2-15^\circ$) (Reprinted, with permission, from Publication II © 2019 Elsevier B.V).

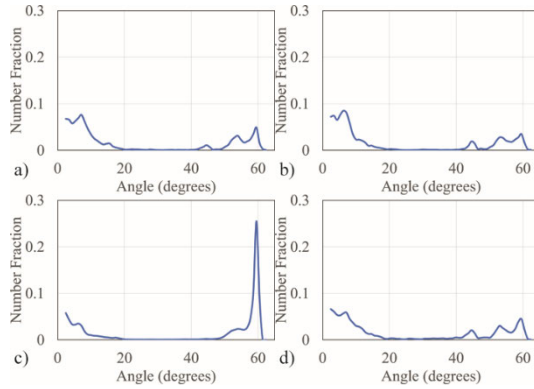


Fig. 12. Grain boundary misorientation distributions measured by EBSD from the simulated CGHAZ of Steel A with $t_{8/5} = 6\text{s}$ (a) and $t_{8/5} = 30\text{s}$ (b) as well as Steel B with $t_{8/5} = 6\text{s}$ (c) and $t_{8/5} = 30\text{s}$ (d) (Reprinted, with permission, from Publication II © 2019 Elsevier B.V.).

More differences between the variants of the two steels are revealed by observing the grain sizes (Fig. 13). Both the average effective grain size and the 80th percentile grain size in the cumulative distribution are significantly smaller in CGHAZ of Steel B with $t_{8/5} = 6$ seconds than in other variants. The reason for the difference is the lower bainitic and partly martensitic microstructure in Steel B with $t_{8/5} = 6$ seconds, thus providing a lot of high angle boundaries inside the prior austenite grains. In other variants, the high angle boundaries are mainly prior austenite grain boundaries, whereas the boundaries inside the prior austenite grains are mostly low angle boundaries that do not contribute to the effective grain size as defined in the measurement.

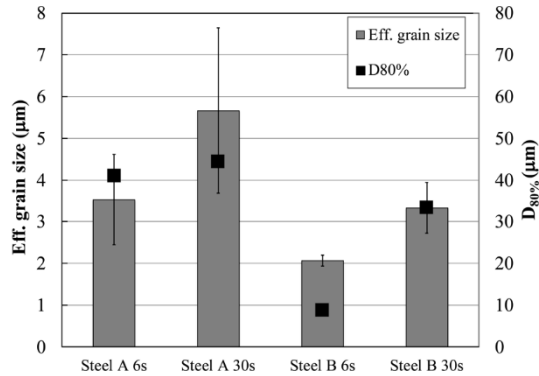


Fig. 13. The effective grain size and the 80th percentile ECD in the cumulative grain size distribution of all the measured grains in the studied steels. According to the one-way ANOVA, statistically significant differences occur between Steel B 6s and all other variants (Reprinted, with permission, from Publication II © 2019 Elsevier B.V.).

The mechanical properties of the base metals of the studied steels are presented in Table 3. The yield strength ($R_{p0.2}$) was slightly lower than the nominal 500 MPa. The tensile tests for this study were performed in the longitudinal direction, while previously in similar steels, slightly higher strength has been observed when tested in transverse direction. Further explanation might stem from the usage of the laboratory scale hot rolling and its differences from the commercial scale hot rolling. Marginally higher hardness values of Steel B compared to Steel A can be related to the higher carbon content in Steel B. CVN impact toughness properties in respect of upper shelf energy (USE) and transition temperature (T_{35}), as well as the elongation obtained from the tensile tests, indicate that the base material had sufficient toughness and ductility for applications in harsh, cold climate conditions.

Table 3. Mechanical properties of the base materials of the studied steels (Adapted, with permission, from Publication II © 2019 Elsevier B.V.).

Steel	Hardness [HV ₁₀]	R_m [MPa]	$R_{p0.2}$ [MPa]	A [%]	USE [J/cm ²]	T_{35} [°C]
A1	208±2	635±27	470±24	23.4±1.4	239	-146
A2	206±4	621±13	496±24	21.6±2.8	246	-154
B1	220±4	609±12	483±62	20.5±5.7	208	-132
B2	225±3	605±16	488±28	26.2±8.0	239	-160

The differences in the mechanical properties of the simulated CGHAZ are more pronounced than in the base materials for the studied steels. Table 4 presents the

hardness data of the simulated CGHAZ for different steel variants. Using the short cooling time $t_{8/5} = 6$ seconds, the hardness of both Steel A and Steel B increased compared to the base material. However, in Steel B, the increase in hardness is remarkably higher. Using the long cooling time $t_{8/5} = 30$ seconds, the hardness of both Steel A and Steel B remained close to that of the base material. Tensile tests were not performed for the simulated CGHAZ. However, tensile strength in steels generally correlate with the hardness by a factor of 3.2. Based on this, the estimated tensile strength using $t_{8/5} = 6$ seconds works out to be approximately 750 MPa and 900 MPa for Steels A and B, respectively. In the case of $t_{8/5} = 30$ seconds, the estimated tensile strength of both steels was close to that of the base materials, i.e., between 600–650 MPa.

Table 4. Hardness of the simulated CGHAZ of the studied steels (Adapted, with permission, from Publication II © 2019 Elsevier B.V.).

Hardness	Steel A1	Steel A2	Steel B1	Steel B2	Steel A1	Steel A2	Steel B1	Steel B2
	6s	6s	6s	6s	30s	30s	30s	30s
[HV ₁₀]	239±7	235±4	280±6	274±9	214±6	202±6	210±5	208±2

Fig. 14 shows the CVN impact toughness results of the simulated CGHAZ of the studied steels. Upper shelf energies were approximately at the same level or even a bit higher compared to those of the base materials for all variants (250–300 J/cm² vs. 208–246 J/cm², respectively). Using $t_{8/5} = 6$ seconds (Fig. 14a), Steels A1 and B1 had excellent ductile-brittle transition temperature (T_{35}) below -100 °C, while the transition temperatures were significantly higher in the case of Steels A2 and B2 (-67 °C and -77 °C, respectively). Using the longer cooling time, $t_{8/5} = 30$ seconds, the impurity content played an inconsequential role, since the variants of Steel A displayed better impact toughness compared to those of Steel B regardless of the impurity contents. The transition temperatures were -85 °C and -67 °C in the case of Steels A1 and A2, respectively, and marginally higher at -52 °C and -41 °C in the case of Steels B1 and B2, respectively.

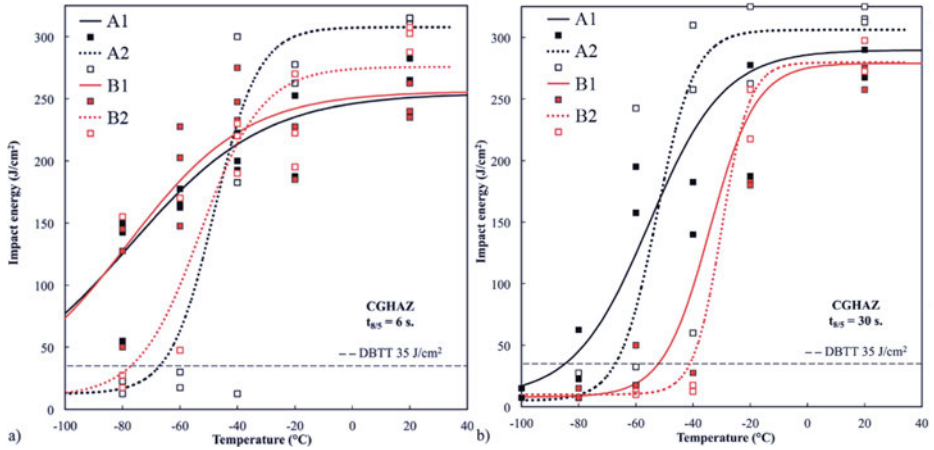


Fig. 14. CVN impact toughness of the simulated CGHAZ of the studied steels with $t_{8/5} = 6$ s (a) and $t_{8/5} = 30$ s (b). Marks indicate single test results and lines show the fitted transition curves. The approximation of T_{35} for Steels A1 and B1 with $t_{8/5} = 6$ s is < -100 °C since the lower shelf was not achieved in the test (Reprinted, with permission, from Publication II © 2019 Elsevier B.V.).

Fracture toughness data of the simulated CGHAZ of the studied steels is presented in Fig. 15. Similar to impact toughness, the best fracture toughness was achieved for Steel A1 using $t_{8/5} = 6$ seconds. On the other hand, Steel A2 had poor fracture toughness when the short cooling time was applied. Using $t_{8/5} = 30$ seconds, both variants of Steel A had relatively good fracture toughness but there was a lot of scatter in the results. All variants of Steel B had poor fracture toughness at -40 °C regardless of the impurity content or the applied cooling time. Fig. 15 also shows the features that were identified causing the premature failures in each material variant. This will be discussed further in Chapter 5.

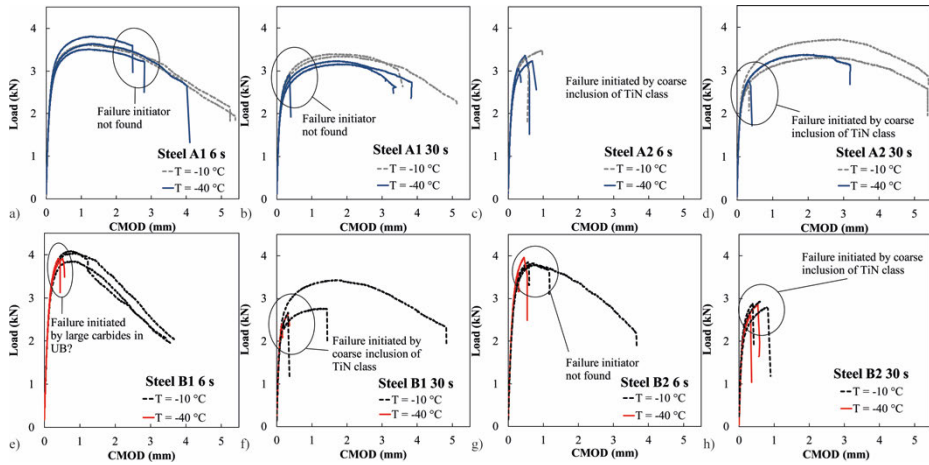


Fig. 15. Fracture toughness test results for the simulated CGHAZ of the studied steels with the two $t_{8/5}$: Steel A1 6s (a), Steel A1 30s (b), Steel A2 6s (c), Steel A2 30s (d), Steel B1 6s (e), Steel B1 30s (f), Steel B2 6s (g), Steel B2 30s (h) (Reprinted, with permission, from Publication II © 2019 Elsevier B.V.).

4.2.2 Inclusions

Inclusion size distributions according to number density and area fraction of inclusions are presented in Fig. 16a and b, respectively. Steel A had more inclusions than Steel B, especially in the size classes 2.8–5.8 μm .

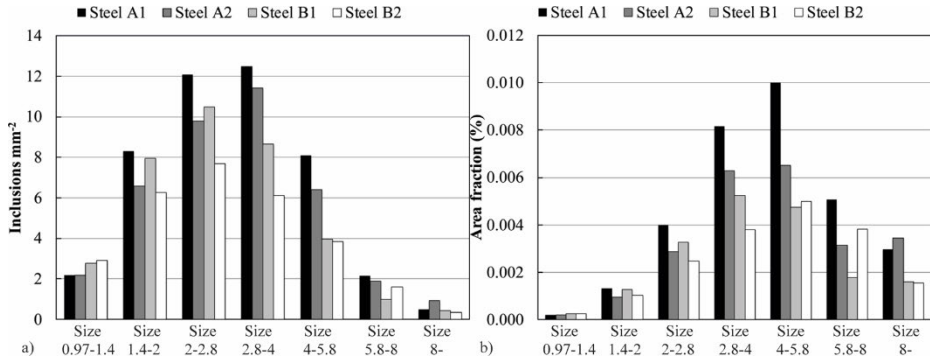


Fig. 16. Number density (a) and area fraction (b) of inclusions in the studied steels, classified according to their longest length. The inclusions were scanned from an area approximately 36 mm² (Reprinted, with permission, from Publication II © 2019 Elsevier B.V.).

In Fig. 17, the number density and area fraction of inclusions are presented according to their chemical compositions. The inclusion content of Steel A1 differed remarkably from that of the other steels. Not only Steel A1 had a greater number density and area fraction of inclusions compared to the other steels, but also the chemical compositions of the inclusions were different. A majority of inclusions in Steel A1 were Ca-based inclusions, especially MnS+Ca. These inclusions were mainly spherical, small sized (<4 μm) and evenly distributed. A few MnS inclusions, detected in Steels A1 and B1, were attributed to the slightly higher content of S in these steels compared to Steels A2 and B2. However, most sulphides were present either as (Mn,Ca)S or CaS in all steels.

It is also noteworthy that TiN inclusions, which are known to be detrimental to toughness, were completely absent in Steel A1, while other steels had differing fractions of this type of inclusion. TiN inclusions were present as coarse (>4 μm) particles in all steels except A1. An interesting point is that the number density of TiN was highest in steels A2 and B2, which had the lowest content of N among the studied steels. Steels A2, B1 and B2 generally had quite similar inclusion contents, but the number density and area fraction of inclusions were smaller in Steels B1 and B2 compared to A2. As expected from the impurity levels, number densities of inclusions detected in Steels A1 and B1 were higher compared to those of A2 and B2.

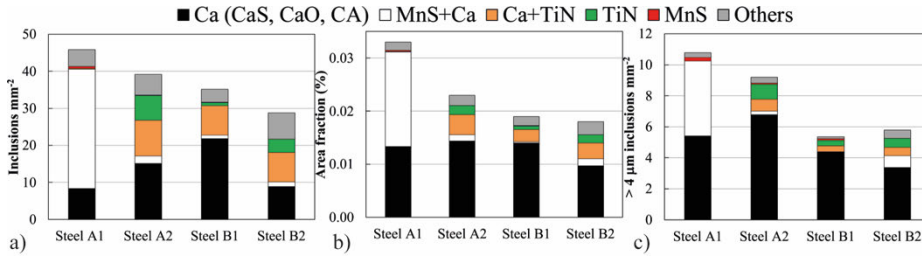


Fig. 17. Number density (a), area fraction (b) and separate number density of coarse inclusions (>4 μm) (c) in the studied steels according to their chemical composition. Ca consists of inclusions such as CaS, CaO, CaO-Al₂O₃ and their combinations. TiN also includes titanium-niobium nitrides and carbonitrides. Others are miscellaneous inclusions such as MgO and less common inclusion combinations. The inclusions were scanned from an area approximately 36 mm² (Reprinted, with permission, from Publication II © 2019 Elsevier B.V.).

TiN inclusions tend to segregate. In other words, TiN inclusions tend to form at locations with increased content of Ti. Fig. 18 shows the spatial distribution of inclusions consisting of Ti, Nb and N in the studied steels. The niobium content of these inclusions was generally between 3–10 wt.%. In Steel A2, and to a lesser extent in Steel B1, a strong concentration of TiN inclusions was observed at certain depths below the surface. The sum of %Ti + %Nb + %N (in wt.%) decreased, when TiN nucleated on the surfaces of pre-existing inclusions such as calcium aluminates or calcium sulphides. Inclusions with the sum of %Ti + %Nb + %N < 50% are not presented in the images.

Regarding the unsymmetrical spatial distributions of TiN inclusions in Steels A2 and B1, it should be mentioned that the studied pieces of steel were cut approximately from the centreline of industrial scale slabs, and subsequently hot rolled using a laboratory scale rolling mill. Therefore, the surfaces of the samples do not represent the surfaces of the original slabs but the whole thickness of the samples is near the centreline of the original slabs. In Steels A2 and B1 it looks like the concentration of these inclusions lies slightly below the geometrical centreline of the sample. This may stem from slight variation of the centreline segregation in the original slab e.g., due to soft reduction parameters, or from the slight variation of the sample location cut from the original slab.

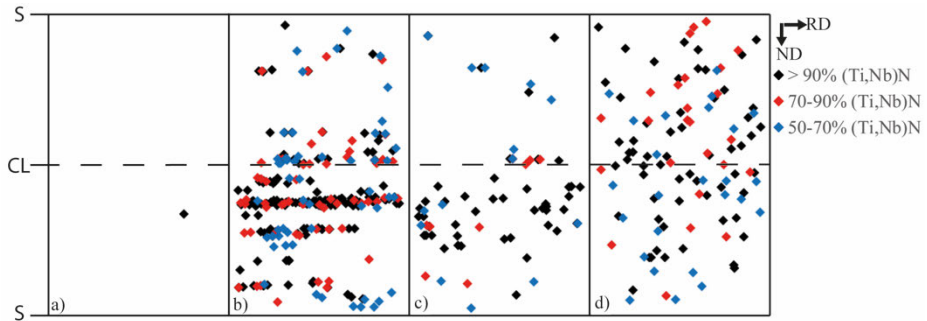


Fig. 18. Spatial distribution of TiN inclusions grouped according to the sums of %Ti + %Nb + %N being >90%, 70–90% and 50–70%, as measured in wt.% in Steel A1 (a), Steel A2 (b), Steel B1 (c) and Steel B2 (d). CL = centreline, S = surface. The inclusions were scanned from an area approximately 36 mm². The total number densities of all inclusions were 45.8 mm⁻², 39.2 mm⁻², 35.2 mm⁻² and 28.8 mm⁻² in Steels A1, A2, B1 and B2, respectively (Reprinted, with permission, from Publication II © 2019 Elsevier B.V.).

4.3 Characterization of coarse-grained heat-affected zones in Al- and Ti-deoxidized offshore steels

Publication III investigated the possibly positive effect of certain types of inclusions in promoting the nucleation and formation of acicular ferrite (AF) in the CGHAZ of offshore steels. The aim was to study the effect of different factors on the formation of acicular ferrite, with inclusion content being one of the factors. It was assumed that the toughness of the CGHAZ would be improved by increasing the fraction of acicular ferrite in the microstructure. Publication IV focused on the impact toughness of the same steels in order to clarify whether the increased fraction of AF actually improved the impact toughness, as was assumed based on the literature information.

Three different experimental steels were studied. One of the steels was Al-deoxidized reference steel (Al_{ref}), while the other two were Ti-deoxidized steels with slightly differing chemical compositions (Ti_{high} and Ti_{low}). In Publication III, the CGHAZ simulations were carried out for each steel using three different cooling times $t_{8/5} = 5$ seconds, 17 seconds and 24 seconds (rounded to the closest whole number from those used in the original paper). Another cooling time $t_{8/5} = 64$ seconds was included in Publication IV along with subsequent microstructural characterization. The specimens simulated with $t_{8/5} = 5$ seconds, 24 seconds and 64

seconds were subjected to CVN impact toughness testing at temperatures ranging from $-40\text{ }^{\circ}\text{C}$ to $-80\text{ }^{\circ}\text{C}$.

As regards the effect of inclusions, both the positive aspect of certain types of inclusions promoting AF formation as well as the negative influence of coarse inclusions deteriorating the toughness were considered.

4.3.1 Microstructures and mechanical properties

The growth of prior austenite grains following heating to peak temperatures (T_p) of $1200\text{ }^{\circ}\text{C}$ and $1350\text{ }^{\circ}\text{C}$ and subsequent water quenching, was studied since the increase in prior austenite grains size (PAGS) is known to be one of the factors promoting AF formation. The PAGS of the base materials was also measured for reference purposes. The results of the reconstructed prior austenite grains acquired from EBSD data are presented in Fig. 19. Fig. 20 shows the PAGS distribution of each variant separately. According to the images, the grain growth in all steels was still moderate at $T_p = 1200\text{ }^{\circ}\text{C}$ and the grain size distribution followed a normal distribution. However, in Steel Ti_{low} , the PAGS had already coarsened to a mean value of $52\text{ }\mu\text{m}$ from $34\text{ }\mu\text{m}$ in the base material. A slight increase was observed in Steel Ti_{high} (from $28\text{ }\mu\text{m}$ to $36\text{ }\mu\text{m}$) also, while in Al_{ref} , the mean value did not significantly change from that of the base material.

However, at $T_p = 1350\text{ }^{\circ}\text{C}$, the mean PAGS had coarsened in all the three steels, and each had many grains coarser than $100\text{ }\mu\text{m}$. The most drastic coarsening was observed in Ti_{low} , which had a mean PAGS of $225\text{ }\mu\text{m}$ and only a few whole grains were captured in the measured area, even if it was extended by combining six separate EBSD runs.

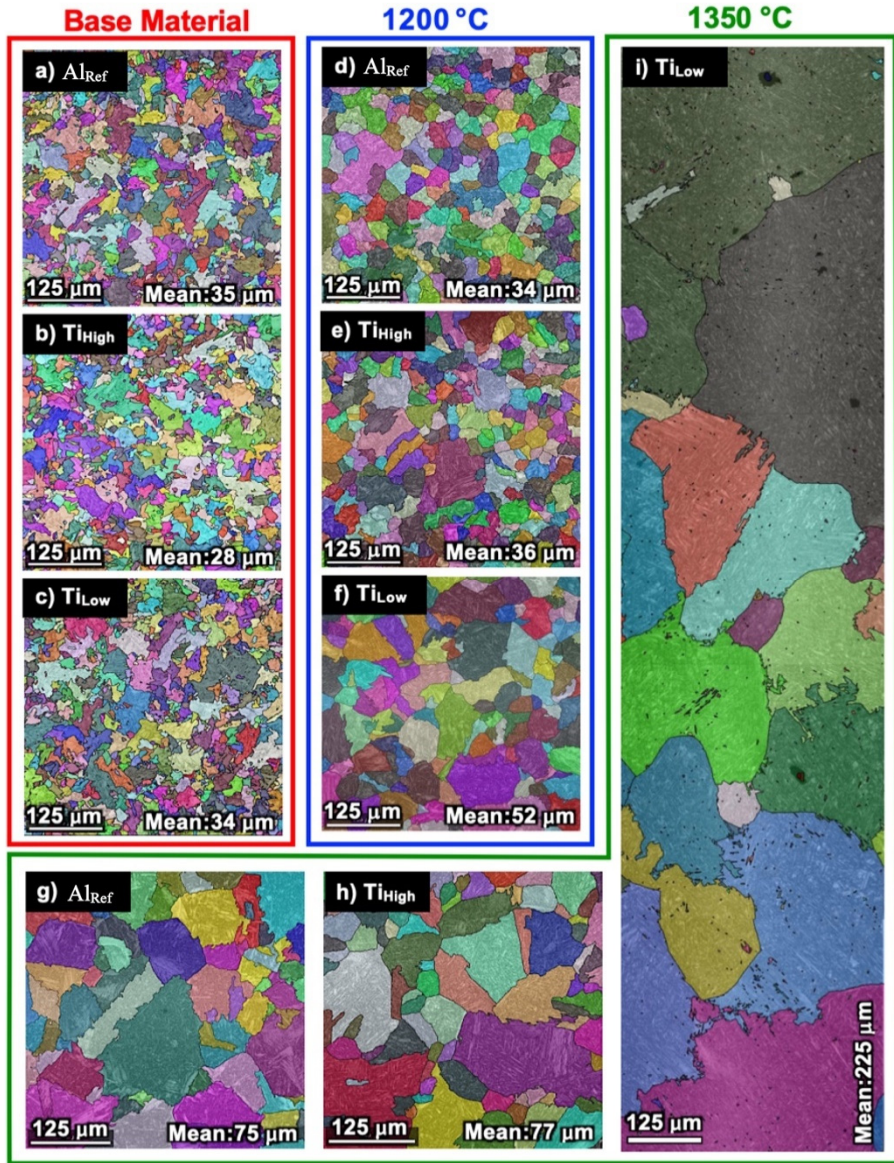


Fig. 19. Reconstructed prior austenite grains of base materials of Al_{ref} (a), Ti_{high} (b), and Ti_{low} (c); simulated HAZ with $T_p = 1200$ °C, held for 5 minutes, and subsequent water quenching of Al_{ref} (d), Ti_{high} (e), and Ti_{low} (f); and simulated HAZ with $T_p = 1350$ °C, held for 2 minutes, and subsequent water quenching of Al_{ref} (g), Ti_{high} (h), and Ti_{low} (i) (Adapted under CC BY 4.0 license from Publication III © 2020 Authors).

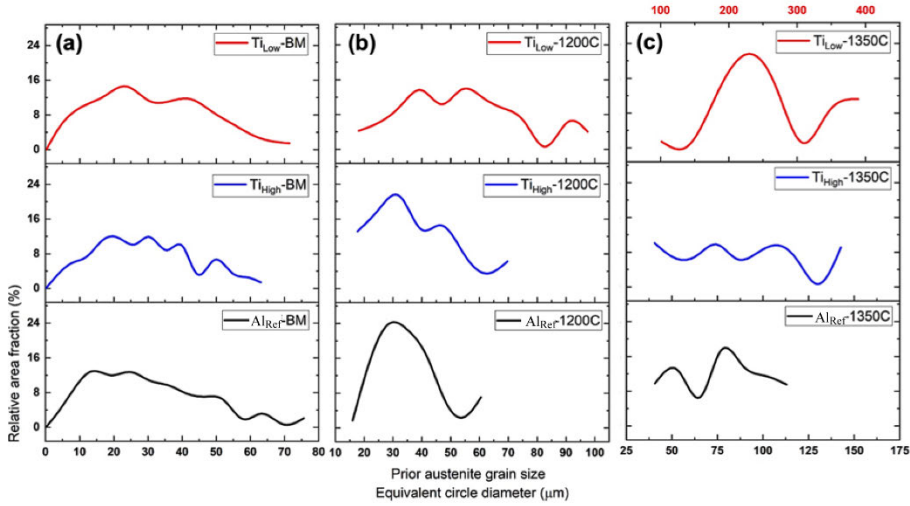


Fig. 20. Prior austenite grain size distribution of base materials (a); simulated HAZ with $T_p = 1200\text{ }^\circ\text{C}$, held for 5 minutes, and subsequent water quenching (b); and simulated HAZ with $T_p = 1350\text{ }^\circ\text{C}$, held for 2 minutes, and subsequent water quenching (c). Note the different scale in the x-axis for $T_{i\text{low}}\ 1350\text{ }^\circ\text{C}$ that appears at the top of the chart (Adapted under CC BY 4.0 license from Publication III © 2020 Authors).

The effect of cooling rate was studied thoroughly by simulating the CGHAZ using four different $t_{8/5}$ cooling times, since the cooling rate is known as one of the factors affecting AF formation in CGHAZ. Detailed microstructural characterization was carried out to quantify different microstructural components in each of the studied variants by analysing the image quality (IQ) data acquired by EBSD. The results of the simulated CGHAZ of each steel using $t_{8/5} = 5$ seconds, 17 seconds, 24 seconds and 64 seconds are presented in Fig. 21, Fig. 22, Fig. 23 and Fig. 24, respectively.

Plate-like bainite was generally the most common microstructural component, with fractions varying in the range 28–68% in all variants. AF was only observed for all applied cooling times in $T_{i\text{low}}$, where its fraction increased from 19% to 46% with the increase of $t_{8/5}$ from 5 seconds to 64 seconds. However, when $t_{8/5}$ was 64 seconds, AF had also formed in Al_{ref} and $T_{i\text{high}}$, fractions being 13% and 22%, respectively.

The increase in the fraction of AF with increased cooling time can be explained by interpreting the continuous cooling transformation (CCT) diagram, where the transformation of AF takes place between bainite and polygonal ferrite [27]. Thus, the increase in the cooling time leads to reduced factors driving bainite transformation and promotes AF transformation. However, in the case of $t_{8/5} = 24$

seconds concerning Ti_{low} , the fraction of AF was still only 28% and most of the microstructure (51%) consisted of platelike bainite. Other dominant microstructural components in the studied variants were granular bainite and lath-like bainite.

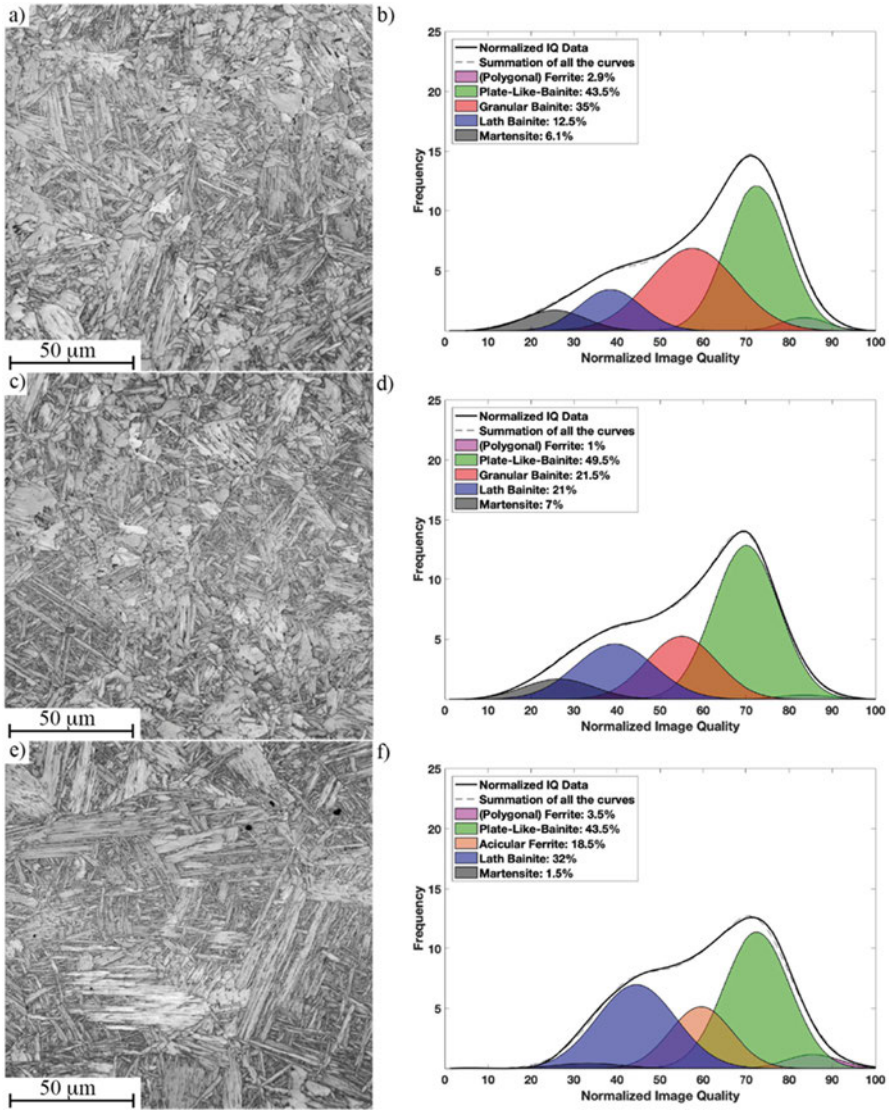


Fig. 21. Image quality analysis of simulated CGHAZs with $t_{8/5} = 5s$ in Al_{ref} (a, b), Ti_{high} (c, d), and Ti_{low} (e, f) (Reprinted under CC BY 4.0 license from Publication III © 2020 Authors).

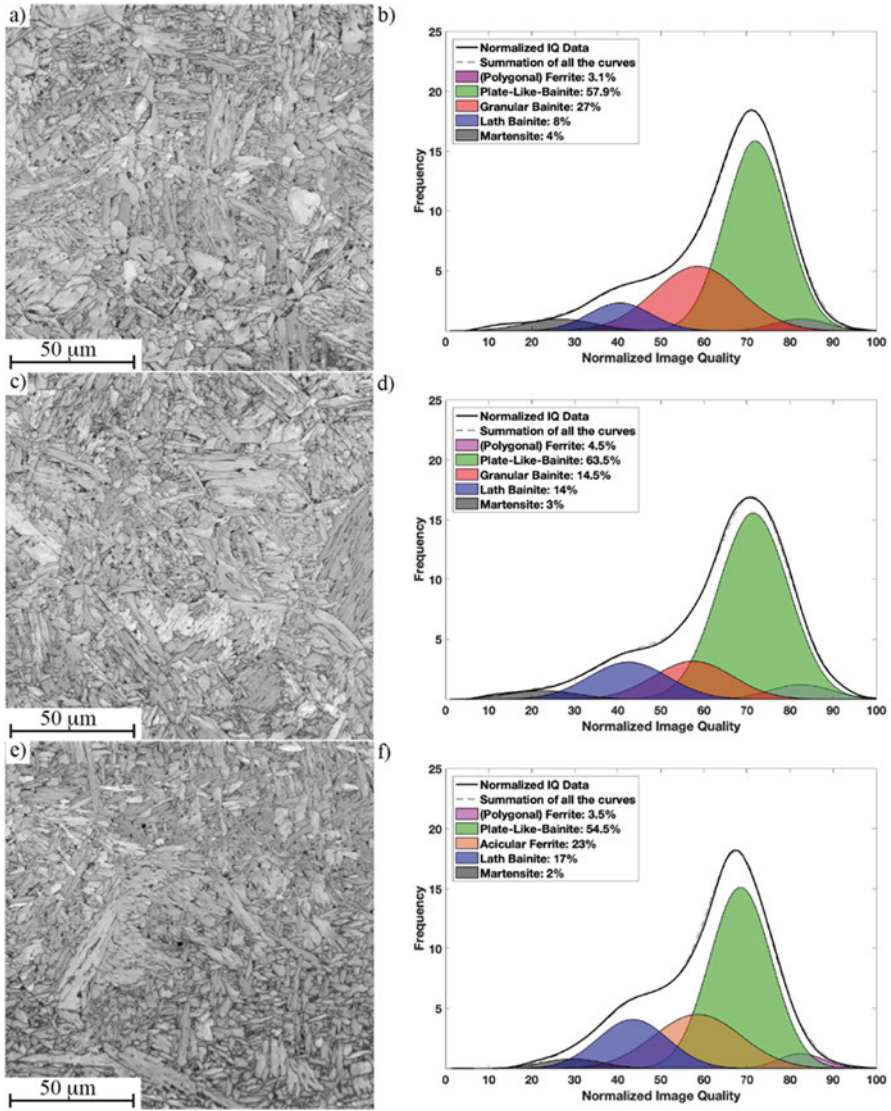


Fig. 22. Image quality analysis of simulated CGHAZs with $t_{8/5} = 17s$ in Al_{ref} (a, b), Ti_{high} (c, d), and Ti_{low} (e, f) (Reprinted under CC BY 4.0 license from Publication III © 2020 Authors).

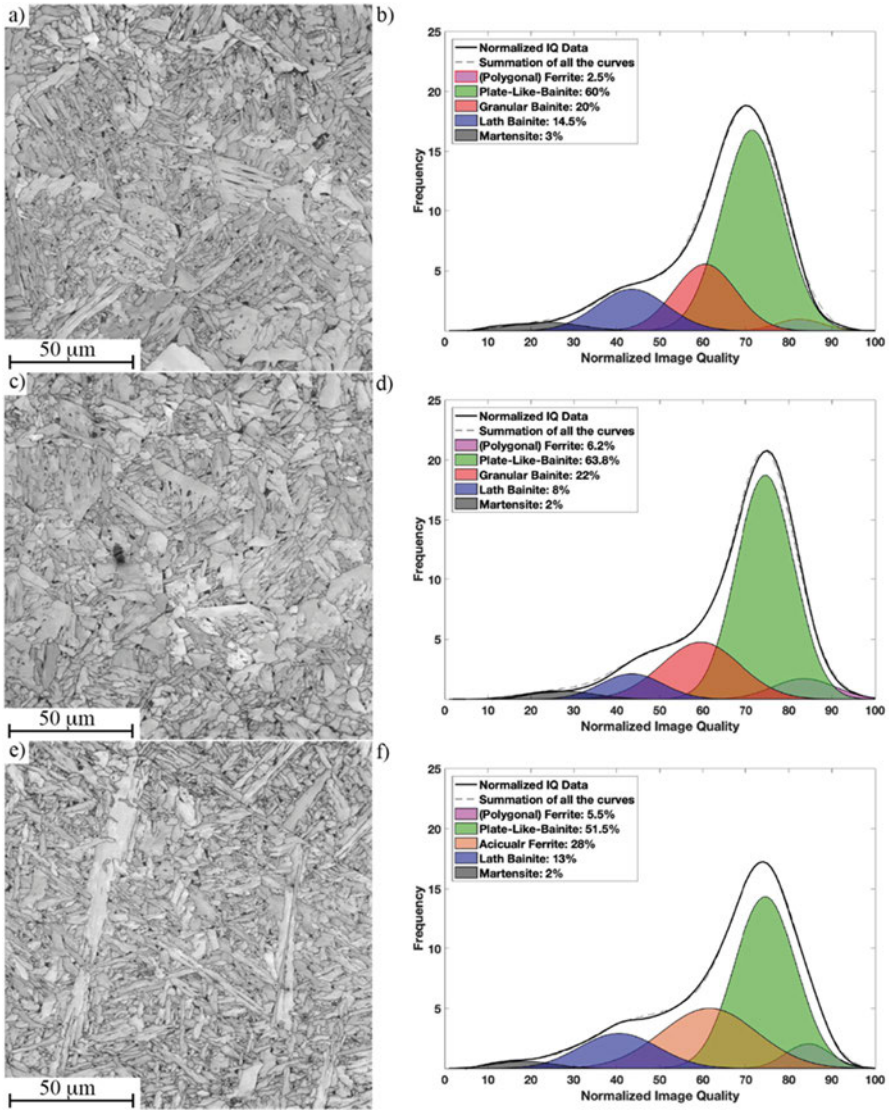


Fig. 23. Image quality analysis of simulated CGHAZs with $t_{8/5} = 24s$ in Al_{ref} (a, b), Ti_{high} (c, d), and Ti_{low} (e, f) (Reprinted under CC BY 4.0 license from Publication III © 2020 Authors).

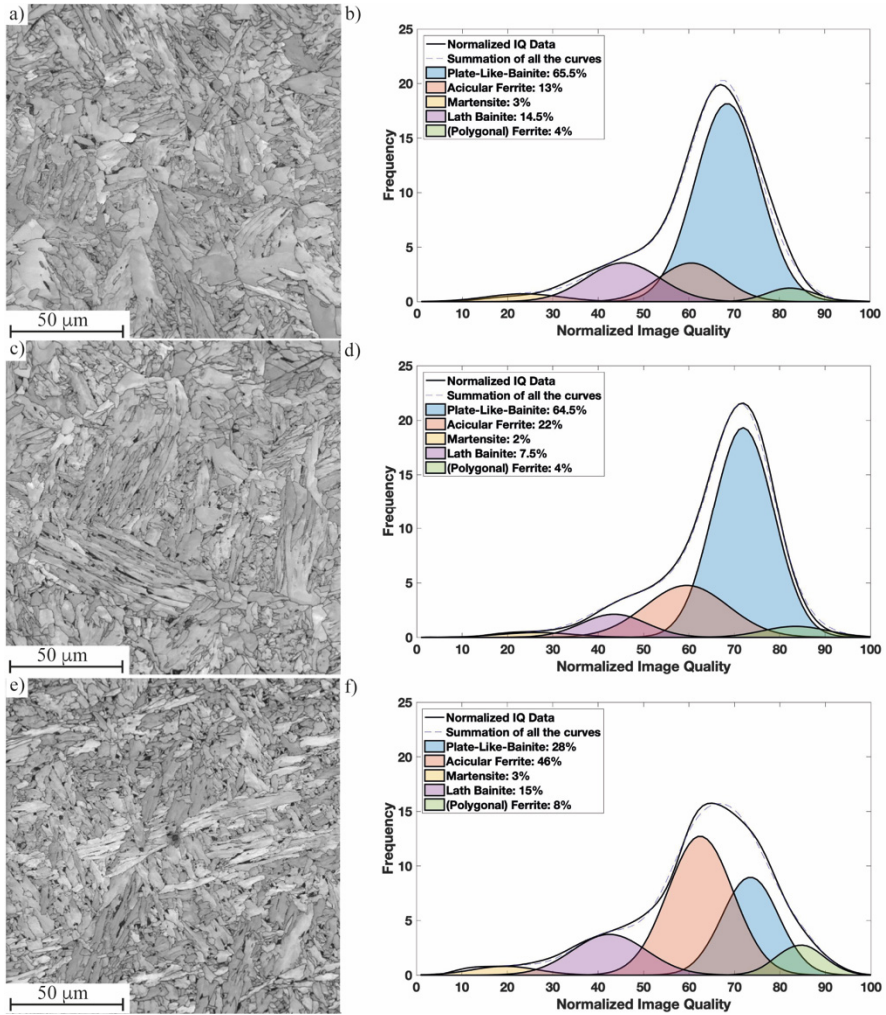


Fig. 24. Image quality analysis of simulated CGHAZs with $t_{8/5} = 64s$ in Al_{ref} (a, b), Ti_{high} (c, d), and Ti_{low} (e, f) (Reprinted under CC BY 4.0 license from Publication IV © 2021 Authors).

The validity of the IQ analysis in finding AF from the various microstructural components was checked by analysing the IQ data of an autogenous weld metal sample that mainly consisted of AF. The results of this analysis are shown in Fig. 25.

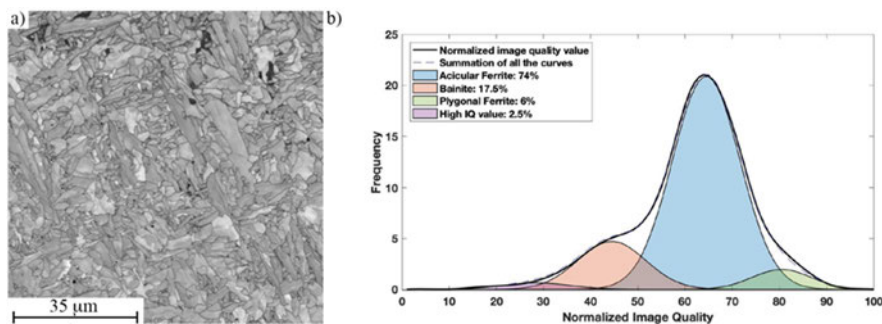


Fig. 25. Image quality analysis of weld metal in Ti_{low} with $t_{8/5} = 24s$. EBSD image (a) and normalized image quality values (b) (Reprinted under CC BY 4.0 license from Publication III © 2020 Authors).

A summary of the fractions of different microstructural components are presented in Table 5. Additionally, the fractions of retained austenite obtained through XRD measurements for specimens simulated with $t_{8/5} = 5$ seconds, 24 seconds and 64 seconds are also included in the table. The fractions of retained austenite were highest in Ti-deoxidized steels, Ti_{high} and Ti_{low} . However, the amounts of retained austenite were relatively low (approximately 1–4 %) in all variants. For comparison, retained austenite was also measured by EBSD for samples with $t_{8/5} = 5$ seconds and 64 seconds. This way, the obtained fractions of retained austenite (in vol.%) were 0.2, 0.3 and 0.2 with $t_{8/5} = 5$ seconds, and 0.4, 0.5 and 1.0 with $t_{8/5} = 64$ seconds in Al_{ref} , Ti_{high} and Ti_{low} , respectively. These fractions were significantly lower compared to the results obtained via XRD measurements due to the differences in the characterization methods, and also the resolution limit (about $0.1\mu m$) of the EBSD technique to detect very fine retained austenite grains. However, a trend can be observed: the fraction of retained austenite increased with increasing cooling time, especially in Ti-deoxidized steels. Fig. 26 shows the measured 1.0% of retained austenite by EBSD in the simulated CGHAZ of Ti_{low} with $t_{8/5} = 64$ seconds.

Table 5. Fractions of different microstructural constituents [%] in the simulated CGHAZ of the studied steels acquired by image quality analysis, and the volume fraction of retained austenite [%] acquired by X-ray diffraction [Publications III and IV] (Adapted under CC BY 4.0 license from Publication IV © 2021 Authors).

Microstructure	Al _{ref}	Ti _{high}	Ti _{low}	Al _{ref}	Ti _{high}	Ti _{low}	Al _{ref}	Ti _{high}	Ti _{low}	Al _{ref}	Ti _{high}	Ti _{low}
	5 s	5 s	5 s	17 s	17 s	17 s	24 s	24 s	24 s	64 s	64 s	64 s
Acicular ferrite	-	-	19	-	-	23	-	-	28	13	22	46
Plate-like bainite	44	50	44	58	64	55	60	64	52	66	65	28
Polygonal ferrite	3	1	4	3	5	4	3	6	6	4	4	8
Lath bainite	13	21	32	8	14	17	15	8	13	15	8	15
Granular bainite	35	22	-	27	15	-	20	22	-	-	-	-
Martensite	6	7	2	4	3	2	3	2	2	3	2	3
Retained austenite	1.5	2.0	2.3	-	-	-	1.6	3.0	4.0	1.1	3.5	3.4

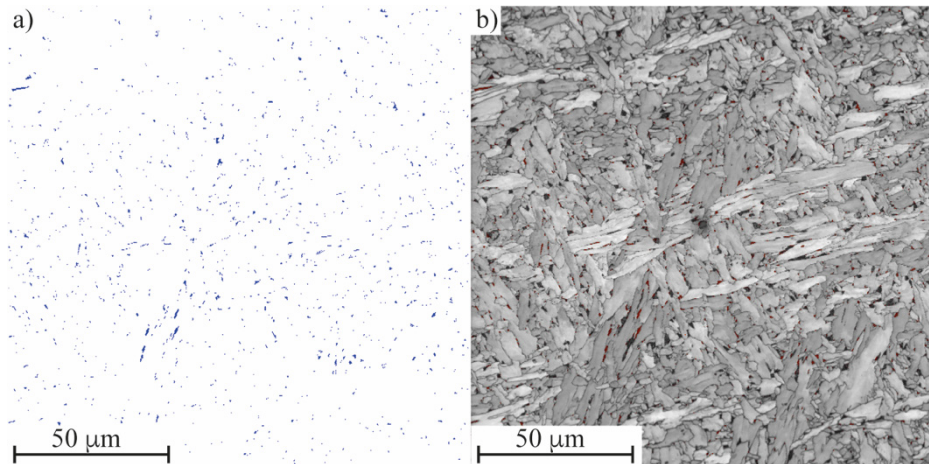


Fig. 26. Retained austenite in the ferrite matrix (a), seen together with the grains (b) in the simulated CGHAZ of Ti_{low} with $t_{8/5} = 64$ s. The blue colour indicates retained austenite in (a) and red colour in (b) (Reprinted under CC BY 4.0 license from Publication IV © 2021 Authors).

FESEM images showing the microstructures of the simulated CGHAZ specimens using the shortest ($t_{8/5} = 5$ s) and the longest ($t_{8/5} = 64$ s) cooling times of the study are presented in Fig. 27. With $t_{8/5} = 5$ seconds, the microstructure consisted mainly of fine lath-like bainite in all the studied steels. With $t_{8/5} = 64$ seconds, the microstructures consisted of plate-like bainite and ferrite. Especially in the cases of Ti_{high} (Fig. 27d) and Ti_{low} (Fig. 27f), AF was observed in remarkable fractions. AF

laths can be seen to have nucleated from inclusions. In Ti_{high} (Fig. 27d), the AF laths appeared to be somewhat coarser than in Ti_{low} (Fig. 27f).

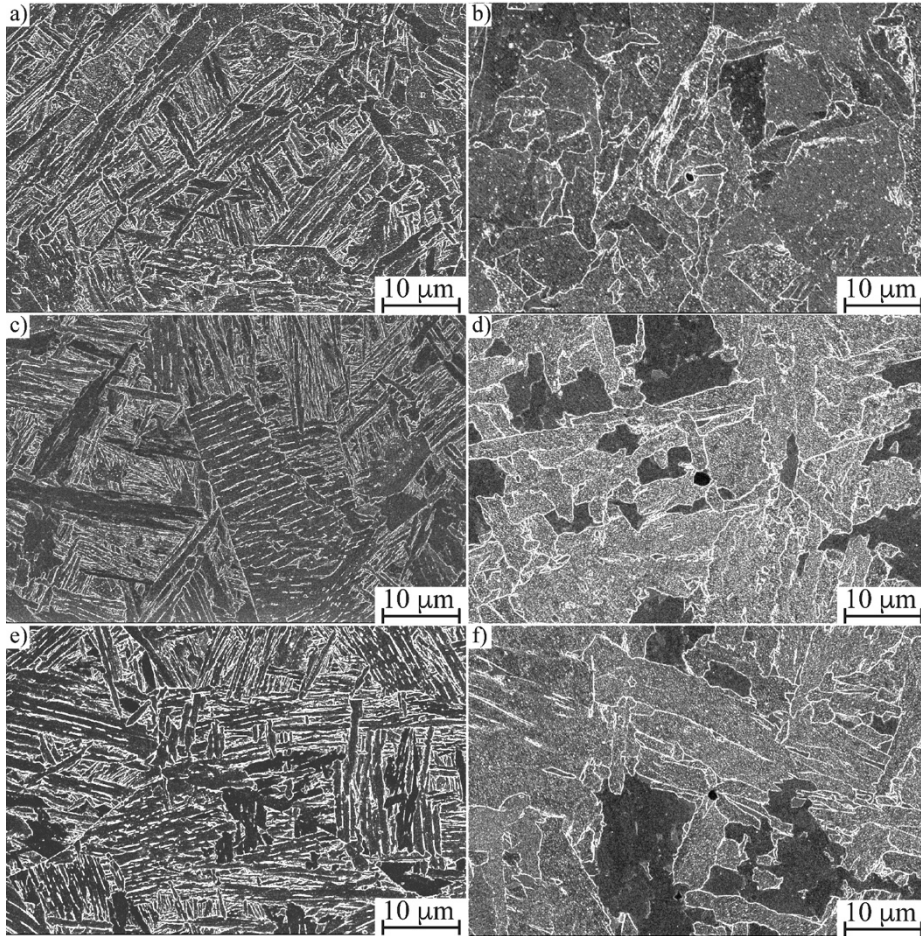


Fig. 27. FESEM images of the microstructure in the simulated CGHAZs of Al_{ref} , Ti_{high} , and Ti_{low} with $t_{8/5} = 5s$ (a, c, e) and $64s$ (b, d, f), respectively (Reprinted under CC BY 4.0 license from Publication IV © 2021 Authors).

EBSD images showing grain boundaries, together with the measured HV_{10} hardness and grain boundary misorientation distributions concerning CGHAZs of different specimens simulated with $t_{8/5} = 5$ seconds, 17 seconds and 24 seconds are presented in Fig. 28. For $t_{8/5} = 5$ seconds, the hardness of Ti_{low} (Fig. 28c) showed a

notable increase compared to Al_{ref} and Ti_{high} . This result is likely due to the coarsened PAGS in Ti_{low} , as was seen in Fig. 19i, as well as the increased fraction of lath-like bainite (Fig. 21f). Regarding the chemical composition, the higher silicon content in Ti_{low} compared to Al_{ref} and Ti_{high} (0.23% vs. 0.01% and 0.03%, respectively) improved the hardenability. Additionally, higher vanadium content in the Ti-deoxidized steels (0.07%) compared to Al_{ref} (0.01%) also promoted enhanced hardenability. With $t_{8/5} = 17$ seconds and 24 seconds, the differences between the steels were smaller but the same trend continued, i.e., Ti_{low} was the hardest and Al_{ref} was the softest. Grain boundary misorientation distributions did not reveal any noticeable difference between Al_{ref} and Ti_{high} , but Ti_{low} differed from the other two. Especially, with $t_{8/5} = 17$ seconds and 24 seconds, the grain boundary misorientation distributions resembled that of AF, as reported previously [65].

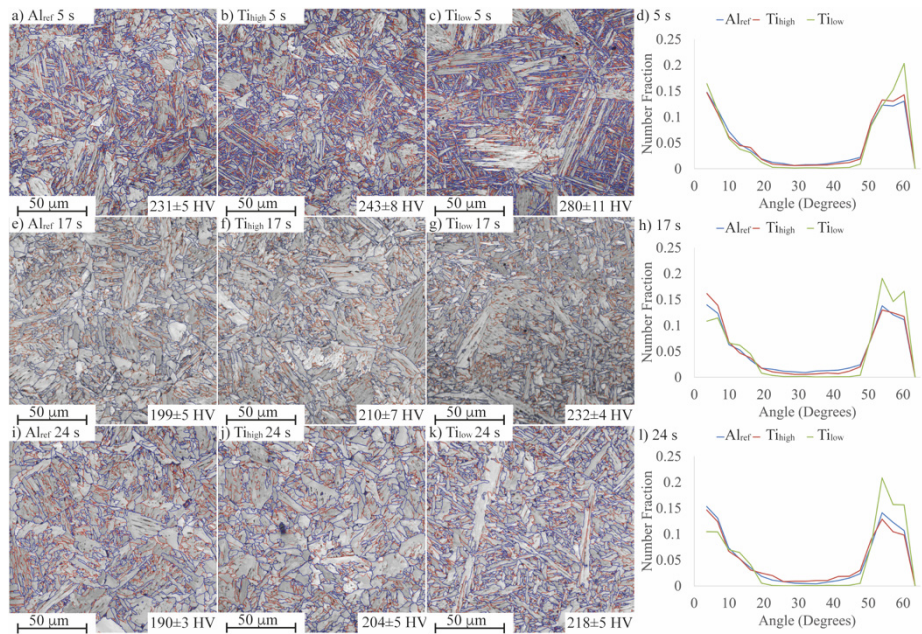


Fig. 28. EBSD images of the simulated CGHAZs with the corresponding average hardness of Al_{ref} , Ti_{high} and Ti_{low} as well as the grain boundary misorientation distributions using $t_{8/5} = 5$ s (a, b, c, d); 17 s (e, f, g, h); and 24s (i, j, k, l). In the microstructure images, blue lines indicate high-angle boundaries ($>15^\circ$), while red lines indicate low-angle boundaries ($2\text{--}15^\circ$) (Adapted under CC BY 4.0 license from Publication III © 2020 Authors).

Grain size data was also acquired from the EBSD results and are presented in Table 6. Here, the data of CGHAZs simulated with $t_{8/5} = 64$ seconds are also included, besides those shown in Fig. 28. Median values were reported instead of mean values because the grain sizes had non-normal distributions. $D_{80\%}$ values indicate the sizes of the coarsest grains in the samples, i.e., the grain size at 80% in the cumulative grain size distributions. As expected, the coarsest grains coarsened further with increasing cooling time. However, the median grain size started to decrease for specimens simulated with $t_{8/5} = 17$ seconds in Al_{ref} and Ti_{low} , and with $t_{8/5} = 24$ seconds in Ti_{high} . Both the coarsest grains and median grain sizes were smaller in Ti_{low} specimens compared to those of Al_{ref} and Ti_{high} , when simulated with $t_{8/5} = 5$ seconds and 24 seconds. Median grain size was also the smallest for Ti_{low} sample simulated with $t_{8/5} = 64$ seconds, but the coarse grains seen in Al_{ref} were the smallest. However, with $t_{8/5} = 17$ seconds, the smallest median grain size was observed for Ti_{high} , while the coarse grains seen in Ti_{low} were the smallest.

Table 6. Median grain size and grain size at 80% in the cumulative grain size distribution of the simulated CGHAZs of the studied steels [Publications III and IV] (Adapted under CC BY 4.0 license from Publication III © 2020 Authors).

Grain Size	Al_{ref}	Ti_{high}	Ti_{low}									
[μm]	5 s	5 s	5 s	17 s	17 s	17 s	24 s	24 s	24 s	64 s	64 s	64 s
Median	1.54	1.37	1.26	1.92	1.73	2.06	1.84	2.44	1.61	1.37	1.93	1.04
$D_{80\%}$	14.27	11.20	8.92	16.43	19.27	14.75	21.71	20.71	17.49	20.66	23.05	22.08

CVN absorbed impact energies of the simulated CGHAZs of the studied steels are presented in Fig. 29 and a detailed summary is provided in Table 7. At -40 °C, only the variants with $t_{8/5} = 24$ seconds were tested. Since all the steels fractured in a ductile mode at this temperature, it was decided to focus on testing at lower temperatures with the rest of the samples. However, already at -40 °C, Al_{ref} displayed a higher absorbed impact energy than Ti_{high} and Ti_{low} , and this was statistically significant.

At -60 °C and -80 °C, Al_{ref} continued to show higher absorbed impact energy compared to both Ti_{high} and Ti_{low} regardless of the applied cooling time. Particularly, the performance of Ti_{low} with $t_{8/5} = 64$ seconds was poor at -60 °C and -80 °C. However, due to the considerable scattering in the values caused by respective ductile to brittle transition zones, there were no statistical differences except that Al_{ref} with $t_{8/5} = 64$ seconds had shown the best impact toughness at -60 °C.

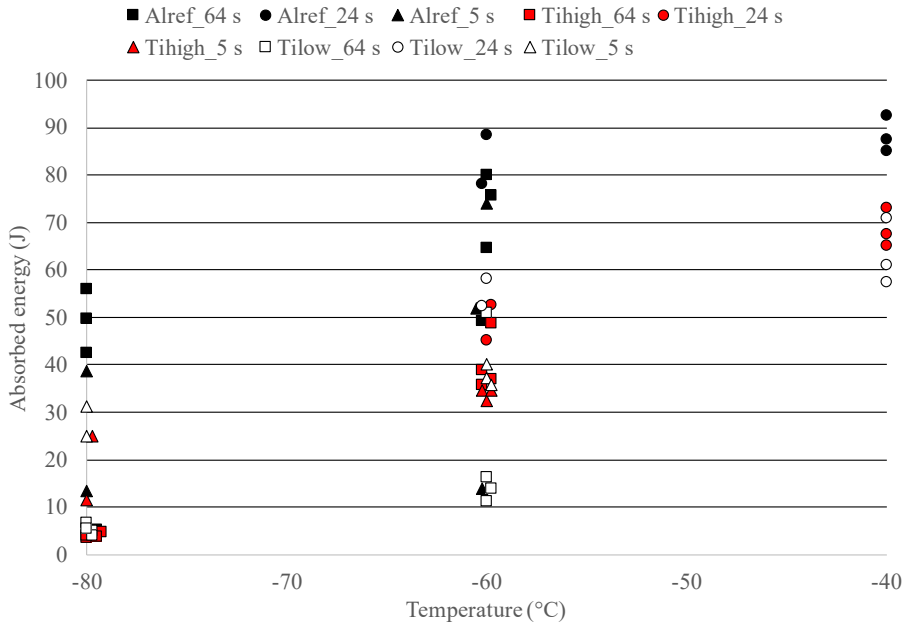


Fig. 29. CVN impact toughness results of simulated CGHAZs of the studied steels tested at three temperatures (sub-size specimens, $5 \times 10 \times 55 \text{ mm}^3$, absolute values) (Adapted under CC BY 4.0 license from Publication IV © 2021 Authors).

Table 7. Summary of the CVN impact toughness data (sub-size specimens, $5 \times 10 \times 55 \text{ mm}^3$, absolute values) (Adapted under CC BY 4.0 license from Publication IV © 2021 Authors).

$t_{8/5}$ [s]	Temperature [°C]	Al_{ref} [J]	T_{high} [J]	T_{low} [J]
5	-60	47 ± 30	34 ± 1	38 ± 2
	-80	26 ± 18	19 ± 9	28 ± 4
24	-40	$89 \pm 4^*$	69 ± 4	63 ± 7
	-60	83 ± 7	49 ± 6	55 ± 4
64	-60	$68 \pm 14^*$	40 ± 6	23 ± 19
	-80	39 ± 23	4 ± 1	5 ± 1

*Denotes a statistically significant difference to other steels (Mood's Median Test, $p < 0.05$)

The CVN impact toughness testing was performed using an instrumented machine in order to have more detailed data and better understanding regarding the behaviour of the samples during the testing. The load-displacement diagrams obtained from the tests are presented in Fig. 30, illustrating the possible occurrence of different types of fractures in the samples. Generally, Al_{ref} showed better

performance than Ti_{high} and Ti_{low} at each cooling time and test temperature. Distinctively, the curves of the Al_{ref} samples reach the highest displacement and the total area under the load-displacement curves of the Al_{ref} are also higher compared to those of Ti-deoxidized samples.

The highest maximum loads (F_m) were reached at the cooling time of $t_{8/5} = 5$ seconds, presumably due to the most hardened microstructures. However, the fracture occurred in most of the samples soon after F_m was reached, leaving the ductile propagation part of the fracture nearly absent. Al_{ref} samples did have slight ductile propagation only at -60 °C, but not at -80 °C. The crack arrest ability was observed most notably in Al_{ref} samples at -60 °C.

Samples simulated with $t_{8/5} = 24$ seconds were tested at -40 °C and -60 °C. At -40 °C, both ductile propagation and crack arrest ability were observed in all samples, but already at -60 °C, only Al_{ref} showed notable crack arrest ability, whereas tendency for ductile propagation decreased in all samples, most remarkably in Ti-deoxidized ones.

With $t_{8/5} = 64$ seconds, Al_{ref} continued to show better performance compared to Ti_{high} and Ti_{low} . Ductile propagation was observed in Al_{ref} at both -60 °C and -80 °C, while in both the Ti-deoxidized steels, there was only slight ductile propagation, even at -60 °C. Notable crack arrest ability was only seen in Al_{ref} at -60 °C. However, brittle fracture occurred at -80 °C, once the F_m was reached in both Ti_{high} and Ti_{low} , and the displacement remained extremely low.

Fractographic features of some of the specimens were studied with an aim to pinpoint the reason for crack initiation and the findings are mentioned in the graphs. However, this will be discussed later.

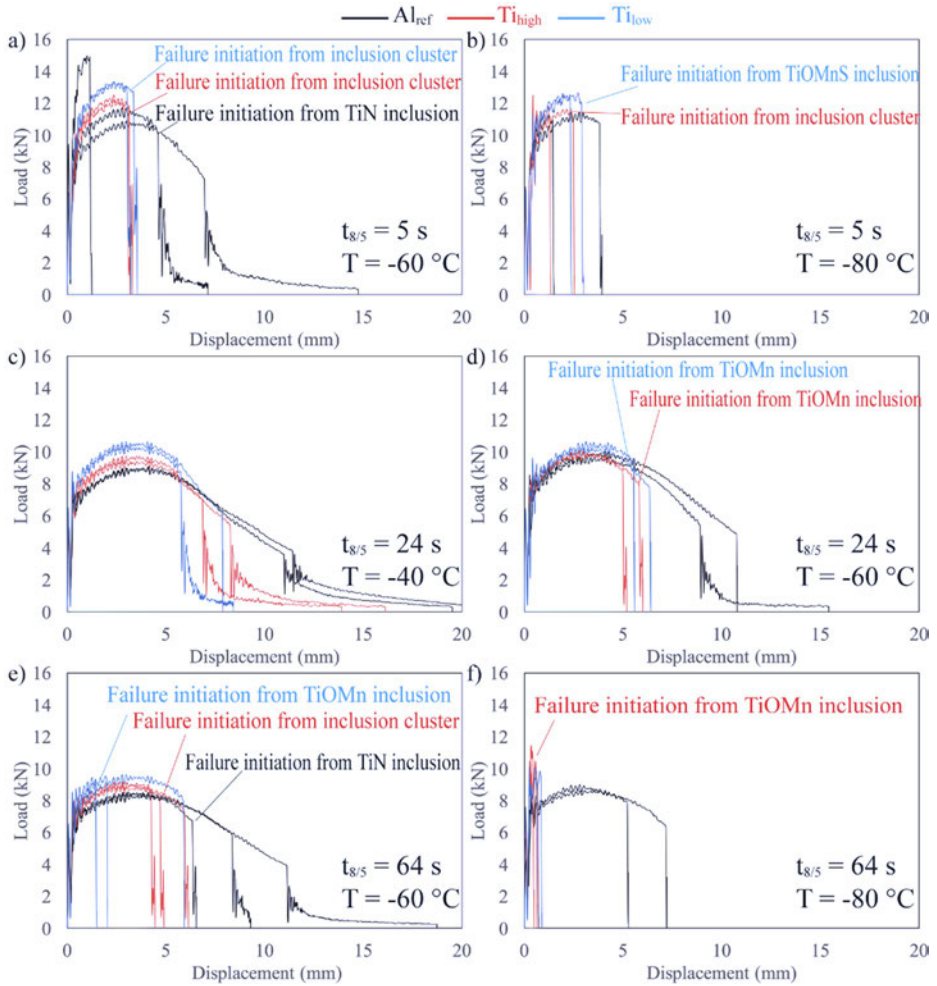


Fig. 30. Load-displacement curves acquired from the instrumented CVN impact toughness tests. CGHAZ simulated $t_{8/5} = 5$ s tested at -60 °C (a) and -80 °C (b); $t_{8/5} = 24$ s tested at -40 °C (c) and -60 °C (d); $t_{8/5} = 64$ s tested at -60 °C (e) and -80 °C (f) (Adapted under CC BY 4.0 license from Publication IV © 2021 Authors).

More detailed data of the samples tested at -60 °C is presented in Table 8. The absorbed impact energy can be divided into crack initiation (E_i) that comprises from the start to F_m , crack propagation (E_p) from F_m until the beginning of brittle crack propagation, and crack arrest ability (E_a) from crack arrest to complete fracture. The values of E_i were in a somewhat similar range in all variants, except in the case of Ti_{low} with $t_{8/5} = 64$ seconds, where E_i values were notably lower. More differences

occurred in respect of E_p , which was generally higher than E_i in Al_{ref}, but lower than E_i in both Ti-deoxidized steels. E_a values were very low and only observed in Al_{ref}.

Table 8. Instrumented CVN impact toughness data of the samples tested at -60 °C. E_i , E_p , E_a = energy absorbed in the crack initiation, crack propagation, crack arrest, respectively (sub-size specimens, $5 \times 10 \times 55 \text{ mm}^3$, absolute values) (Adapted under CC BY 4.0 license from Publication IV © 2021 Authors).

$t_{8/5}$ [s]	Al _{ref}			Ti _{high}			Ti _{low}		
	E_i [J]	E_p [J]	E_a [J]	E_i [J]	E_p [J]	E_a [J]	E_i [J]	E_p [J]	E_a [J]
5	29	19	4	26	7	0	37	10	1
5	13	0	0	26	9	0	29	6	1
5	32	34	8	25	9	1	26	13	1
24	37	52	0	28	17	0	33	19	0
24	33	40	5	29	24	0	33	25	0
64	25	24	0	24	15	0	11	0	0
64	30	46	4	27	21	0	16	0	0
64	30	33	1	23	14	0	14	0	0
64	29	43	4	29	6	0	28	22	0

The variation of average hardness as a function of $t_{8/5}$ measured from the simulated CGHAZ of each variant is presented in Fig. 31. Besides the CGHAZ simulated with $t_{8/5} = 5$ seconds, 24 seconds, 17 seconds and 64 seconds, hardness data obtained on different variants quenched directly in water from the T_p ($t_{8/5} \approx 2-3$ seconds) are also included in the graph for reference purposes. From the graph, it is clear that the hardness decreased in all steels when cooling time increased. Additionally, the hardness of the simulated CGHAZ was highest in Ti_{low} and lowest in Al_{ref} over all cooling times.

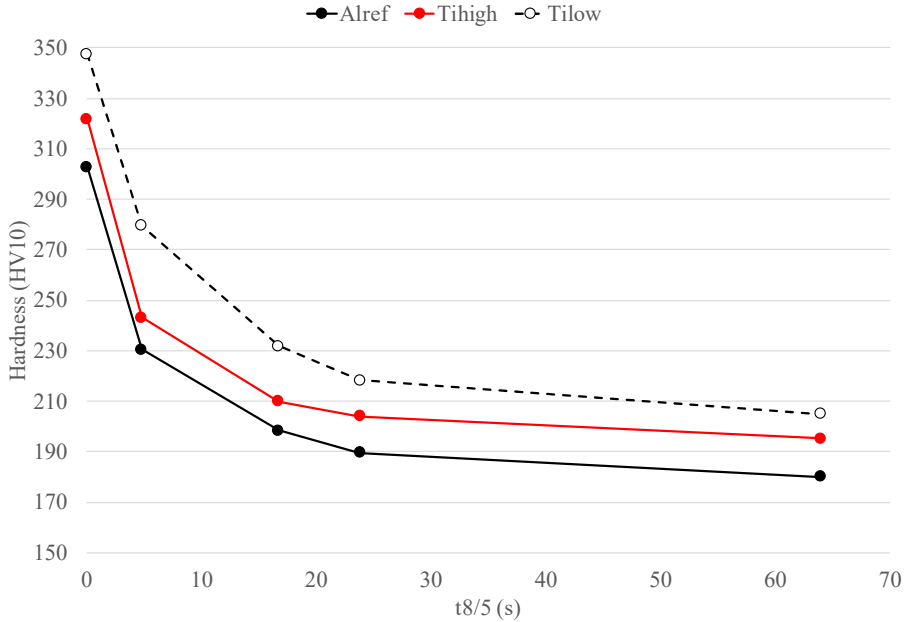


Fig. 31. Average hardness measured from the simulated CGHAZs of the studied steels with cooling times of $t_{8/5} \approx 2\text{--}3$ s (water quenched), 5s, 17s, 24s and 64s (Adapted under CC BY 4.0 license from Publication IV © 2021 Authors).

4.3.2 Inclusions

In Publication III, inclusions were detected and measured only from the samples of the simulated CGHAZs using the intermediate cooling time of $t_{8/5} = 17$ seconds, since it was expected that the cooling time would not significantly change the inclusion content. The size distributions of inclusions according to their number densities and area fractions are presented in Fig. 32. In the Al_{ref} steel, the highest number density of inclusions was in the smallest class, 1–2 μm , while in both Ti_{high} and Ti_{low} steels, there were more inclusions in classes 2–3 μm and 3–5 μm . This size distribution is similar to that of area fractions of inclusions, which was significantly higher in the Ti-deoxidized steels compared to the Al-deoxidized Al_{ref} steel. Additionally, Ti_{high} had more inclusions in the coarsest classes >5 μm than Ti_{low} , as clearly revealed in the chart of area fraction distribution. The differences between the steels stem from the total oxygen contents, which were 23, 47 and 80 ppm in Al_{ref} , Ti_{low} and Ti_{high} , respectively.

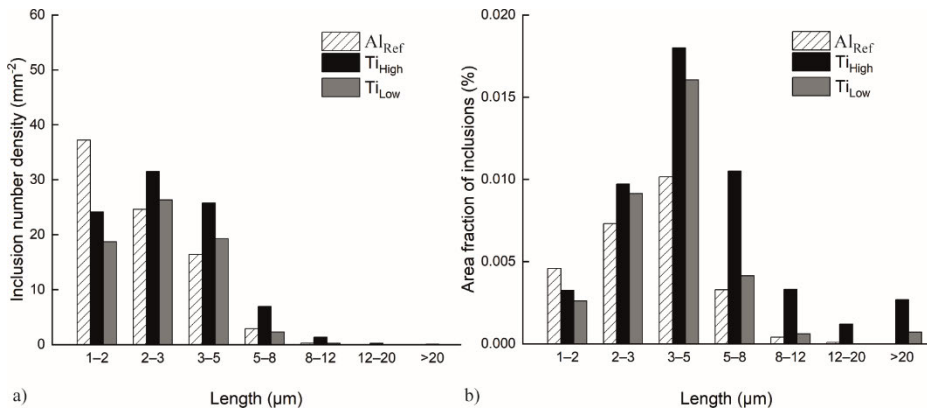


Fig. 32. Number density (a) and area fraction (b) of inclusions according to their size distribution, measured in simulated CGHAZ samples with $t_{8/5} = 17$ s. The inclusions were scanned from an area approximately 37 mm² (Adapted under CC BY 4.0 license from Publication III © 2020 Authors).

The differences in the chemical compositions of the inclusions in the studied steels are depicted in Fig. 33. In the Al-deoxidized Al_{ref} steel, the majority of inclusions contain Al₂O₃-based components, while in Ti-deoxidized Ti_{high} and Ti_{low} steels, Al₂O₃ was replaced by TiO_x-based components and the most common inclusion types were MnO-TiO_x with or without MnS and TiN components. Pure TiN was detected considerably only in Al_{ref} and Ti_{high}, whereas in Ti_{low} there was only a small number of pure TiN inclusions.

Fig. 33 also shows the number density of inclusions smaller than 3 μm separately from all inclusions. This is because small inclusions were considered to have a key role in AF formation. Coarser inclusions may have a more negative effect on toughness and ductility, rather than improving them through the initiation of AF formation. MnO-TiO_x-MnS (with or without TiN), which are reasonably expected to have a beneficial effect on the AF formation, comprised about 1/3 of the small inclusions (<3 μm) in Ti_{low}. On the other hand, in Ti_{high}, the most common small inclusion type was MnO-TiO_x (with or without TiN), while in Al_{ref}, approximately half of the small inclusions consisted of Al₂O₃-containing complex inclusions.

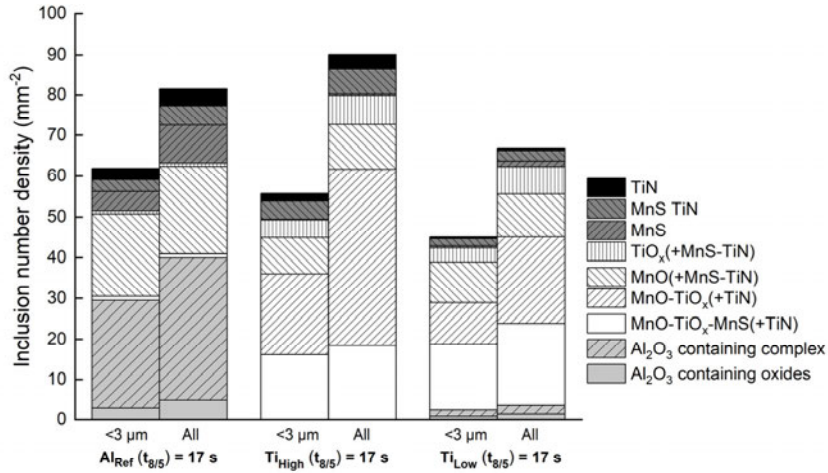


Fig. 33. Number density of inclusions smaller than 3 μm and all inclusions according to their compositional classification in the studied steels. TiO_x represents various titanium oxide phases such as TiO₂ and Ti₂O₃. The inclusions were scanned from an area approximately 37 mm² (Adapted under CC BY 4.0 license from Publication III © 2020 Authors).

In Publication III, inclusions were measured only from simulated CGHAZs of each steel with $t_{8/5} = 17$ seconds to represent all variants (Fig. 32 and Fig. 33), whereas for Publication IV inclusions were measured from variants with $t_{8/5} = 5$ seconds, 24 seconds and 64 seconds and the results are shown in Fig. 34. In this case, alongside all inclusions, coarse inclusions larger than 3 μm were presented separately, since these were assumed to have a negative effect on impact toughness. However, no significant differences were observed between different cooling times. This was expected since inclusions had already formed during the manufacturing process of the steels and the time spent at high temperature during the CGHAZ simulation was too short to cause any changes in the inclusion content. Consequently, the results were similar to those obtained from simulated CGHAZs with $t_{8/5} = 17$ seconds, as has already been presented in Fig. 33.

When it comes to detrimental coarse inclusions, their number densities and especially area fractions were remarkably higher in Ti_{high} compared to Ti_{low} and Al_{ref}. The lowest number density and area fraction of coarse inclusions were detected in Al_{ref} steel. Generally, the most common compositional types of coarse

inclusions were those that were the most common in the case of all inclusions too, i.e., Al_2O_3 containing complex inclusions and $\text{MnO}(+\text{MnS-TiN})$ in Al_{ref} , $\text{MnO-TiO}_x(+\text{TiN})$ in Ti_{high} , and $\text{MnO-TiO}_x(+\text{TiN})$ and $\text{MnO-TiO}_x\text{-MnS}(+\text{TiN})$ in Ti_{low} . Coarse TiN inclusions, which are known to be extremely harmful to the toughness, were present in Al_{ref} and Ti_{high} .

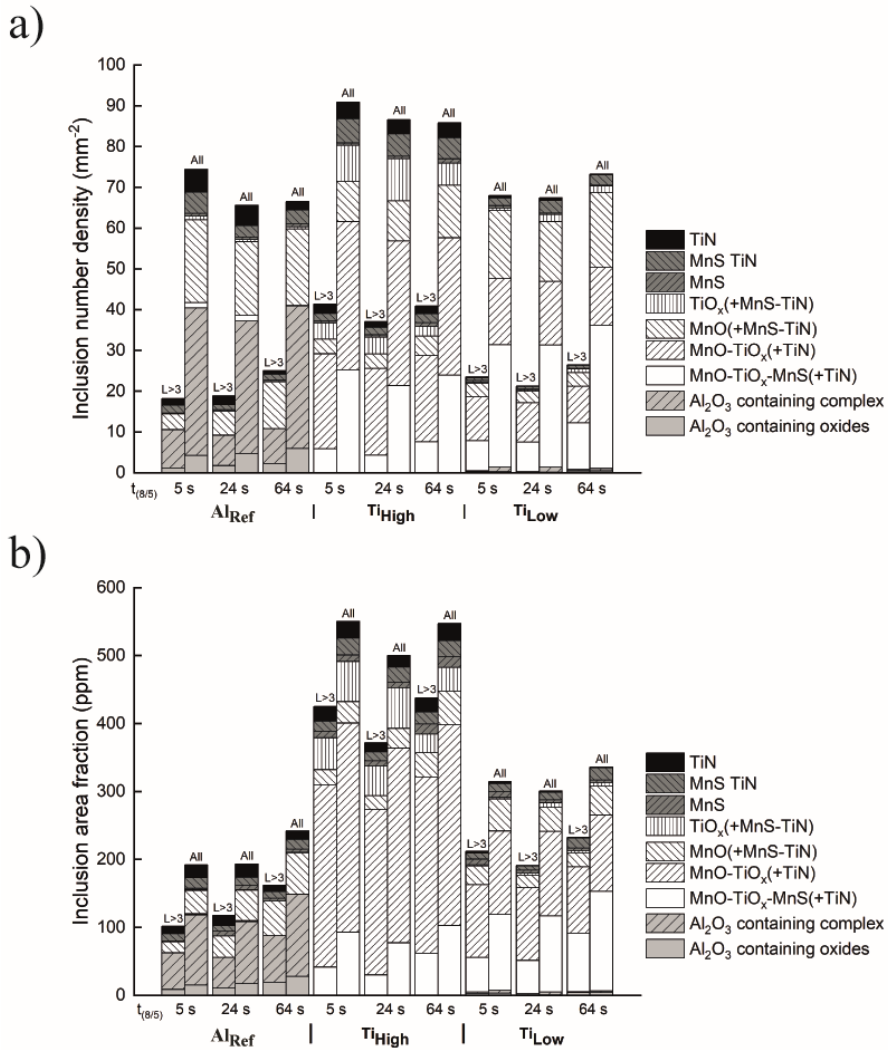


Fig. 34. Number density (a) and area fraction (b) of coarse inclusions ($>3 \mu\text{m}$) and all inclusions in the studied steels. The inclusions were scanned from an area approximately $31\text{--}38 \text{ mm}^2$ in case of $t_{8/5} = 5 \text{ s}$ and 24 s , and from an area approximately $5\text{--}6 \text{ mm}^2$ in case of $t_{8/5} = 64 \text{ s}$ (Adapted under CC BY 4.0 license from Publication IV © 2021 Authors).

5 Discussion

In this chapter, the results of Publications I–IV are discussed with a focus on the role of inclusions on the realized mechanical properties. Primarily, the detrimental effects of different inclusion types on ductility and toughness are discussed, but the beneficial effects of certain inclusion types are also covered, especially in respect of the induced formation of acicular ferrite.

5.1 Effect of impurity level and inclusions on ductility of ultra-high-strength steels

Typical inclusions of Al-killed, Ca-treated, low-alloyed, martensitic ultra-high-strength steels were investigated in Publication I, thus focusing on their influence on ductility and low temperature impact toughness. As can be seen in Table 2, UHSS B displayed significantly better upper shelf energy in the CVN impact toughness tests compared to UHSS A and this was also achieved at lower temperatures in UHSS B than in UHSS A. Additionally, the tensile test results showed that the reduction of area dropped to 54.1% in UHSS A, when tested in transverse to the rolling direction, as against 63.8% achieved in the longitudinal direction. In comparison, UHSS B had a better reduction of area in both the directions compared to UHSS A, i.e., 63.9% and 65.3% in transverse and longitudinal directions, respectively. Besides, the low temperature toughness, defined in this study as absorbed CVN impact energy at $-40\text{ }^{\circ}\text{C}$, was slightly better in UHSS B than in UHSS A. Hence, the aim was to investigate the reasons for these differences in toughness and ductility.

5.1.1 Effect of microstructure on toughness and ductility

Different microstructural features are known to affect the mechanical properties differently in steels. In martensitic and bainitic steels, the impact toughness has been found to improve by: decreasing the prior austenite grain size (PAGS) [66]–[69]; decreasing the average effective grain size, i.e., the packet or block size [70]–[72]; and decreasing the size of the coarsest grains, i.e., $D_{90\%}$ grain size [67], [73]. Regarding the ductility of martensitic steels, there has not been any systematic studies on the effect of different microstructural features. However, the effects of these factors were so small between UHSS A and UHSS B that the differences in toughness and ductility were considered negligible.

5.1.2 Effect of inclusions and impurity content on toughness and ductility

While the microstructural features were similar in UHSS A and UHSS B, differences were quite obvious in respect of impurity and inclusion contents. The impurity level (IL), defined as the sum of %O, %S and %N in wt.%, was 91 ppm in UHSS A as compared to 55 ppm in UHSS B. This was also reflected in the inclusion contents, as can be seen in Fig. 7, as the number densities of coarse ($>8 \mu\text{m}$) inclusions were 1.2 mm^{-2} in UHSS A and 0.7 mm^{-2} in UHSS B. Additionally, the compositional types of the coarse inclusions were different in the two steels; the majority of them were TiN and MnS in UHSS A, and Ca-modified inclusions in UHSS B.

Fig. 35 presents the transverse reduction of area (RA) and transverse upper shelf energy (USE) as a function of impurity level and number density of coarse inclusions. Both RA and USE can be considered a measure of ductility. It was observed that the transverse RA decreased from 63.9% to 54.1%, while the transverse USE decreased from 161 J to 101 J, with increasing impurity level and number density of inclusions. Additionally, the scattering in the RA values was seen to increase from 1.8% in UHSS B to 2.8% in UHSS A, indicating the unpredictable effect of inclusions on the test results. It is to be noted that a similar correlation was not observed in the longitudinal direction. This in-plane anisotropy of ductility in UHSS A was presumably the result of the presence of elongated MnS inclusions, which are especially known to deteriorate the transverse ductility [35], [40], [41], [60], [74], [75].

For instance, in a study of steels with comparable strength levels to the ones investigated here, the transverse reduction of area was measured 51.0%, while the longitudinal one was 63.0%, when the sulphur content was 0.007% and no Ca-treatment was performed. With higher sulphur contents, the transverse reduction of area decreased significantly from that regardless of Ca-treatment [40]. In the present study, the anisotropy of ductility in UHSS A was in similar range, even if the sulphur content was only 0.0018%. Additionally, the study of Ghosh *et. al* [41] showed that the sulphur content as high as 0.01% did not cause anisotropy of ductility when the yield strength of the studied steel was only $\approx 600 \text{ MPa}$. This shows the importance of extra-low sulphur contents in ultra-high-strength steels in order to avoid anisotropy problems.

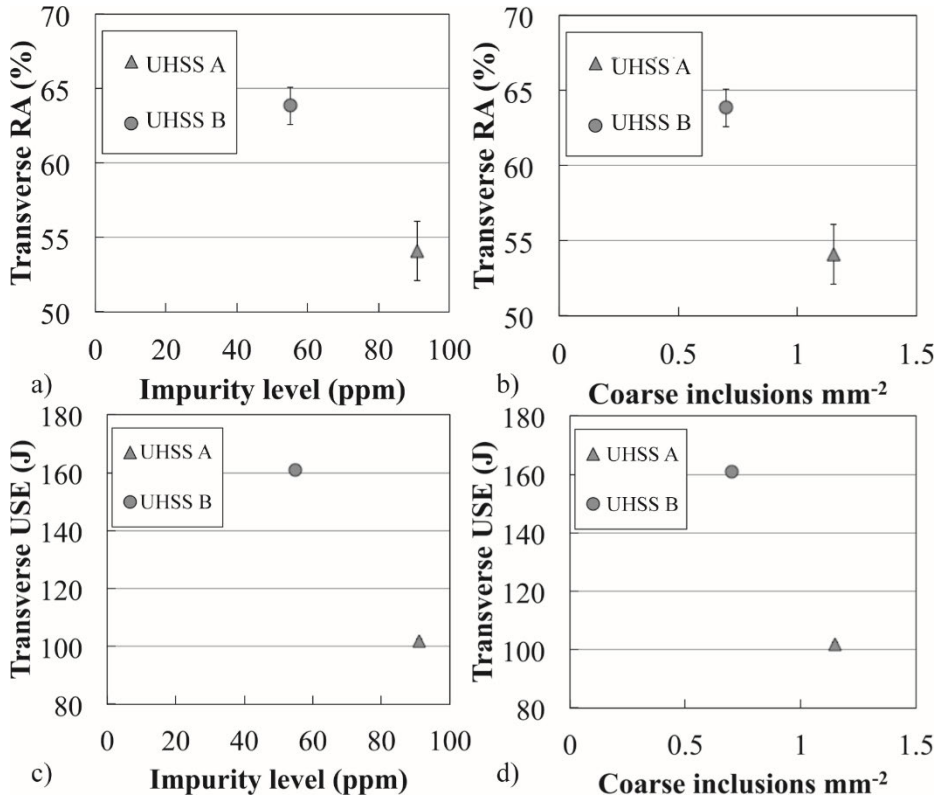


Fig. 35. Effect of impurity level and number density of coarse inclusions ($>8 \mu\text{m}$) on transverse reduction of area (a, b) and on transverse upper shelf CVN impact toughness energy (c, d), respectively. The inclusions were scanned from an area approximately 40 mm^2 (Adapted, with permission, from Publication I © 2017 Elsevier B.V.).

Fractography studies of the tensile tested specimens confirmed the role of elongated MnS causing the lower ductility in UHSS A compared to UHSS B, as presented in Fig. 36. The fractographic features of UHSS A already differed from UHSS B in a macroscale. In UHSS A, the fracture surface was elongated in the rolling direction and looked like a canyon, while in UHSS B, it appeared circular. Zooming in at the fracture surface in LSCM revealed elongated dimples, which were most likely initiated around elongated inclusions. At the bottom of these dimples, fragments of inclusions were found and identified as MnS using FESEM-EDS. In UHSS B, the fracture appeared to have initiated as circular dimples around spherical $x\text{CaO}-y\text{Al}_2\text{O}_3$ inclusions that were found at the bottom of these dimples.

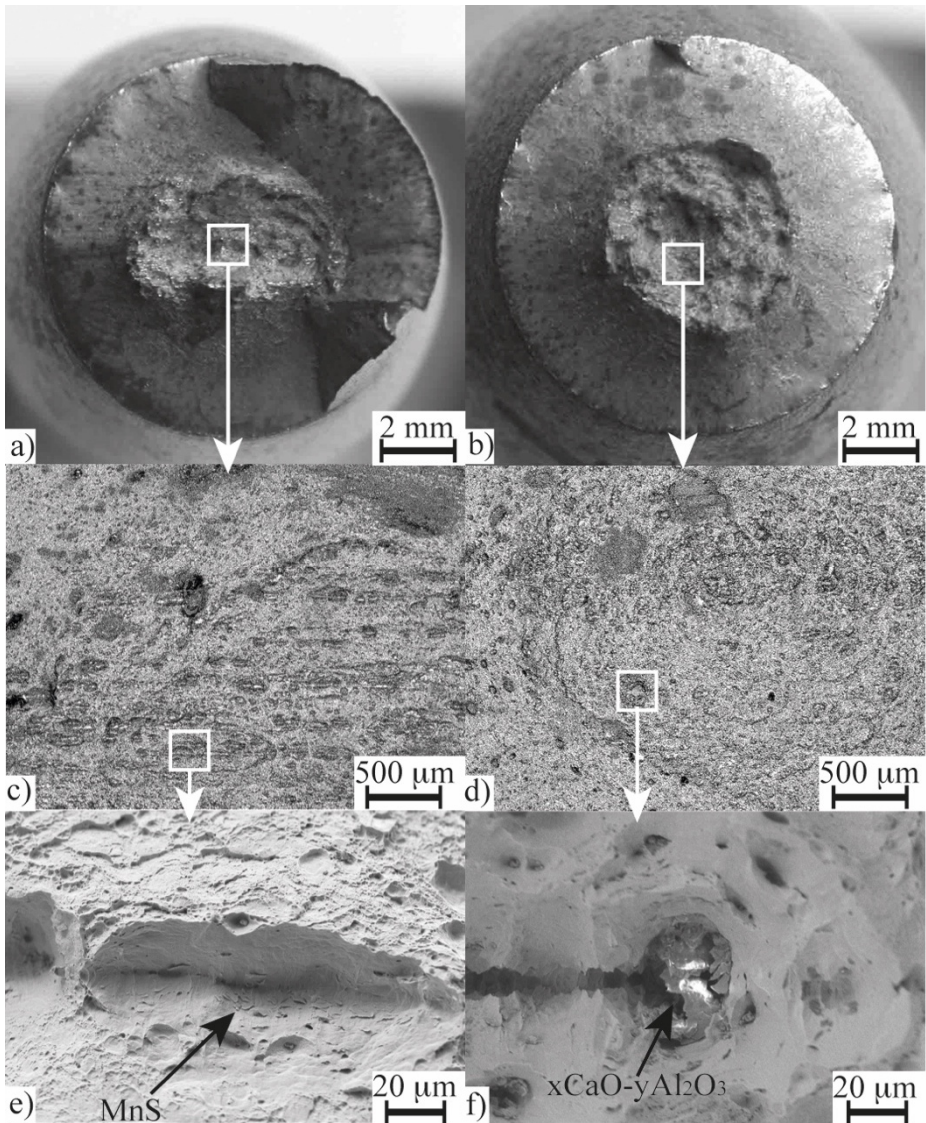


Fig. 36. Macroscale fracture surface of UHSS A (a) and UHSS B (b). LSCM image of the fracture surface of UHSS A (c) and UHSS B (d). FESEM images recorded at the bottom of the fracture surfaces of UHSS A (e) and UHSS B (f) (Reprinted, with permission, from Publication I © 2017 Elsevier B.V.).

As regards low temperature impact toughness, coarse TiN inclusions are known to adversely deteriorate the toughness in ferritic [23], bainitic [21] and martensitic

steels [76], [77]. TiN inclusions have a tendency to initiate cleavage fractures due to the strong bonding between the inclusions and the steel matrix as well as the brittleness of these inclusions [23]. Consequently, stresses from the matrix cause the TiN particle to crack up and thereafter the fracture continues freely into the matrix [24]. This mechanism has been reported to be similar both for bainitic and martensitic steels [78]. In this study, the number densities of coarse ($>8 \mu\text{m}$) TiN inclusions were 0.4 mm^{-2} in UHSS A and 0.1 mm^{-2} in UHSS B. The absorbed impact energy at $-40 \text{ }^\circ\text{C}$ was slightly better in UHSS B, even though there was considerable scattering in the results. It was concluded that the lower impact toughness at $-40 \text{ }^\circ\text{C}$ in UHSS A was probably a result of the higher number density of coarse TiN inclusions compared to that of UHSS B.

5.2 Effect of inclusions on toughness and ductility of the CGHAZ of 500 MPa offshore steels

Publication II dealt with the detrimental effect of inclusions, especially TiN, on the toughness of the coarse-grained heat-affected zone (CGHAZ) in 500 MPa offshore steels. The evaluation was carried out both in respect of impact as well as fracture toughness. Besides, the ductility of simulated CGHAZ was also considered. Steels are known to be more prone to the impairing effect of inclusions on the toughness, as the strength increases [6]. Therefore, despite different inclusion contents in the studied steels, the base material properties (Table 3) were observed to have not been affected by the inclusions, even if some differences in the inclusion contents might have caused differences in the toughness of steels with higher strengths. However, the CGHAZ is an altogether different topic due to the changes in the microstructure caused by the thermal cycles during welding. One of the main phenomena in the CGHAZ is the coarsening of prior austenite grain size (PAGS), leading to the increased vulnerability of the microstructure to the detrimental effect of hard and brittle inclusions, such as coarse TiN. This turns out to be a result of the mechanism leading to the fracture propagating freely from the cracked inclusion through the whole grain before meeting the obstacles, such as grain boundaries [23], [24]. Additionally, the transformed microstructure of the CGHAZ may consist of a combination of several types of microstructural phase constituents, depending on the heat input of the welding and the subsequent cooling rate, with each microstructure type having different properties.

As presented in Fig. 14 and Fig. 15, the studied steels had differences in respect of both the impact toughness as well as fracture toughness. Steels A1 and B1 had

better impact toughness properties compared to A2 and B2 when cooling time $t_{8/5} = 6$ seconds was applied to the simulated CGHAZ. When the applied cooling time was $t_{8/5} = 30$ seconds, the impact toughness was better in A1 and A2 compared to B1 and B2. The best fracture toughness performance was generally observed in A1, while A2 showed mostly good results with $t_{8/5} = 30$ seconds. B1 still had moderately good fracture toughness at -10 °C but not at -40 °C.

The essential difference between A1 and A2, as well as B1 and B2, was in respect of inclusion contents. The compositional differences existed only between steels A and B. As presented in Fig. 16, Fig. 17 and Fig. 18, the number density of inclusions was highest in A1, and in general, A1 and B1 contained more inclusions compared to A2 and B2, respectively. TiN inclusions were absent in A1, and the highest number of these inclusions were detected in A2. Especially, these inclusions were found to have concentrated at certain depths of the plate thickness, i.e., along segregation bands. B2 also had slightly more TiN inclusions than B1.

The statistical sampling effect is expected to affect the toughness results, when the spatial distribution of TiN is inhomogeneous, as was observed particularly in A2, but in some extend also in B1. According to the literature [46], low CTOD values are expected, when the fatigue precrack of the test specimen samples a high number density region of coarse TiN particles. Unfortunately, in the current study the sampling regarding the different regions of TiN particle number density was not recorded. However, the considerable scatter in the toughness properties may result from this effect.

Fig. 37 presents the effect of TiN inclusions on the impact toughness transition temperature (a) as well as the effect of all inclusions together on impact toughness upper shelf energy (USE) (b). It is to be noted the transition temperature increases with the increase in number density of TiN inclusions. In other words, the ductile to brittle transition occurs already at less harsh temperatures, when there are more TiN inclusions in the steels. USE, on the other hand, is a measure of ductility. Ductile fracture starts with the nucleation and coalescence of the microvoids around inclusions. Therefore, when there are more inclusions in the steel, there is a probability of increased microvoid formation in the steel, thus rendering the material less ductile. Both the effect of TiN on transition temperature as well as the effect of all inclusions collectively on USE were more significant, when the shorter cooling time of $t_{8/5} = 6$ seconds was applied to the simulated CGHAZ. On the other hand, the transition temperatures were lowest when the cooling time $t_{8/5} = 6$ seconds instead of $t_{8/5} = 30$ seconds was applied, and when the number densities of TiN inclusions were lowest in the steel. This is due to the differences in the

transformation microstructures caused by the different cooling rates. The effective grain size as well as the size of the coarsest grains increase with increasing cooling time as was seen also in this study in Fig. 13. Therefore, there are less obstacles to stop the propagation of the fracture in variants simulated with $t_{8/5} = 30$ seconds compared to $t_{8/5} = 6$ seconds.

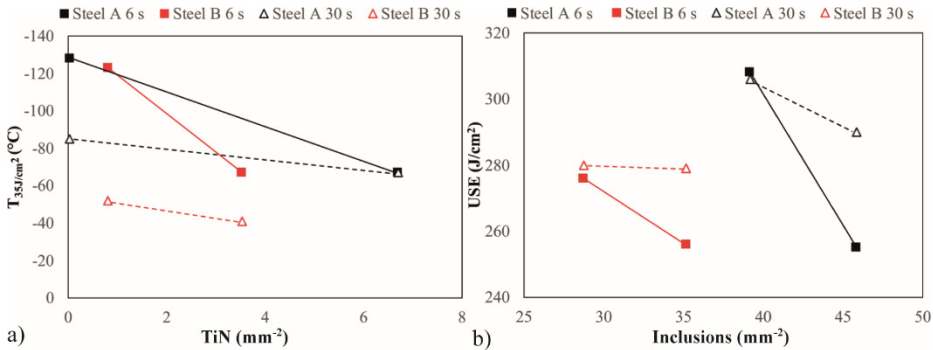


Fig. 37. Effect of number density of TiN inclusions on transition temperature T_{35} of the simulated CGHAZs (a) and the effect of number density of all inclusions on the upper shelf energy of the simulated CGHAZs (b). Transition temperature values below -80 °C are predicted since that was the lowest testing temperature. The inclusions were scanned from an area approximately 36 mm^2 (Reprinted, with permission, from Publication II © 2019 Elsevier B.V.).

As seen previously in Fig. 15, TiN inclusions were identified as the initiators of the early failures in the case of A2 with both cooling times, as well as for B1 and B2 with the cooling time of $t_{8/5} = 30$ seconds. Fig. 38 presents such TiN inclusion in A2 with $t_{8/5} = 30$ seconds. EDS analysis shows that there is also a small fraction of Nb in the inclusion besides Ti and N.

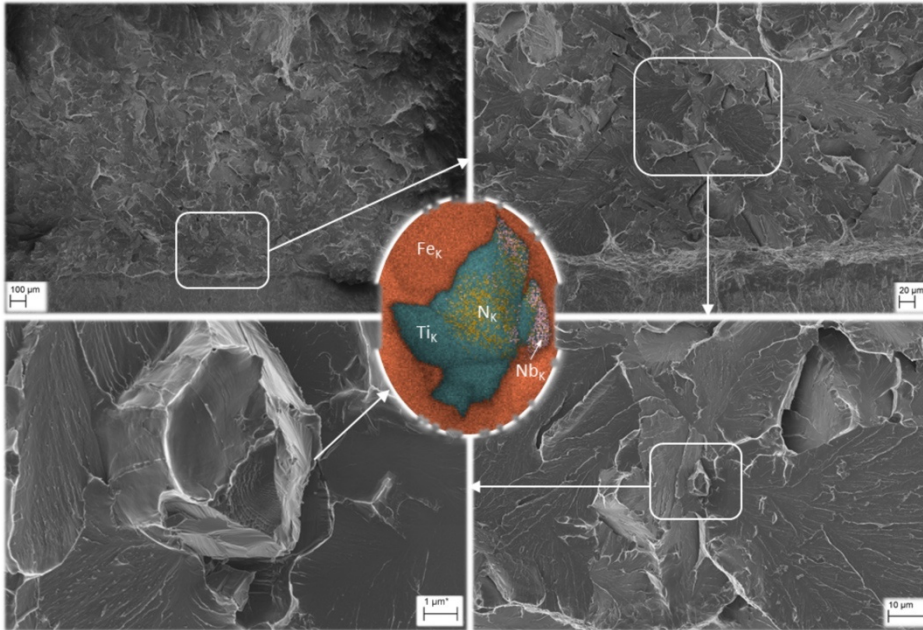


Fig. 38. Initiation of a brittle fracture in Steel A2 ($t_{8/5} = 30$ s) caused by a compact cluster of TiN inclusions (Reprinted, with permission, from Publication II © 2019 Elsevier B.V.).

To clarify the findings of the study with various factors affecting the impact toughness and fracture toughness results, a summary is presented in Table 9. It is noteworthy that the best combination of both the impact toughness transition temperature as well as the fracture toughness can be seen in Steel A1 with $t_{8/5} = 6$ seconds. The absence of TiN inclusions together with a fine effective grain size ensured the best toughness properties in the steel A1, which also performed relatively well with $t_{8/5} = 30$ seconds, though the fracture toughness results showed considerable scatter. Steel B1 also had good toughness properties with $t_{8/5} = 6$ seconds. However, already as low number density of TiN inclusions as 0.8 mm^{-2} , together with coarsened grains due to the longer cooling time of $t_{8/5} = 30$ seconds, led to a remarkable decrease in transition temperature. This indicates that a strict control of TiN is needed, especially if applying higher heat inputs in welding.

Table 9. Summary of the key material performance measures and the resulting toughness values. Microstructural characterization was performed on A/B1 variants only since the difference compared to A/B2 was assumed to be negligible. Microstructural abbreviations: upper bainite (UB), granular bainite (GB), martensite (M), lower bainite (LB). The inclusions were scanned from an area approximately 36 mm² (Adapted, with permission, from Publication II © 2019 Elsevier B.V.).

Steel	$t_{8/5}$ [s]	Microstructure	Hardness [HV ₁₀]	D_{eff} [μm] / $D_{80\%}$ [μm]	TiN [pcs/mm ²]	Failure initiator	T_{35} [°C]	$K_{Jc(1T)}$ @ -40 °C [MPa√m]
A1	6	UB-GB	235–239	3.5/40.9	0	Undefined	<-100	215±8
A1	30	GB-UB	202–214	5.7/44.4	0	Undefined	-85	193±80
A2	6	6.7	TiN	-67	119±29
A2	30	6.7	TiN	-67	177±118
B1	6	M-LB-UB	274–280	2.1/8.7	0.8	UB*	<-100	126±16
B1	30	GB-UB	208–210	3.3/33.5	0.8	TiN	-52	107±23
B2	6	3.5	TiN	-77	71±23
B2	30	3.5	TiN	-41	10±24

*potentially coarse carbides in upper bainite (UB)

5.3 Factors affecting the impact toughness of the CGHAZ of 420 MPa offshore steels

This section discusses the results presented in both Publication III and Publication IV, as these were from the same study. The aim was to improve the impact toughness of the CGHAZ in 420 MPa offshore steels. Firstly, based on the literature, it was assumed that the presence of acicular ferrite in the CGHAZ microstructure would improve impact toughness. Therefore, it was decided to study the factors affecting the formation of acicular ferrite. In the second part, the main focus was to understand if the achieved fraction of acicular ferrite actually improved impact toughness. Contrary to the expectations, the acicular ferrite formation, however, did not show any improvement of the impact toughness of CGHAZ in this study, and the concerned results are presented in Fig. 29 and Fig. 30. Finally, investigations were carried out to find the explanations for these unexpected results. When it comes to the inclusions, their role on the impact toughness was considered keeping in view both the positive as well as negative effects. The results can be called positive because certain types of inclusions are known to promote the formation of acicular ferrite, and negative because of their role in initiating cleavage fractures.

5.3.1 Role of titanium oxides in inducing acicular ferrite formation

Titanium oxides, such as TiO_2 and Ti_2O_3 , have been reported to be some of the most promising inclusion types to promote the formation of acicular ferrite [14], [15]. Titanium oxides form in the steel as a result of the deoxidizing process, when titanium is used as a reagent instead of the more commonly used aluminium or silicon. Therefore, Ti-deoxidized experimental steels were trialled in order to include titanium oxides in the steels. However, regarding the acicular ferrite formation, inclusion size also matters. It has been reported that the optimal size for titanium oxides would be approximately 0.25 to 3.00 μm [14], [15], [49]. Additionally, it would be beneficial to have manganese in the inclusions, either as a compound together with titanium oxide, e.g., TiO-MnO , or as separate manganese sulphide phase on the surface of the titanium oxide. This is due to the diffusion of manganese from the steel matrix into the inclusion, resulting in a local depletion of manganese in the matrix next to the inclusion. The transformation temperature of ferrite increases locally because of this depletion of manganese, which in turn encourages ferrite to nucleate around inclusions within the grains instead of nucleating on grain boundaries [50]–[52], [79]–[83].

As construed previously in Fig. 33, the most promising inclusion type, $\text{MnO-TiO}_x\text{MnS(+TiN)}$, made up approximately 1/3 of all inclusions smaller than 3 μm in Ti_{low} . It is also notable that the majority of this type of inclusions in Ti_{low} was smaller than 3 μm . In Ti_{high} , the most dominant inclusion type was $\text{MnO-TiO}_x(+\text{TiN})$, which may also promote the nucleation of acicular ferrite. However, a notable fraction of this type of inclusions in Ti_{high} was coarser than 3 μm , which might not be optimal for acicular ferrite formation. Instead, these might impair the impact toughness as cleavage fracture initiators.

The depletion of manganese near the inclusions was studied by TEM-EDS. Fig. 39 presents a typical $\text{MnO-TiO}_x\text{-MnS(+TiN)}$ inclusion of Ti_{low} that was chosen for the TEM-EDS observation. The upper edge of the inclusion is the polished surface of the metallographic specimen. The manganese content was measured starting from the interface of the inclusion and matrix extending over 250 nm into the matrix. A statistical analysis of the measurements showed that the depletion of manganese occurred 37 nm from the inclusion-matrix interface and into the matrix. The measured manganese content was also slightly higher than the nominal 1.7 wt.%. Some possible reasons for this are segregation of manganese in the analysed region, differences in the measurement methods (the nominal 1.7 wt.% was obtained by optical emission spectroscopy (OES)), elimination of some elements

from the analysis before the normalisation of the results, or not calibrated measurements.

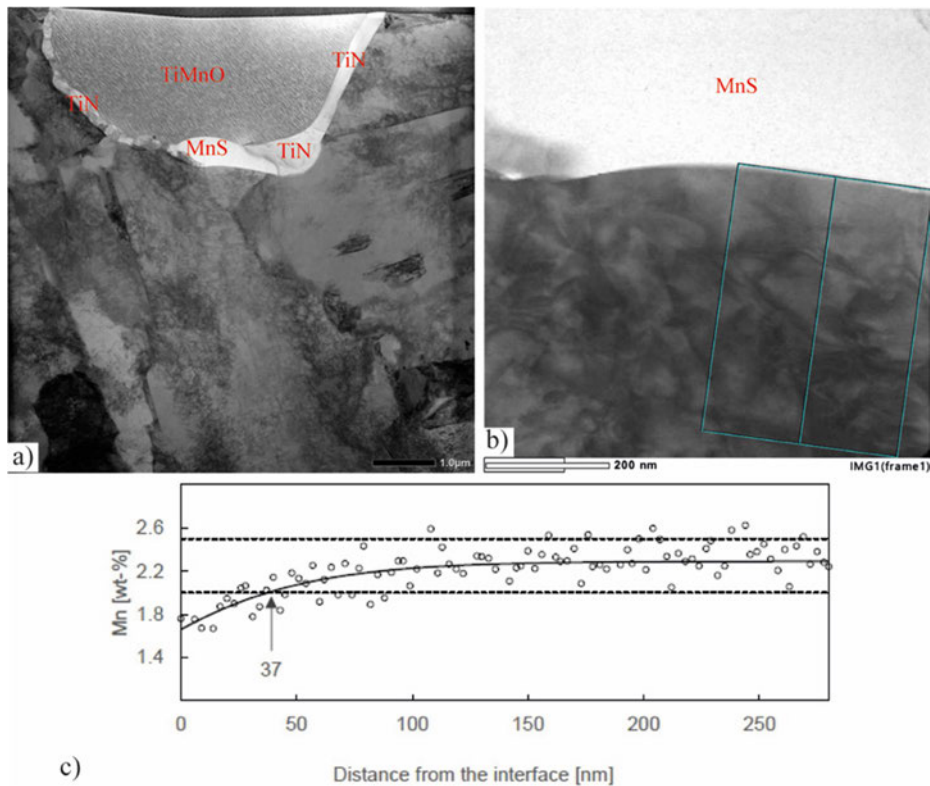


Fig. 39. TEM image of a typical inclusion the simulated CGHAZ of Ti_{low} with $t_{8/5} = 24$ s (a); closer look at the area where the Mn content was measured (b). The measured Mn content where dotted lines represent standard deviations from the mean taken from data points >200 nm from the MnS-matrix interface (c) (Reprinted under CC BY 4.0 license from Publication III © 2020 Authors).

The depletion of Mn content was also simulated using the DICTRA module in Thermo-Calc software [84]. It was assumed that the MnS had already precipitated on the surface of an inclusion and the growth of these MnS precipitates occurred through the diffusion of Mn from the steel matrix. The simulation supported the observation made by TEM-EDS analysis, showing the decrease in the Mn-content near the MnS-austenite interface, as shown in Fig. 40. The increase in cooling time affected an increase in the width of the depletion zone. This may be one factor

responsible for the increased fraction of acicular ferrite with the increase in cooling time, since the decrease of Mn-content is known to drive ferrite formation [51], [52], [79], [83].

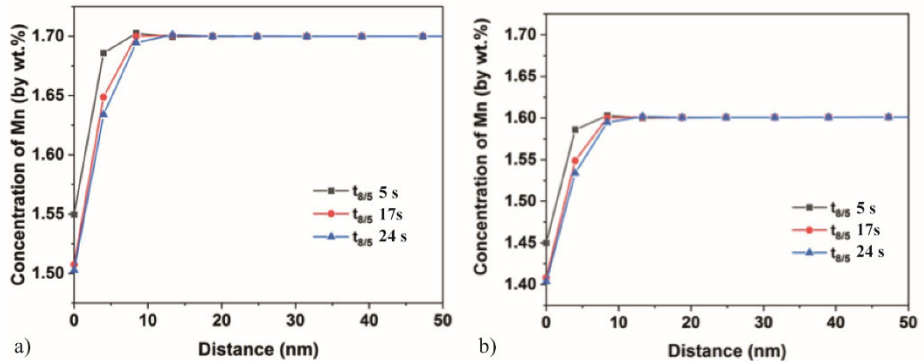


Fig. 40. Computer simulation of variation of Mn concentration from MnS-austenite matrix interface into the austenite matrix for the simulated CGHAZ using the cooling times $t_{9/5} = 5$ s, 17s and 24s, assuming no initial Mn depletion (a), and assuming an initial depletion of Mn to 1.6 wt.% (b) at the MnS-matrix interface (Adapted under CC BY 4.0 license from Publication III © 2020 Authors).

5.3.2 Other factors affecting acicular ferrite formation

The formation of acicular ferrite (AF) in the coarse-grained heat-affected zone (CGHAZ) depends on various simultaneous factors. Beneficial inclusion content is one factor, but it is not enough for producing AF by itself.

Coarse prior austenite grain size (PAGS) is known to promote the formation of intragranular AF by reducing the total grain boundary area [14], [15]. One study [85] suggests that PAGS coarser than 100 μm is needed in order to achieve more than 60% AF in the CGHAZ, and according to another study [47], PAGS as coarse as 250 μm is required to promote AF formation. However, coarse PAGS itself is known to impair toughness. Hence, PAGS should be sufficiently coarse to initiate the AF formation, but within certain limits to prevent a negative effect on the toughness. 150 μm has been suggested as a critical PAGS, beyond which, the positive effect of AF on the toughness starts to diminish [14].

As seen in Fig. 19, the PAGS was remarkably coarser in $T_{i\text{low}}$ compared to $A_{l\text{ref}}$ and $T_{i\text{high}}$. The measured mean PAGS in $T_{i\text{low}}$ was 225 μm , but some grains were far more coarser than the average. Such coarse PAGS had evidently promoted AF

formation in Ti_{low} , but also might have had negative effect on the toughness. However, the mean PAGS of $75\ \mu m$ and $77\ \mu m$ in Al_{ref} and Ti_{high} , respectively, were not coarse enough to support AF formation.

The third important factor, besides inclusions and PAGS, is the cooling rate, $t_{8/5}$. The question of the cooling rate is complicated since it depends on the chemical composition of the steel. However, in low-carbon, Ti-deoxidized steels, the formation of AF has been observed in a wide range of cooling rates, from $t_{8/5} = 5.6$ seconds to $t_{8/5} = 1000$ seconds [86]. In the current study, it was observed that the fraction of AF increased as $t_{8/5}$ increased, as was listed in Table 5. More precisely, in Ti_{low} , the fraction of AF increased from 19% with $t_{8/5} = 5$ seconds to 46% with $t_{8/5} = 64$ seconds. In Al_{ref} and Ti_{high} , a small fraction of AF was observed only with the longest applied cooling time, $t_{8/5} = 64$ seconds. The explanation for this behaviour can be corroborated with the predictions of continuous cooling transformation diagram, where the transformation of AF is expected to occur in a cooling range between bainite and polygonal ferrite [27]. Hence, the increasing cooling time reduces the driving force for bainite formation and promotes AF formation. Additionally, the depletion of manganese near inclusions in the steel matrix may have a small effect, as was discussed in the previous chapter.

5.3.3 Role of coarse inclusions impairing the impact toughness of the coarse-grained heat-affected zone

As discussed previously, certain types of inclusions might be beneficial for the toughness of the steel through enhancement of acicular ferrite formation. Conventionally, inclusions are considered detrimental to the toughness. In coarse-grained heat-affected zones (CGHAZ), typically the most harmful inclusions are coarse titanium nitrides (TiN). As discussed in Section 5.2, this is due to the combined effect of the hard and brittle TiN particles acting as the initiators of cleavage fracture, and the coarsened grains letting the fracture propagate freely over lengthy distances.

As shown in Fig. 34, the number density and area fraction of coarse inclusions was highest in Ti_{high} and lowest in Al_{ref} . Expectedly, such coarse inclusions might cause problems regarding the toughness. On the other hand, the extremely harmful TiN inclusions were present not only in Ti_{high} but also in Al_{ref} .

Fractographies of the CVN impact tested specimens revealed inclusions that likely had a role leading to the final fracture. Fig. 41 shows the fracture surface morphologies and inclusions found near the fracture initiation sites in Al_{ref} , Ti_{high}

and Ti_{low} with $t_{8/5} = 5$ seconds tested at -60 °C. The respective absorbed impact energies recorded in these specimens were 13 J, 33 J and 36 J, respectively. It can be seen that the inclusions found near fracture initiation sites were TiN in Al_{ref} and complex clusters of MnO-TiO_x(+TiN) in Ti_{high} and Ti_{low} . TiN inclusions in Al_{ref} were deeply located in a hole and hence could not be analysed reliably by EDS. However, based on the shape of the inclusions and the presence of TiN in the inclusion measurement, these were identified as TiN. MnO-TiO_x(+TiN) were the most common inclusion types in Ti_{high} and Ti_{low} , so it is logical that these inclusions were found on the fractured surfaces. When present in coarse sizes, these otherwise good promoters of AF are detrimental to the toughness.

TiN inclusions were not frequent in the distribution of inclusions in Al_{ref} . However, their detection in the fractography indicates that these are the most harmful inclusion types in Al_{ref} for impact toughness.

Fig. 41a, c & e also show that the average cleavage facet size is somewhat larger in Ti_{low} compared to Al_{ref} and Ti_{high} , most likely due to the larger PAGS in Ti_{low} than the other two steels. However, despite the larger cleavage facet size, the absorbed impact energy in Ti_{low} is comparable with that of Ti_{high} and even slightly higher than that of Al_{ref} . This indicates the combined effect of the grain size and the hard and brittle inclusions, as substantiated by the literature [24], [87]. The level of more harmful inclusion content diminishes the beneficial effect of finer PAGS, as might have occurred in the case of Ti_{high} compared to Ti_{low} . In Al_{ref} , the PAGS was also relatively fine. However, in this particular specimen, a coincidental TiN inclusion present in the steel might have caused the premature fracture. This result is supported by the fact that other Al_{ref} specimens with the applied shorter cooling time of $t_{8/5} = 5$ seconds and tested at -60 °C had remarkably better impact toughness, as shown in Fig. 30a.

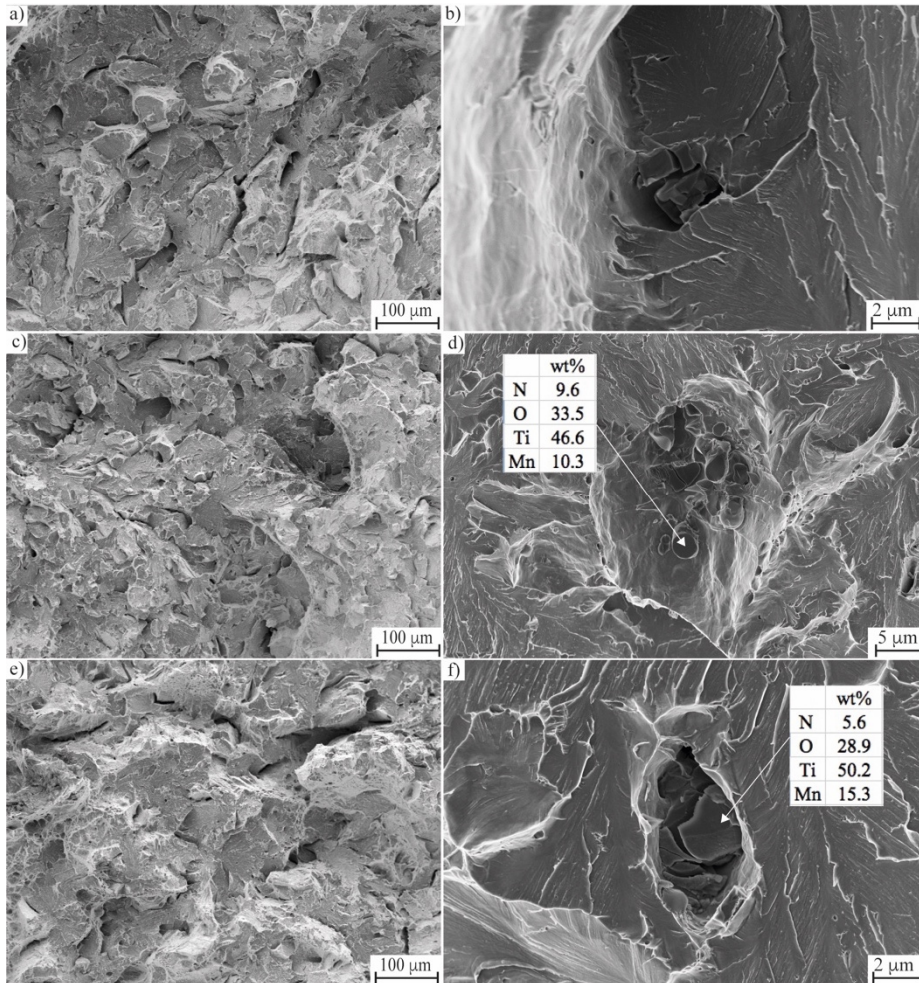


Fig. 41. Fractography of the CVN specimens from approximately the middle of the fractured surface (a, c, e) accompanied by inclusions found from the fracture surfaces (b, d, f) of Al_{ref} (a, b) Ti_{high} (c, d) and Ti_{low} (e, f) (Reprinted under CC BY 4.0 license from Publication IV © 2021 Authors).

5.3.4 Other factors affecting the impact toughness of the coarse-grained heat-affected zone

Naturally, impact toughness depends on many factors having a simultaneous effect, inclusions being only one of these. Both the chemical composition and the

microstructure play a prominent role. Generally, the alloying elements that promote hardenability, such as carbon, silicon and vanadium, tend to decrease the toughness, since any increase in hardness and strength usually leads to a decrease in toughness. Each microstructural component, such as various allotropies of ferrite, bainite and martensite, contribute to the strength/toughness combination of steels in their own way. In addition, the roles of prior austenite grain size, retained austenite, martensite-austenite (M-A) constituents and precipitates should also be considered.

Carbon content was equal (0.05%) in Al_{ref}, Ti_{high} and Ti_{low}, but there were differences in respect of vanadium and silicon contents, which are also known to affect the hardenability of the steels. Vanadium content was 0.07% in Ti_{high} and Ti_{low}, while only 0.01% was present in Al_{ref}. Silicon content was also present in Ti_{low} (0.23%), which was not added in Al_{ref} (0.01%) and Ti_{high} (0.03%). These small differences in the alloying caused slight variation in hardness, as can be seen in Fig. 31. Regardless of the cooling rate, the highest hardness was always measured in Ti_{low} and the lowest in Al_{ref}. Since hardness is related to tensile strength, which in turn is known to affect the toughness, it can be deduced that the difference in hardness might be one factor explaining the differences in the impact toughness of Al_{ref} and Ti-deoxidized steels.

The slight difference in hardenability also caused variation in transformation microstructures, as could be predicted from the continuous cooling transformation diagrams. As summarized in Table 5, the difference in hardenability is seen particularly applicable with the fastest cooling rate ($t_{8/5} = 5$ seconds), where a higher fraction of lath bainite was present in Ti-deoxidized steels (21% in Ti_{high} and 32% in Ti_{low}) compared to Al_{ref} (13%). With slower cooling rates ($t_{8/5} = 24$ seconds and 64 seconds), the microstructures were predominantly plate-like bainite, but in Ti_{low}, the fraction of acicular ferrite (AF) was also notable. Since different types of microstructural components have different fractions of high-angle grain boundaries, there was a variation in grain sizes between the studied steels (Table 6). Generally, a finer grain size is expected to improve the toughness. However, despite the finest median grain size measured in Ti_{low} with $t_{8/5} = 64$ seconds (1.04 μm), it had the lowest impact toughness. Hence, instead of median size, the defining factor might be the size of the coarsest grains. However, the coarse grains in Al_{ref} with $t_{8/5} = 64$ seconds did not prevent this variant having the best impact toughness at -80 °C. This leads to a conclusion that the effective grain size alone did not determine the impact toughness in this study, but this might have had a role in combination with other factors. Particularly, coarse grains are known to cause more vulnerability to fracturing with the presence of coarse inclusions [87]–[89].

Prior austenite grain size (PAGS) was already discussed regarding the formation of AF. However, when the coarsening of PAGS promotes the formation of AF, it also has a negative effect on the toughness [68]. Since the PAGS was significantly coarser in Ti_{low} (225 μm) compared to Al_{ref} (75 μm) and Ti_{high} (77 μm), as can be seen in Fig. 19, it can be expected to have a negative effect on impact toughness. This is also supported by literature since the positive effect of acicular ferrite formation has been suggested to diminish with increasing PAGS e.g. when the PAGS is coarser than 150 μm according to one study [14].

The fractions of retained austenite were also listed in Table 5. It was noted that the Ti-deoxidized steels had a slightly higher fraction of retained austenite compared to Al_{ref}. Additionally, the tendency of retained austenite to increase with the cooling time was noted. However, interestingly, simulated CGHAZ in Al_{ref} with $t_{8/5} = 64$ seconds had the lowest fraction of retained austenite (1.1%) of all variants. The presence of retained austenite indicates to the likely formation of martensite-austenite constituents, which are commonly known to deteriorate the toughness, especially in the CGHAZ [49]. Hence, it can be expected that the higher fraction of retained austenite as M-A constituents in Ti-deoxidized steels compared to Al_{ref} had a role in impairing the impact toughness of Ti_{high} and Ti_{low}.

Nanoscale precipitates, especially TiN, are known to inhibit the grain growth of austenite during welding heat cycles [19], [20]. Since the PAGS was significantly coarser in Ti_{low} compared to Ti_{high} and Al_{ref}, it was expected that the microstructure lacked the presence of nanoscale precipitates. However, the results were not straightforward. Fig. 42 presents TiN precipitates found in all variants and the numerical data of the precipitate study is summarized in Table 10. Ti_{low} had the lowest number of precipitates with $t_{8/5} = 5$ seconds and 24 seconds. However, with $t_{8/5} = 64$ seconds, the lowest number of precipitates was in Al_{ref}. The highest number of precipitates was generally in Ti_{high}, which also had the highest number density of microscale inclusions. This may explain why the PAGS was not as coarse in Ti_{high} as in Ti_{low}. Due to the inconsistencies, partly explained by the investigated area being relatively small, it is not possible to draw reliable conclusions.

TiN with traces of C, Nb and V

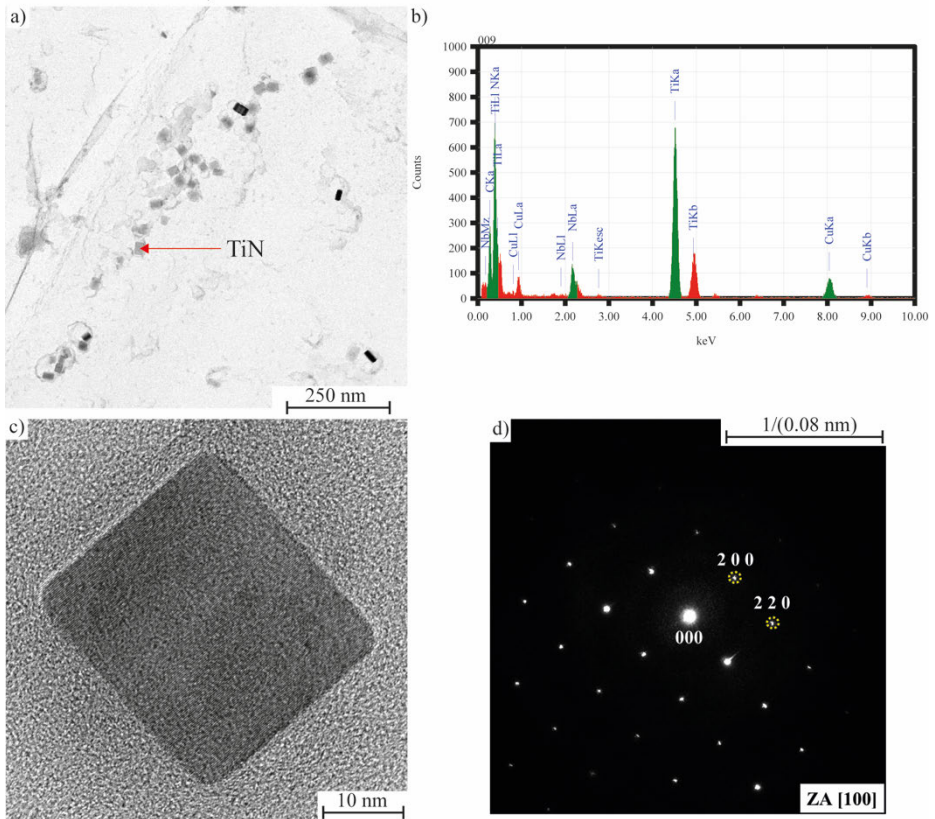


Fig. 42. TiN precipitates observed in the studied steels (a) with energy-dispersive X-ray spectrometry (EDS) analysis (b). A single TiN precipitate (c) with its lattice structure (d) (Reprinted under CC BY 4.0 license from Publication IV © 2021 Authors).

Table 10. Precipitation data of the studied steels acquired by TEM. The total investigated area was 100 μm^2 (Adapted under CC BY 4.0 license from Publication IV © 2021 Authors).

Data type	Al _{ref} 5 s	Ti _{high} 5 s	Ti _{low} 5 s	Al _{ref} 24 s	Ti _{high} 24 s	Ti _{low} 24 s	Al _{ref} 64 s	Ti _{high} 64 s	Ti _{low} 64 s
No. of precipitates	305	709	230	375	340	299	470	603	551
Average ECD [nm]	31	38	35	29	39	39	32	36	32
Confidence level (95%)	2	1	3	1	2	3	2	1	1
$D_{90\%}$ [nm]	62	94	113	50	80	101	94	80	62
Min. ECD [nm]	16	18	20	20	20	17	10	19	16
Max. ECD [nm]	143	160	147	226	138	208	138	189	178

In order to combine different factors affecting the impact toughness of the CGHAZ in the studied offshore steels, multivariate linear regression models were prepared (Table 11). The variable data consisted of the acquired phase fractions, inclusion data and grain sizes. Variables with $p > 0.05$ were excluded from the models. In other words, the models suggest what the defining parameters were for the given properties. Models A and B examine the factors contributing to total absorbed energy in CVN impact toughness testing. In models C, D, and E, the outcomes were the crack initiation, propagation, and arrest, respectively.

Generally, the models suggest a positive effect of plate-like bainite. Coarse inclusions and retained austenite generally had a negative effect on toughness.

Table 11. Regression models on the effect of different factors on impact toughness values of the simulated CGHAZs in the studied steels. The inclusions were scanned from an area approximately 31–38 mm² in case of $t_{8/5} = 5$ s, 17 s and 24 s, and from an area approximately 5–6 mm² in case of $t_{8/5} = 64$ s (Adapted under CC BY 4.0 license from Publication IV © 2021 Authors).

Parameter	Model A	Model B	Model C	Model D	Model E
<i>n</i>	27	52	54	53	54
Constant	23.9	*	**	***	****
Plate-like bainite	1.183	0.802	0.223	0.421	-
Lath-like bainite	-	-	-	-0.445	-
Acicular ferrite	-	-	-0.331	-	-
ECD 90%	-	-	-	-	-0.044
Retained austenite	-	-6.27	-	-4.20	-1.198
Inclusions >3 μm / mm ²	-1.343	-1.130	-	-0.721	-
MnS TiN >3 μm / mm ²	-	-	-9.650	-	-
<i>R</i> -sq(adj)	0.57	0.85	0.69	0.78	0.66
SE	14	10	6	7	2

Model A = CVN absorbed energy at -60 °C; Model B = CVN absorbed energy at -80 °C...-40 °C, two outliers ($\pm 3SD$) removed; *29.45 (-80 °C), 54.55 (-60 °C) and 73.58 (-40 °C); Model C = CVN crack initiation energy at -80 °C...-40 °C; **23.61 (-80 °C), 33.85 (-60 °C) and 34.16 (-40 °C); Model D = CVN crack propagation energy at -80 °C...-40 °C; ***21.99 (-80 °C), 36.02 (-60 °C) and 46.10 (-40 °C); Model E = CVN crack arrest energy at -80 °C...-40 °C; ****6.54 (-80 °C), 7.69 (-60 °C) and 12.73 (-40 °C)

6 Future considerations

Kernel Average Misorientation (KAM) was not considered in this research. It quantifies the average misorientation around a point of interest with respect to a defined set of nearest neighbour points. It is generally high in grains with high dislocation densities and is related to inner stresses in the microstructures. It could be one factor affecting the toughness of steel, particularly in heat-affected zones, and should be investigated.

Transmission electron microscopy (TEM) could be utilized more comprehensively in future studies of inclusions. In Publication III, TEM provided important and interesting details about a small inclusion, which would not have been possible with conventional scanning electron microscopy study. Additionally, the depletion of manganese content in the steel matrix next to the inclusion was possible to measure by TEM-EDS. However, only one inclusion from a chosen variant was studied by TEM. Further in-depth studies could reveal details of different types of inclusions and enable investigation as to how different types of inclusions, cooling rates, and other factors might affect the depletion of manganese content.

In the case of ultra-high-strength steels, only the properties of the base materials were studied. Weldability is naturally important in ultra-high-strength steels as well and hence, it would be beneficial to study the effect of inclusions on the toughness and ductility of heat-affected zones in these steels, too.

In the case of heat-affected zones of offshore steels, only coarse-grained heat-affected zones (CGHAZ) were considered in this study. However, practical offshore multipass weld structures consist of various heat-affected sub-zones, which could influence the mechanical properties of the steels. Therefore, more extensive studies, including multiple heat cycles, are needed in order to examine the influence of other heat-affected sub-zones in addition to the CGHAZ.

The focus in this research work was on the effect of inclusions on mechanical properties of steels. However, it was not studied that comprehensively and, despite some speculative understanding, it remained unclear as to why certain inclusion types and contents were present in the studied steels. The 500 MPa offshore steel variant without coarse titanium nitrides would be a particularly interesting subject for further studies.

The abnormal prior austenite grain growth in the CGHAZ of one of the experimental 420 MPa offshore also requires further study. This phenomenon was seen to influence both the promotion of acicular ferrite formation as well as

deterioration of the impact toughness of the steel in question. However, the reason for this grain growth remained unclear and requires investigation.

Initially, the aim of this doctoral research work was to find the critical level of inclusions in the studied steels, i.e., the number density and size of each inclusion type that can be allowed in the steel in order to be able to achieve the desired property goals. However, this aim was considered too ambitious in the context of this research work. In the future, more systematic studies are needed to find answers to these important research questions.

7 Summary and conclusions

The effect of inclusions on toughness and ductility has been studied in ultra-high-strength steels as well as in the coarse-grained heat-affected zones of different grades of high strength offshore steels. The main focus was on the detrimental effect of inclusions, but the beneficial effects of certain types of inclusions in promoting the formation of acicular ferrite and hence the toughness, were also considered. The following conclusions have been drawn:

Ultra-high-strength steels

Strength and, in some cases, hardness account for the key mechanical properties of ultra-high-strength steels. However, it is also necessary to ensure the manufacturability, e.g., bendability and weldability, of these steels and they are often related to ductility and toughness. Therefore, the aim was to study the effect of inclusions on ductility and toughness.

Total impurity levels ($IL = \%O + \%N + \%S$ in wt.%) were relatively low in the two studied steels, 91 ppm vs. 55 ppm. However, even with this small difference, the fraction of different types of coarse inclusions ($>8 \mu\text{m}$) was dramatic. MnS and TiN were the dominant coarse inclusions in the steel with higher IL due to slightly higher S and N content and a lower Ca/S ratio, while in the steel with lower IL, the coarse inclusions were mainly spherical $x\text{CaO}\cdot y\text{Al}_2\text{O}_3$, with or without CaS shells.

Due to the coarse MnS inclusions, the transverse ductility, measured as the reduction of area in tensile testing and upper shelf energy in Charpy V-notch impact toughness testing, was significantly lower in the steel with higher IL. The role of MnS was further confirmed by fractography studies of the tensile tested specimens.

Because of no remarkable difference between the steels in respect of longitudinal ductility, it was concluded that higher IL and subsequent elongated MnS increased the risk for in-plane anisotropy regarding the ductility.

A higher number of coarse TiN inclusions was concluded to decrease the impact toughness at $-40 \text{ }^\circ\text{C}$ in the steel with higher IL. Consequently, it was determined that the number density of coarse TiN should be minimised in order to avoid a negative effect on the toughness of ultra-high-strength steels.

Reasonably good ductility and toughness was achieved in both studied steels, indicating that impurity levels were low enough in both cases. However, for further development, it is essential to avoid elongated MnS and oxide stringers and

minimize the number density of coarse TiN in order to guarantee the best possible ductility and toughness in ultra-high-strength steels.

Offshore steels

With offshore steels, the focus was on the low temperature toughness at sub-zero temperatures, since the steels are designed for harsh weather conditions.

In the studied 500 MPa offshore steels, different microstructures formed after simulation of the coarse-grained heat-affected zone (CGHAZ) due to differences in carbon content. The differences in the transformed microstructures were remarkable, particularly when a cooling time of 6 seconds from 800 °C to 500 °C ($t_{8/5} = 6$ seconds) was applied. Whereas the steel with a carbon content of 0.02% had predominantly upper bainitic microstructure, the steel with a carbon content of 0.07% had lower bainitic microstructure and increased hardness. When the applied cooling time from 800 °C to 500 °C was 30 seconds ($t_{8/5} = 30$ seconds), the simulated CGHAZ microstructures of both steels consisted of a mixture of granular bainite and upper bainite.

Regarding inclusion contents, the main difference was in respect of the presence or absence of coarse titanium nitrides (TiN). The steel with a carbon content of 0.02% had variants with and without coarse TiN, while the steel with a carbon content of 0.07% had variants with lower and higher number densities of coarse TiN.

A brittle fracture was observed to have started from coarse TiN in most of the cases, indicating that such inclusions should be avoided in order to guarantee the best possible toughness in harsh service conditions.

When the primary fracture initiator was not found, it was expected that the fracture had started from coarse carbides within an upper bainitic matrix. Therefore, it might be necessary to use steels with lower carbon content when high heat-input welding methods, such as submerged arc welding (SAW), are required in order to achieve optimal CGHAZ microstructure to withstand low temperature conditions.

The fine-grained and lath-like CGHAZ microstructure achieved, when using low heat-input welding methods such as flux-cored arc welding (FCAW), has been shown to benefit toughness properties. In this case, the toughness at low temperatures can be further improved by preventing the formation of coarse TiN inclusions.

Ductility of the CGHAZ, measured through the evaluation of upper shelf energy (USE) in Charpy V-notch (CVN) impact toughness testing, was shown to depend on the strength. However, when the microstructures and consequent strengths were identical, ductility was concluded to have dependence on the total number density of inclusions.

In the laboratory scale 420 MPa offshore steels studied, the aim was to investigate the factors affecting the formation of acicular ferrite (AF) in the physically simulated CGHAZ. It was found that with the increase in cooling time, both the coarsened prior austenite grain size (PAGS) as well as the presence of small ($<3 \mu\text{m}$) MnO-TiO_x (+MnS) inclusions promoted the formation of AF.

The depletion of manganese content in the steel matrix next to the MnO-TiO_x (+MnS) type inclusions was confirmed both computationally and experimentally, thus explaining why these types of inclusions promote the formation of AF.

AF was assumed to improve the impact toughness of CGHAZs in 420 MPa offshore steels. However, it was shown that the best impact toughness was achieved in variants without or with only a small fraction of AF in the CGHAZ microstructure, while the variants with the highest fractions of AF had the lowest impact toughness among the studied steels.

It was concluded that despite the increased fraction of AF, the simultaneous occurrence of coarser microstructural and inclusion features diminished the positive effect of AF on the toughness. The marginally higher hardness and strength, as well as the increased fraction of retained austenite in the AF-containing variants, might have also had negative effect on the toughness. Additionally, even the maximum fraction of AF (46%) obtained in this study might not have been enough to improve the toughness.

8 Novel features

The following observations are believed to be novel at the time of publishing:

- On the effect of inclusions on direct-quenched ultra-high-strength steels, published research was very sparse at the time of publishing. Hence, most of the results on this topic, starting from the inclusion content of ultra-high-strength steels, can be considered novel.
- The inclusion content of modern direct-quenched, ultra-high-strength, martensitic steels was found to affect the transverse ductility of these steels. The novelty stems from the fact that even very small impurity levels in these modern steels were observed to have produced detrimental inclusions.
- The impairment of ductility in the studied ultra-high-strength steels can be reduced by preventing the formation of MnS inclusions. These inclusions were observed, even with very low sulphur content due to the segregation phenomenon. Already a low number density of MnS was concluded to have a significant negative effect on the ductility of these steels, owing to the pronounced vulnerability to the effect of inclusions along the increased strength.
- The number density of coarse TiN inclusions should be minimized in the studied ultra-high-strength steels in order to improve impact toughness. Due to the increased strength, even a relatively low number density of TiN may deteriorate the toughness in these steels.
- In the case of 500 MPa and 420 MPa offshore steels, the combination of different inclusion contents and coarse-grained heat-affected zones obtained by various cooling rates were studied more extensively than in previous publications.
- Base material toughness and ductility in 500 MPa offshore steels were observed to have not been affected by inclusions.
- Reducing the carbon content was suggested as the key to improve 500 MPa offshore steels' CGHAZ toughness properties at low temperatures, whenever welding with high heat-input welding methods is required. However, when low heat-input welding methods are utilized, the toughness properties at low temperatures can be improved by preventing the formation of coarse TiN inclusions.
- An acicular ferrite fraction of 46% in the CGHAZ of 420 MPa offshore steel was shown to be inadequate for the improvement of impact toughness of the

steel in question, while, at the same time, coarse microstructural features and a high number of coarse inclusions diminished the positive effect of acicular ferrite on the toughness.

References

- [1] A. McCance, "Non-metallic inclusions: their constitution and occurrence in steel," *J. Iron Steel Inst.*, vol. 97, no. 1, pp. 239–289, 1918.
- [2] A. D. Wilson, "Clean steel technology - Fundamental to the Development of High Performance Steel," in *Advances in the Production Use of Steel with Improved Internal cleanliness*, ASTM STP 1., J. K. Mahaney, Ed. West Conshohocken, PA: American Society for Testing and Materials, 1999, pp. 73–88.
- [3] P. Tardy, "The History of Ten Clean Steel Conferences," in *Proceedings of the 10th International Conference on Clean Steel*, 2018.
- [4] W. M. Garrison, "Ultrahigh-strength steels for aerospace applications," *JOM*, vol. 42, no. 5, pp. 20–24, May 1990.
- [5] E. Fuchs, and P. Jonsson, "Inclusion Characteristics in Bearing Steel Before and During Ingot Casting," *High Temp. Mater. Process.*, vol. 19, no. 5, pp. 333–344, Aug. 2000.
- [6] G. Pomey and B. Trentini, "Introductory address: some aspects of cleanness in steels," in *International Conference on Production and Application of Clean Steels*, 1970, pp. 1–14.
- [7] R. Willms, "High strength steel for steel constructions," *Nord. Steel Constr. Conf. Malmö, Sweden*, pp. 597–604, 2009.
- [8] *Weldable Structural Steels for Fixed Offshore Structures. Technical Delivery Conditions*, SFS-EN 10225, Finnish Standards Association, Sept. 2009.
- [9] *Material Data Sheets for Structural Steel*, NORSOK M-120, Standards Norway, Nov. 2008.
- [10] A. L. V. Da Costa E Silva, "The effects of non-metallic inclusions on properties relevant to the performance of steel in structural and mechanical applications," *J. Mater. Res. Technol.*, vol. 8, no. 2, pp. 2408–2422, 2019.
- [11] F. B. Pickering, "Some effects of non-metallic inclusions on the properties of steels," in *Mechanical Working and Steel Processing Proceedings*, 1989, pp. 381–401.
- [12] T. Gladman, *The Physical Metallurgy of Microalloyed Steels*. Leeds: Maney Publishing, 1997.
- [13] J.-S. Byun, J.-H. Shim, Y. W. Cho, and D. N. Lee, "Non-metallic inclusion and intragranular nucleation of ferrite in Ti-killed C–Mn steel," *Acta Mater.*, vol. 51, no. 6, pp. 1593–1606, Apr. 2003.
- [14] D. Loder, S. K. Michelic, and C. Bernhard, "Acicular Ferrite Formation and Its Influencing Factors-A Review," *J. Mater. Sci. Res.*, vol. 6, no. 1, pp. 24–43, 2017.
- [15] D. S. Sarma, A. V Karasev, and P. G. Jönsson, "On the Role of Non-metallic Inclusions in the Nucleation of Acicular Ferrite in Steels," *ISIJ Int.*, vol. 49, no. 7, pp. 1063–1074, 2009.
- [16] L. E. K. Holappa and A. S. Helle, "Inclusion Control in High-Performance Steels," *J. Mater. Process. Technol.*, vol. 53, pp. 177–186, 1995.
- [17] L. Holappa and O. Wijk, "Inclusion Engineering," in *Treatise on Process Metallurgy*, 1st ed., vol. 3, Elsevier, 2014, pp. 347–372.

- [18] K.-H. Kung, "A Study of Hot Shortness in Steels," M.Sc. thesis, Univ. of Missouri, Rolla, 1965.
- [19] I. Rak, V. Gliha, and M. Kqçak, "Weldability and toughness assessment of Ti-microalloyed offshore steel," *Metall. Mater. Trans. A Phys. Metall. Mater. Sci.*, vol. 28, no. 1, pp. 199–206, 1997.
- [20] J. Moon and C. Lee, "Behavior of (Ti, Nb)(C, N) complex particle during thermomechanical cycling in the weld CGHAZ of a microalloyed steel," *Acta Mater.*, vol. 57, no. 7, pp. 2311–2320, 2009.
- [21] W. Yan, Y. Y. Shan, and K. Yang, "Effect of TiN inclusions on the impact toughness of low-carbon microalloyed steels," *Metall. Mater. Trans. A*, vol. 37, no. 7, pp. 2147–2158, 2006.
- [22] S. Roy, S. Patra, S. Neogy, A. Laik, S. K. Choudhary, and D. Chakrabarti, "Prediction of Inhomogeneous Distribution of Microalloy Precipitates in Continuous-Cast High-Strength, Low-Alloy Steel Slab," *Metall. Mater. Trans. A*, vol. 43, no. 6, pp. 1845–1860, 2012.
- [23] D. P. Fairchild, D. G. Howden, and W. A. T. Clark, "The mechanism of brittle fracture in a microalloyed steel: Part I. Inclusion-induced cleavage," *Metall. Mater. Trans. A*, vol. 31, no. 3, pp. 641–652, 2000.
- [24] J. Du, M. Strangwood, and C. L. Davis, "Effect of TiN Particles and Grain Size on the Charpy Impact Transition Temperature in Steels," *J. Mater. Sci. Technol.*, vol. 28, no. 10, pp. 878–888, 2012.
- [25] H. K. D. H. Bhadeshia, "Physical Metallurgy of Steels," in *Physical Metallurgy*, vol. 3, 5th ed., D. E. Laughlin and K. Hono, Eds., Oxford, UK: Elsevier, 2014, ch. 21, pp. 2157–2214.
- [26] P. Suikkanen, "Development and processing of low carbon bainitic steels," D.Sc. dissertation, University of Oulu, 2009.
- [27] Z. Yang, F. Wang, S. Wang, and B. Song, "Intragranular Ferrite Formation Mechanism and Mechanical Properties of Non-quenched-and-tempered Medium Carbon Steels," *steel Res. Int.*, vol. 79, no. 5, pp. 390–395, 2008.
- [28] Z. Xiong, S. Liu, X. Wang, C. Shang, X. Li, and R. D. K. Misra, "The contribution of intragranular acicular ferrite microstructural constituent on impact toughness and impeding crack initiation and propagation in the heat-affected zone (HAZ) of low-carbon steels," *Mater. Sci. Eng. A*, vol. 636, pp. 117–123, 2015.
- [29] S. Zajac, J. Komenda, P. Morris, S. Matera, and F. Penalba Diaz, "Quantitative Structure-Property Relationships for Complex Bainitic Microstructure. RFCS Final Report," European Commission, Luxembourg, 2005.
- [30] H. K. D. H. Bhadeshia and C. M. Wayman, "Phase Transformations," in *Physical Metallurgy*, vol. 1, 5th ed., D. E. Laughlin and K. Hono, Eds., Oxford, UK: Elsevier, 2014, ch. 9, pp. 1021–1072.
- [31] G. F. Vander Voort, Ed., "Martensitic Structures," in *Metallography and Microstructures*, vol. 9, ASM International, 2004, pp. 165–178.
- [32] Y. Zeng, H. Fan, and X. Xie, "Effects of the shape and size of rectangular inclusions on the fatigue cracking behavior of ultra-high strength steels," *Int. J. Miner. Metall.*

- Mater.*, vol. 20, no. 4, pp. 360–364, 2013.
- [33] X. Li, J. Zhang, S. Shen, Y. Wang, and X. Song, “Effect of tempering temperature and inclusions on hydrogen-assisted fracture behaviors of a low alloy steel,” *Mater. Sci. Eng. A*, vol. 682, no. August 2016, pp. 359–369, 2017.
- [34] N. Ånmark, A. Karasev, and P. G. Jönsson, “The effect of different non-metallic inclusions on the machinability of steels,” *Materials (Basel)*, vol. 8, no. 2, pp. 751–783, 2015.
- [35] F. B. Pickering, *Physical metallurgy and the design of steels*. London: Applied Science Publishers Ltd., 1978.
- [36] W. T. Becker and S. Lampman, “Fracture Appearance and Mechanisms of Deformation and Fracture,” in *Failure Analysis and Prevention*, vol. 11, W. T. Becker and R. J. Shipley, Eds. ASM International, 2002, pp. 559–586.
- [37] J. F. Knott, “Second-phase particles and the toughness of structural steels,” in *Proc. Effect of second-phase particles on the mechanical properties of steel*, Scarborough, UK, March 24–25, 1971, pp. 44–53.
- [38] H. V. Atkinson and G. Shi, “Characterization of inclusions in clean steels: a review including the statistics of extremes methods,” *Prog. Mater. Sci.*, vol. 48, pp. 457–520, 2003.
- [39] G. H. Majzoubi, A. H. Mahmoudi, and S. Moradi, “Ductile to brittle failure transition of HSLA-100 Steel at high strain rates and subzero temperatures,” *Eng. Fract. Mech.*, vol. 158, pp. 179–193, Jun. 2016.
- [40] G. H. Xiao, H. Dong, M. Q. Wang, and W. J. Hui, “Effect of sulfur content and sulfide shape on fracture ductility in case hardening steel,” *J. Iron Steel Res. Int.*, vol. 18, no. 8, pp. 58–64, 2011.
- [41] A. Ghosh, P. Modak, R. Dutta, and D. Chakrabarti, “Effect of MnS inclusion and crystallographic texture on anisotropy in Charpy impact toughness of low carbon ferritic steel,” *Mater. Sci. Eng. A*, vol. 654, pp. 298–308, 2016.
- [42] A. D. Wilson, “the effect of inclusions on the properties of constructional steels,” in *Wear and Fracture Prevention*, Peoria, Illinois, USA, May 21–22, 1980, pp. 181–201.
- [43] A. D. Wilson, “the Effect of Inclusions on the Fracture Properties of A387-22 Steel Plate,” in *Proc. Advanced Materials for Pressure Vessel Service with Hydrogen at High Temperature and Pressures (MPC-18)*, Orlando, Florida, USA, June 27–July 2, 1982, pp. 203–221.
- [44] W. T. Becker, “Mechanisms and Appearances of Ductile and Brittle Fracture in Metals,” in *Failure Analysis and Prevention*, vol. 11, W. T. Becker and R. J. Shipley, Eds. ASM International, 2002, pp. 587–626.
- [45] R. Chen *et al.*, “The Scatter in Fracture Toughness of Two Different Pearlitic Railway Wheels,” *J. Mater. Eng. Perform.*, vol. 31, no. 11, pp. 9209–9219, 2022.
- [46] L. P. Zhang, C. L. Davis, and M. Strangwood, “Dependency of fracture toughness on the inhomogeneity of coarse TiN particle distribution in a low alloy steel,” *Metall. Mater. Trans. A*, vol. 32, no. 5, pp. 1147–1155, 2001.
- [47] D. Zhang, H. Terasaki, and Y. Komizo, “In situ observation of the formation of

- intragranular acicular ferrite at non-metallic inclusions in C–Mn steel,” *Acta Mater.*, vol. 58, no. 4, pp. 1369–1378, Feb. 2010.
- [48] H. Homma, S. Ohkita, S. Matsuda, and K. Yamamoto, “Improvement of HAZ in HSLA steel by Introducing finely dispersed Ti-Oxide,” *Weld. Res. Suppl.*, pp. 301–309, 1987.
- [49] R. Laitinen, “Improvement of weld HAZ toughness at low heat input by controlling the distribution of M-A constituents,” D.Sc. dissertation, University of Oulu, 2006.
- [50] D. Haaland, C. Van Der Eijk, and Ø. Grong, “The role of interactive particles in steel,” in *Safety in application of high strength steel* symposium, Trondheim, Norway, 1–2 July, 1997.
- [51] H. Mabuchi, R. Uemori, and M. Fujioka, “The Role of Mn Depletion in Intra-Granular Ferrite Transformation in the Heat Affected Zone of Welded Joints with Large Heat Input in Structural Steels.,” *ISIJ Int.*, vol. 36, no. 11, pp. 1406–1412, 1996.
- [52] Y. Kang, J. Jang, J. H. Park, and C. Lee, “Influence of Ti on non-metallic inclusion formation and acicular ferrite nucleation in high-strength low-alloy steel weld metals,” *Met. Mater. Int.*, vol. 20, no. 1, pp. 119–127, 2014.
- [53] T. Alatarvas, “Evolution of inclusion population in calcium treated ultra-high strength steels : novel applications of sample data treatment,” D.Sc. dissertation, University of Oulu, 2018.
- [54] *Metallic materials — Tensile testing — Part 1: Method of test at room temperature*, ISO 6892-1:2019, ISO, 2019.
- [55] *Metallic materials - Charpy pendulum impact test - Part 1: Test method*, 3rd ed., EN ISO 148-1, ISO, 2016.
- [56] *Metallic materials. Charpy V-notch pendulum impact test. Instrumented test method (ISO 14556 : 2015) Metallien Charpyn iskukoe V-lovikoesauvalla. Instrumentoitu koe*, SFS-EN ISO 14556, Finnish Standards Association, 2015.
- [57] *Metallic materials — Determination of plane-strain fracture toughness*, ISO 12737:2010, ISO, 2010.
- [58] A. Kaijalainen, S. Pallaspuro, and D. A. Porter, “Tempering of Direct Quenched Low-Alloy Ultra-High-Strength Steel, Part I – Microstructure,” *Adv. Mater. Res.*, vol. 922, pp. 316–321, 2014.
- [59] K. Wallin, *Fracture Toughness of Engineering Materials - Estimation and Application*. Warrington: EMAS Publishing, 2011.
- [60] A. Kaijalainen *et al.*, “Effect of inclusions on the properties of ultra-high-strength low-alloy steel with a martensitic-bainitic microstructure,” in *Proc 8th Int. Conf. Clean Steel*, Budapest, Hungary, May 14–16, 2012.
- [61] H. Tervo, “Effect of inclusions on mechanical properties of steel,” M.Sc. thesis, University of Oulu, 2014.
- [62] S. Zajac, V. Schwinn, and K. H. Tacke, “Characterisation and Quantification of Complex Bainitic Microstructures in High and Ultra-High Strength Linepipe Steels,” *Mater. Sci. Forum*, vol. 500–501, pp. 387–394, 2005.
- [63] A. J. Kaijalainen, M. Liimatainen, V. Kesti, J. Heikkala, T. Liimatainen, and D. A.

- Porter, "Influence of Composition and Hot Rolling on the Subsurface Microstructure and Bendability of Ultrahigh-Strength Strip," *Metall. Mater. Trans. A Phys. Metall. Mater. Sci.*, vol. 47, no. 8, pp. 4175–4188, 2016.
- [64] N. Haghdadi, D. Abou-ras, P. Cizek, P. D. Hodgson, A. D. Rollett, and H. Beladi, "Austenite-ferrite interface crystallography dependence of sigma phase precipitation using the five-parameter characterization approach," *Mater. Lett.*, vol. 196, pp. 264–268, 2017.
- [65] S. L. Shrestha, A. J. Breen, P. Trimby, G. Proust, S. P. Ringer, and J. M. Cairney, "An automated method of quantifying ferrite microstructures using electron backscatter diffraction (EBSD) data," *Ultramicroscopy*, vol. 137, pp. 40–47, 2014.
- [66] S. Kennett, "Strengthening and Toughening Mechanisms in Low-C Microalloyed Steel as Influenced by Austenite Conditioning," Ph.D. dissertation, Colorado School of Mines, 2014.
- [67] A. J. Kaijalainen, P. P. Suikkanen, T. J. Linnell, L. P. Karjalainen, J. I. Kömi, and D. A. Porter, "Effect of austenite grain structure on the strength and toughness of direct-quenched martensite," *J. Alloys Compd.*, vol. 577S, no. SUPPL. 1, pp. S642–S648, 2013.
- [68] K. J. Irvine and F. . Pickering, "The Impact Properties of Low Carbon Bainitic Steels," *J. Iron Steel Inst.*, vol. 201, pp. 518–531, 1963.
- [69] P. Brozzo, G. Buzzichelli, A. Mascanzoni, and M. Mirabile, "Microstructure and cleavage resistance of low-carbon bainitic steels," *Met. Sci.*, vol. 11, no. 4, pp. 123–130, Apr. 1977.
- [70] C. Wang, M. Wang, J. Shi, W. Hui, and H. Dong, "Effect of microstructural refinement on the toughness of low carbon martensitic steel," *Scr. Mater.*, vol. 58, no. 6, pp. 492–495, 2008.
- [71] J. W. Morris, Jr., "On the Ductile-Brittle Transition in Lath Martensitic Steel," *ISIJ Int.*, vol. 51, no. 10, pp. 1569–1575, 2011.
- [72] S. Morito, H. Yoshida, T. Maki, and X. Huang, "Effect of block size on the strength of lath martensite in low carbon steels," *Mater. Sci. Eng. A*, vol. 438–440, no. SPEC. ISS., pp. 237–240, 2006.
- [73] S. Pallaspuuro, A. Kaijalainen, T. Linnell, and D. A. Porter, "Tempering of Direct Quenched Low-Alloy Ultra-High-Strength Steel, Part II – Mechanical Properties," *Adv. Mater. Res.*, vol. 922, pp. 580–585, May 2014.
- [74] A. D. Wilson, "Characterization of Inclusions in Plate Steels and Their Influence on Mechanical Properties," in *Inclusions and their influence on material behavior: Proceedings of a symposium held in conjunction with the 1988 World Materials Congress, Chicago, Illinois, USA, September 24–30, 1988*, ed. R. Rungta. Published by ASM, pp. 21–34.
- [75] J. Steninger and A. Melander, "The relation between bendability, tensile properties and particle structure of low carbon steel," *Scand. J. Metall.*, vol. 11, pp. 55–71, 1982.
- [76] A. Ghosh, S. Das, and S. Chatterjee, "Ultrahigh strength hot rolled microalloyed steel: microstructure and properties," *Mater. Sci. Technol.*, vol. 21, no. 3, pp. 325–

333, 2005.

- [77] Y. Han and S. Kuang, "Effect of nitrogen content on mechanical properties of Ti-microalloyed low carbon martensite steel," *Jinshu Rechuli/Heat Treat. Met.*, vol. 40, no. 10, 2015.
- [78] A. Echeverria and J. M. Rodriguez-Ibabe, "Brittle fracture micromechanisms in bainitic and martensitic microstructures in a C-Mn-B steel," *Scr. Mater.*, vol. 41, no. 2, pp. 131–136, 1999.
- [79] J.-H. Shim, Y. . Cho, S. . Chung, J.-D. Shim, and D. . Lee, "Nucleation of intragranular ferrite at Ti₂O₃ particle in low carbon steel," *Acta Mater.*, vol. 47, no. 9, pp. 2751–2760, Jul. 1999.
- [80] Z. Zhang and R. A. Farrar, "Role of non-metallic inclusions in formation of acicular ferrite in low alloy weld metals," *Mater. Sci. Technol.*, vol. 12, no. 3, pp. 237–260, Mar. 1996.
- [81] M. Enomoto, "Nucleation of phase transformations at intragranular inclusions in steel," *Met. Mater.*, vol. 4, no. 2, pp. 115–123, Mar. 1998.
- [82] T. Koseki, S. Ohkita, and N. Yurioka, "Thermodynamic study of inclusion formation in low alloy steel weld metals," *Sci. Technol. Weld. Join.*, vol. 2, no. 2, pp. 65–69, Apr. 1997.
- [83] Y. Tomita, N. Saito, T. Tsuzuki, Y. Tokunaga, and K. Okamoto, "Improvement in HAZ Toughness of Steel by TiN-MnS Addition.," *ISIJ Int.*, vol. 34, no. 10, pp. 829–835, 1994.
- [84] J.-O. Andersson, T. Helander, L. Höglund, P. Shi, and B. Sundman, "Thermo-Calc & DICTRA, computational tools for materials science," *Calphad*, vol. 26, no. 2, pp. 273–312, Jun. 2002.
- [85] F. J. Barbaro, P. Krauklis, and K. E. Easterling, "Formation of acicular ferrite at oxide particles in steels," *Mater. Sci. Technol.*, vol. 5, no. 11, pp. 1057–1068, Nov. 1989.
- [86] K. Yamamoto, S. Matsuda, T. Haze, R. Chijiwa, and H. Mimura, "A Newly Developed Ti-Oxide Bearing Steel Having High HAZ Toughness," in *Residual and Unspecified Elements in Steel*, A. S. Melilli and E. G. Nisbett, Eds. West Conshohocken, PA: ASTM International, 1989, pp. 266–284.
- [87] A. Echeverria and J. M. Rodriguez-Ibabe, "The role of grain size in brittle particle induced fracture of steels," *Mater. Sci. Eng. A*, vol. 346, no. 1–2, pp. 149–158, 2003.
- [88] L. P. Zhang, C. L. Davis, and M. Strangwood, "Effect of TiN particles and microstructure on fracture toughness in simulated heat-affected zones of a structural steel," *Metall. Mater. Trans. A*, vol. 30, no. 8, pp. 2089–2096, Aug. 1999.
- [89] S. Pallaspuuro, S. Mehtonen, J. Kömi, Z. Zhang, and D. Porter, "Effects of local grain size and inclusions on the low-temperature toughness of low-carbon as-quenched martensite," *Mater. Sci. Eng. A*, vol. 743, no. August 2018, pp. 611–622, 2019.

Original publications

- I Tervo, H., Kaijalainen, A., Pikkarainen, T., Mehtonen, S., & Porter, D. (2017). Effect of impurity level and inclusions on the ductility and toughness of an ultra-high-strength steel. *Materials Science & Engineering A*, 697, 184–193. <https://doi.org/10.1016/j.msea.2017.05.013>
- II Tervo, H., Kaijalainen, A., Pallaspuuro, S., Anttila, S., Mehtonen, S., Porter, D., & Kömi, J. (2020). Low-temperature toughness properties of 500 MPa offshore steels and their simulated coarse-grained heat-affected zones. *Materials Science & Engineering A*, 773, 138719. <https://doi.org/10.1016/j.msea.2019.138719>
- III Tervo, H., Kaijalainen, A., Javaheri, V., Kolli, S., Alatarvas, T., Anttila, S., & Kömi, J. (2020). Characterization of coarse-grained heat-affected zones in Al and Ti-deoxidized offshore steels. *Metals*, 10(8), 1096. <https://doi.org/10.3390/met10081096>
- IV Tervo, H., Kaijalainen, A., Javaheri, V., Ali, M., Alatarvas, T., Mehtonen, M., Anttila, S., & Kömi, J. (2021). Comparison of impact toughness in simulated coarse-grained heat-affected zone of Al-deoxidized and Ti-deoxidized offshore steels. *Metals*, 11(11), 1783. <https://doi.org/10.3390/met11111783>

Reprinted with permission from the publisher Elsevier (Publications I and II © 2017, 2019 Elsevier B.V.) and under CC BY 4.0 license² (Publications III and IV © 2020, 2021 Authors).

Original publications are not included in the electronic version of the dissertation.

² <https://creativecommons.org/licenses/by/4.0/>

848. Afonin, Nikita (2022) Development of passive seismic interferometry to study shallow subsurface structure
849. Sdobnov, Anton (2022) Laser speckle contrast imaging for functional visualization
850. Tampio, Kari-Pekka (2022) Enhancing value creation at the front-end of a collaborative hospital construction project
851. Annunen, Petteri (2022) Industrialization in construction : a process model for capability creation
852. Omodara, Linda (2022) Developing and testing sustainability assessment tools for chemical processes and products : case study on critical rare earth elements
853. Karimidastenaei, Zahra (2022) The potential of unconventional water in limiting water scarcity
854. Kallio, Rita (2022) Multidisciplinary study of the beneficiation potential of the Kiviniemi ferrous scandium deposit
855. Kiani, Sepideh (2022) Development of passive bioreactors treating different types of low carbon wastewater in cold climate conditions
856. Latypova, Renata (2022) Development and application of a novel tuning-fork test in studying hydrogen-induced fracture in as-quenched martensitic steels
857. Sone, Su Pyae (2022) Proactive resource allocation in spectrum sharing with radar systems via ML-based wireless network time series forecasting
858. Huynh, Lam (2022) From 3D sensing to dense prediction
859. Ismail, (2022) Monitoring ecohydrological process and forest dynamics in a tropical peatland
860. Juntti, Mirva (2022) Public service productization : a constructive approach on research, development and innovation process of University of Applied Sciences
861. Nikula, Riku-Pekka (2022) Automated methods for vibration-based condition monitoring of rotating machines
862. Bhattacharjee, Joy (2022) Assessment of changes in hydrology and water quality in peat-dominated catchments due to foreseen changes in bioeconomy-driven landuses
863. Keikkala, Ville (2022) Development of vertical stirred mill grinding disc and chamber design : Effect on grinding efficiency and media behaviour and laboratory to plant size scale-up study

S E R I E S E D I T O R S

A
SCIENTIAE RERUM NATURALIUM
University Lecturer Tuomo Glumoff

B
HUMANIORA
University Lecturer Santeri Palviainen

C
TECHNICA
Postdoctoral researcher Jani Peräntie

D
MEDICA
University Lecturer Anne Tuomisto

E
SCIENTIAE RERUM SOCIALIUM
University Lecturer Veli-Matti Ulvinen

E
SCRIPTA ACADEMICA
Planning Director Pertti Tikkanen

G
OECONOMICA
Professor Jari Juga

H
ARCHITECTONICA
Associate Professor (tenure) Anu Soikkeli

EDITOR IN CHIEF
University Lecturer Santeri Palviainen

PUBLICATIONS EDITOR
Publications Editor Kirsti Nurkkala

ISBN 978-952-62-3548-6 (Paperback)
ISBN 978-952-62-3549-3 (PDF)
ISSN 0355-3213 (Print)
ISSN 1796-2226 (Online)